

PhD thesis

Dark-field hyperlens

High-contrast subwavelength imaging in optics and acoustics

Taavi Repän

December 10, 2018

DTU Fotonik
Technical University of Denmark

Contents

Abstract	5
Resumé	7
List of publications	9
1. Introduction	13
I. Background	17
2. Basic theory	19
2.1. Electromagnetic wave equation	19
2.2. Propagation of plane waves	20
2.3. Angular spectrum representation	21
2.4. Wave propagation in anisotropic media	22
2.5. Summary	23
3. Hyperbolic metamaterials	25
3.1. Introduction	25
3.2. Wave propagation in HMMs	27
3.3. Multilayer structures as HMMs	36
3.4. HMMs with magnetic properties	42
3.5. Hyperbolic metamaterials in acoustics	43
3.6. Summary	45
4. Diffraction limit and subwavelength imaging	47
4.1. Diffraction limit	47
4.2. Devices for subwavelength imaging	48
4.3. Hyperlens	49
4.4. Magnification in cylindrical hyperlens	52
4.5. Summary	53

II. Results	55
5. Dark-field hyperlens	57
5.1. Introduction	57
5.2. Scattering via type-II HMM slab	58
5.3. Cylindrical geometry: dark-field hyperlens	63
5.4. Hybrid design: avoiding low-k cutoff	67
5.5. Summary	71
Acoustic dark-field hyperlens	71
6. Magnetic dark-field hyperlens	73
6.1. Motivation: “pseudocanalization” via phase compensation	73
6.2. Phase compensation in planar structures	75
6.3. Cylindrical geometry: pseudocanalizing hyperlens	84
6.4. Summary	89
7. Surface waves	91
7.1. Motivation	91
7.2. Surface waves on a single interface	91
7.3. Surface waves in a three-layer system	101
7.4. Pseudocanalization with surface waves	108
7.5. Summary	110
8. Conclusions	111
Acknowledgments	113
Bibliography	114

Abstract

This thesis has been written in part of the DarkSILD project. Aim of the project (and the thesis) is to explore possibilities for superresolution imaging of weakly scattering objects in bioimaging applications, for example. The thesis contains results of theoretical analysis and numerical simulations, carried out by the finite-element package COMSOL Multiphysics.

The first half of the thesis gives a comprehensive overview of hyperbolic metamaterials: how to describe wave propagation in such structures, how the metamaterial parameters affect wave propagation and behavior, and how to design hyperbolic metamaterials using metal-dielectric multilayers. I also explore how such properties come into play when designing hyperlenses for superresolution imaging.

The second part of the thesis covers results of the PhD project. I start by presenting the dark-field hyperlens, using the theory developed in the first part of the thesis to discuss design challenges of the dark-field design. The design is based on a metal-dielectric multilayer with realistic material parameters, although as I will discuss the dark-field operation creates several new challenges.

Thesis continues with more theoretical work, covering magnetic dark-field hyperlenses. Here I show that by also incorporating negative permeability hyperbolic metamaterials we can avoid some of the challenges, that seriously hampered performance of the earlier design.

Finally, I move from hyperbolic metamaterials to anisotropic interfaces, which support hyperbolic surface waves. This allows applying the magnetic hyperlens design in a more realistic setting, as surface waves can be engineered to offer similar propagation properties as magnetic metamaterials, without actually requiring magnetic material properties.

Resumé

Denne afhandling er udarbejdet som en del af DarkSILD projektet. Målet for projektet (samt denne afhandling) er at undersøge muligheder for afbildning med superopløsning af objekter med svag spredning indenfor for eksempel biologiskafbildning. Afhandlingen indeholder resultater fra teoretiske analyser samt fra numeriske simuleringer udført med det endelige-element program COMSOL Multiphysics.

Den første halvdel af afhandlingen giver et omfattende overblik over hyperbolske metamaterialer: hvordan bølgeudbredelse i disse strukturer beskrives, hvordan metamaterialeparametrene påvirker bølgeudbredelsen og bølgeopførslen, og hvordan hyperbolske materialer designs ved brug af flere metal-dielektrikum lag. Jeg undersøger også, hvordan disse egenskaber kommer i spil, når hyperlinser for superopløsningsafbildning designs.

Afhandlingens anden del omhandler resultaterne af dette PhD-projekt. Jeg starter med at præsentere mørkfeltshyperlinsen ved brug af den i første halvdel udviklede teori for at diskutere udfordringerne ved et mørkfeltsdesign. Designet er baseret på multiple metal-dielektrikum lag med realistiske materiale parametre, selvom mørkfeltsbetjening kreerer flere nye udfordringer, hvilket jeg ligeledes diskuterer.

Afhandlingen fortsætter med mere teoretisk arbejde omhandlende magnetiske mørkfeltslinser. Her viser jeg, at ved at inkorporere negative permeabilitets-hyperbolske-metamaterialer kan vi undgå nogle af udfordringerne, som hæmmede ydeevnen af det tidligere design i alvorlig grad.

Til sidst bevæger jeg mig fra hyperbolske metamaterialer til anisotropiske grænseflader, som understøtter hyperbolske overfladebølger. Dette tillader anvendelsen af magnetiske hyperlinsedesigns i et mere realistisk format, da overfladebølger kan manipuleres til at give udbredelsesegenskaber lig magnetiske metamaterialers uden at skulle bruge magnetiske materialeegenskaber.

List of publications

Published journal articles:

- J1 **Taavi Repän**, Andrei V. Lavrinenko, and Sergei V. Zhukovsky.
Dark-field hyperlens: Super-resolution imaging of weakly scattering objects.
Optics Express, 23(19):25350, 2015.
- J2 **Taavi Repän**, Andrey Novitsky, Morten Willatzen, and Andrei V. Lavrinenko.
Pseudocanalization regime for magnetic dark-field hyperlenses.
Physical Review B, 96(19), 2017.

Manuscripts in preparation:

- J3 **Taavi Repän**, Osamu Takayama, Morten Willatzen, and Andrei V. Lavrinenko.
Engineering phase propagation of hyperbolic surface waves.

Published journal articles (not included in the thesis):

- J4 Leonid Dolgov, Olena Fesenko, Vladyslav Kavelin, Oksana Budnyk, Victorio Estrela-Llopis, Alona Chevychalova, **Taavi Repän**, Vladimir I. Kondratiev and Sergii Mamykin.
Gold micro- and nano-particles for surface enhanced vibrational spectroscopy of pyridostigmine bromide.
Vibrational Spectroscopy, 88, 2017.
- J5 Evgeniy Shkondin, **Taavi Repän**, Osamu Takayama, Andrei Lavrinenko.
High aspect ratio titanium nitride trench structures as plasmonic biosensor.
Optical Materials Express, 7(11), 2017.
- J6 Osamu Takayama, Evgeniy Shkondin, Andrey Bodganov, Mohammad Esmail Aryaee Panah, Kirill Golenitskii, Pavel Dmitriev, **Taavi Repän**, Radu Malureanu, Pavel A. Belov, Flemming Jensen and Andrei V. Lavrinenko.
Midinfrared Surface Waves on a High Aspect Ratio Nanotrench Platform.
ACS Photonics, 4(11), 2017.

List of publications

- J7 Christian Frydendahl, **Taavi Repän**, Mathias Geisler, Sergey M. Novikov, Jonas Beermann and Andrei Lavrinenko, Sanshui Xiao, Sergey I. Bozhevolnyi, N. Asger Mortensen and Nicolas Stenger.
Optical reconfiguration and polarization control in semi-continuous gold films close to the percolation threshold.
Nanoscale, 9(33), 2017.
- J8 Andrey Novitsky, **Taavi Repän**, Sergei Zhukovsky and Andrei Lavrinenko.
Subwavelength Hyperlens Resolution With Perfect Contrast Function.
Annalen der Physik, 530(3), 2018.
- J9 Evgeniy Shkondin, **Taavi Repän**, Mohammad Esmail Aryaee Panah, Andrei V. Lavrinenko, and Osamu Takayama.
High Aspect Ratio Plasmonic Nanotrench Structures with Large Active Surface Area for Label-Free Mid-Infrared Molecular Absorption Sensing.
ACS Applied Nano Materials, 1(3), 2018.

Conference contributions:

- C1 **Taavi Repän**, Sergei Zhukovsky, Andrei Lavrinenko and Morten Willatzen.
Dark-field hyperlens for high-contrast sub-wavelength imaging.
Oral presentation at *CLEO Europe*, 2016.
- C2 **Taavi Repän**, Christian Frydendahl, Sergey M. Novikov, Jonas Beermann, Sergey I. Bozhevolnyi, N. Asger Mortensen, Nicolas Stenger, Morten Willatzen and Andrei Lavrinenko.
Numerical simulations of nanostructured gold films.
Oral presentation at *NUSOD*, 2017.
- C3 **Taavi Repän**, Andrey Novitsky, Morten Willatzen, Andrei Lavrinenko.
Compensation of loss-induced beam broadening in HMMs by a μ -negative HMM.
Poster presentation at *Metamaterials Congress*, 2017.
- C4 **Taavi Repän**, Andrey Novitsky, Morten Willatzen, Andrei Lavrinenko.
Reversed phase propagation for hyperbolic surface waves.
Oral presentation at *OWTNM*, 2018.
- C5 **Taavi Repän**, Andrey Novitsky, Morten Willatzen, Andrei Lavrinenko.
Pseudocanalization regime for surface waves.
Poster presentation at *CLEO*, 2018.

C6 **Taavi Repän**, Andrey Novitsky, Morten Willatzen, Andrei Lavrinenko.
Pseudocanalizing propagation with hyperbolic surface waves.
Oral presentation at *OSA Advanced Photonics Congress*, 2018.

1. Introduction

Metamaterials The term *metamaterials* emerged at the beginning of this century in electromagnetics research [1], although it should be noted that there are plenty of earlier works that now would be called metamaterials as well. The metamaterials concept has by now reached in many other research fields apart from electromagnetics (e.g. acoustics [2], mechanics [3]).

Just as naturally occurring materials are made of atoms, metamaterials consist of “meta-atoms”. By building a large-scale structure made of small structures, the inner details of the meta-atoms can be abstracted away. Instead we describe response of the whole structure with effective averaged parameters linked to the response of the individual meta-atoms.

In electromagnetics the metamaterials research now covers spectral range from gigahertz to visible wavelengths in optics [4]. Although the name is same, the nature of the game is not. For microwave applications metals behave as perfect conductors and with wavelength in range of centimeters the constituent unit cells of the metamaterial structures can be as small as $\lambda/100$. On the other hand, in optics the metals are not perfect conductors, allowing electromagnetic fields to penetrate metallic structures, giving rise to plasmonic effects [5–8]. Here however one has to deal with ohmic losses in the metal, potentially reducing the range of practical applications.

Focus for electromagnetic (optical?) metamaterials was at first on negative-index metamaterials (also known as double negative medium, indicating that both dielectric permittivity ε and permeability μ are negative). The idea of negative index medium itself is not that recent: it was first proposed by Veselago in 1968 [9], but although experimental demonstrations appeared only at turn of the century [10–12].

Hyperbolic metamaterials (HMMs) is another well-known class of metamaterials [13, 14]. HMMs are uniaxial anisotropic structures, which offer extremely strong anisotropy by behaving like a dielectric in one axis while exhibiting metallic behavior in the other. Quite soon after first theoretical works [15, 16], experimental demonstrations of HMMs followed [17–19].

1. Introduction

Subwavelength imaging Optical microscopy is an important in a wide range of fields. However, already in 1873 Abbe discovered the diffraction limit: wave nature of light limits resolution of optical microscopes to $\sim \lambda/2$ [20–22]. Perhaps most straightforward way around this is to use electron microscopy, as electron wavelength is orders of magnitude smaller than wavelength of visible light. For many applications however we are keen to work with optical wavelengths. Various techniques has been developed to circumvent the diffraction limit, such as scanning optical microscopy (SNOM) [23, 24] and stimulated depletion emission microscopy (STED) [25, 26]. Metamaterials research has also yielded possible ways to achieve subwavelength resolution (superlens [27], hyperlens [16, 18, 28–32], dark-field hyperlens [33–36]), but unlike SNOM and STED these approaches are yet to reach practical use. Interestingly, the metamaterials have also been used to design superresolution devices in acoustics as well [37–41].

Motivation and aim for the PhD project The thesis focuses on theoretical studies of hyperlens: a design to use hyperbolic metamaterials for subwavelength imaging. In particular we will focus on dark-field hyperlens, where by suitable tuning wave propagation in the hyperbolic medium we can separate scattered fields from the incident radiation, thus enabling dark-field imaging.

We use theoretical calculations and finite-element full-wave simulations to study wave propagation in HMMs and to explore the idea of dark-field hyperlens. Mostly we are focused on underlying properties of the HMMs and important design considerations there. We briefly also cover theory for a more practical design (metal-dielectric multilayer), but we note that the dark-field hyperlens has inherent drawbacks in design requirements, so practical realizations of the idea are unlikely to manifest.

Structure of the thesis The thesis is divided into two major parts. The first part covers necessary background knowledge needed for rest of the thesis. In chapter 2 we start from basic Maxwell’s equations and then cover basic principles of hyperbolic metamaterials and mathematical tools we use for understanding such structures (chapter 3). We then introduce mathematical formulation of the diffraction limit and give short overview of techniques for superresolution imaging techniques in chapter 4.

In the second part we cover the results of this PhD project. In chapters 5 to 7 we present work published in two journal articles [34, 42] and in one in-progress

manuscript. In chapter 5 we introduce the idea of type-II hyperbolic metamaterial (HMM) based dark-field hyperlens, implemented with a metal-dielectric multilayer structure. We will analyze the basic idea and following design challenges for the dark-field hyperlens. Then, in chapter 6, we move further into theoretical discussions as we also consider magnetic properties of the hyperlens. This allows to overcome several design challenges of the original design. Finally we discuss hyperbolic surface waves and see how anisotropic interfaces can “emulate” behavior of magnetic HMMs, without actually needing magnetic properties (chapter 7).

Part I.

Background

This part introduces the necessary theory and gives a brief overview of hyperbolic metamaterials, subwavelength imaging and also of the hyperlens concept itself. We touch upon important results and literature, relevant from the hyperlens perspective.

2. Basic theory

2.1. Electromagnetic wave equation

Maxwell's equations are the starting point for all work in optical materials. In this work we are working exclusively with time-harmonic fields, so we start from Maxwell's equations in the frequency domain:¹

$$\nabla \cdot \mathbf{D} = 0 \quad (2.1)$$

$$\nabla \cdot \mathbf{B} = 0, \quad (2.2)$$

$$\nabla \times \mathbf{E} = i\omega \mathbf{B}, \quad (2.3)$$

$$\nabla \times \mathbf{H} = -i\omega \mathbf{D}. \quad (2.4)$$

These equations are obtained by assuming time-harmonic form for the electric and magnetic fields [$\tilde{\mathbf{F}}(\mathbf{r}, t) = \mathbf{F}(\mathbf{r}) \exp(-i\omega t)$] and neglecting free currents and charges in the time-domain Maxwell's equations[23, 43]. Relations between \mathbf{D} , \mathbf{B} and \mathbf{E} , \mathbf{H} fields are given by the constitutive relations (this is for the isotropic case — we will cover the anisotropic case at the end of the chapter)

$$\mathbf{D} = \varepsilon_0 \varepsilon \mathbf{E}, \quad (2.5)$$

$$\mathbf{B} = \mu_0 \mu \mathbf{H}. \quad (2.6)$$

However, for our purposes Maxwell's equations (a set of coupled equations) is not the most convenient form. For a homogeneous medium we can insert eq. (2.3) into eq. (2.4) and with help of eqs. (2.1), (2.5) and (2.6) we arrive at

$$\nabla^2 \mathbf{E} + k_0^2 \varepsilon \mu \mathbf{E} = 0, \quad (2.7)$$

¹The fields are functions of space coordinates \mathbf{r} as well, but for notational convenience we do not explicitly write them out.

2. Basic theory

where $k_0 = \omega/c$ is the free-space wavenumber. Equation (2.7) is also known as the electromagnetic wave equation.

As we noted, eq. (2.7) was derived for a homogeneous medium. In practice we mostly deal with piecewise homogeneous media, where we have two or more different media, separated by interfaces. To link the solutions in different media we need to apply electromagnetic interface conditions. Equations (2.3) and (2.4) (in integral form) give conditions for the tangential field components

$$\mathbf{n} \times (\mathbf{E}_1 - \mathbf{E}_2) = 0, \quad (2.8)$$

$$\mathbf{n} \times (\mathbf{H}_1 - \mathbf{H}_2) = 0, \quad (2.9)$$

where \mathbf{n} is normal vector of the interface. Similarly, from eqs. (2.1) and (2.2) follow the conditions for the normal field components

$$\mathbf{n} \cdot (\mathbf{D}_1 - \mathbf{D}_2) = 0, \quad (2.10)$$

$$\mathbf{n} \cdot (\mathbf{B}_1 - \mathbf{B}_2) = 0. \quad (2.11)$$

2.2. Propagation of plane waves

The simplest nontrivial solutions for eq. (2.7) are plane waves, given by amplitude E_0 and wavevector $\mathbf{k} = k_x \hat{\mathbf{x}} + k_y \hat{\mathbf{y}} + k_z \hat{\mathbf{z}}$:

$$\mathbf{E} = E_0 \exp(i\mathbf{k} \cdot \mathbf{r}). \quad (2.12)$$

The simplicity of plane waves means that in many cases it is the easiest to decompose the fields in terms of plane waves and solve the problem in terms of plane wave components of the fields. We start from looking at the propagation of a single plane wave and later extend the discussion to arbitrary fields (e.g. fields originating from a point source or a fields scattering away from an object).

We insert the plane wave solution [eq. (2.12)] into the wave equation [eq. (2.7)] to get

$$-(k_x^2 + k_y^2 + k_z^2) \exp(i\mathbf{k} \cdot \mathbf{r}) + k_0^2 \epsilon \mu \exp(i\mathbf{k} \cdot \mathbf{r}) = 0,$$

from which we identify a condition that must be fulfilled for the plane wave to be

2.3. Angular spectrum representation

solution to the wave equation,

$$k_x^2 + k_y^2 + k_z^2 = k_0^2 \varepsilon \mu . \quad (2.13)$$

In other words, this equation — the dispersion equation — describes a set of plane waves (identified by the wavevector components k_x , k_y and k_z) that are allowed to propagate in the medium.

Having reached the dispersion relation, we can now describe behavior of waves in the medium in terms of plane waves. Firstly, to illuminate the meaning of the equation, we assume $k_x = 0$, $k_y = 0$ in order to look at a plane wave with wavevector pointing in z -direction. Writing out eq. (2.12) for this case gives

$$\mathbf{E} = \mathbf{E}_0 \exp (i k_z z) .$$

We note that if k_z is real then it is a propagating wave. However, the k_z could also be imaginary (e.g. when $\varepsilon < 0$). In such case the wave will be exponentially decaying, also known as an evanescent wave. Such waves are not propagating and are only present near surfaces or interfaces (as they decay to zero further away).

In the context of this thesis we are interested in solving propagation problems. Namely, we suppose we are given initial fields at $z = 0$ and we are interested in fields obtained after some distance d . For our purposes the z is the propagation coordinate and x , y are transverse coordinates.

As we assume that fields on the x - y plane (at $z = 0$) are known, we take the k_x, k_y components of the wavevector to be given us by the problem description. Therefore we consider these to be independent variables of our problem. The k_z component we take to be the dependent variable, obtained by solving the dispersion relation eq. (2.13). Given the wavevector component along the propagation axis k_z (the propagation constant) we can calculate the propagated fields from initial fields using

$$\mathbf{E} (k_x, k_y; z) = \mathbf{E} (k_x, k_y; z = 0) \exp (i k_z z) . \quad (2.14)$$

2.3. Angular spectrum representation

In the previous section we obtained a description for the propagation of a single plane wave. Now we use plane waves as a basis, expressing an arbitrary field as a combination of plane waves. Knowing the initial fields at $z = 0$ [$E(x, y; z = 0)$] we can take the Fourier transform of the fields, expressing the fields in terms of plane

2. Basic theory

waves (with given k_x, k_y):

$$\tilde{E}(k_x, k_y; z = 0) = \frac{1}{4\pi^2} \int \mathbf{E}_0(x, y, z = 0) \exp(-ik_x x - ik_y y) dx dy. \quad (2.15)$$

The advantage of this representation (*angular spectrum representation*[23]) is that we have a solution for the propagation problem of a plane wave. We already noted that after propagating through distance z the plane wave acquires a phase $\exp(ik_z z)$. This means that the expression for propagated fields (in the angular spectrum representation is given by eq. (2.14)

$$\tilde{E}(k_x, k_y; z) = \tilde{E}(k_x, k_y; z = 0) \exp(ik_z z),$$

noting that k_z is a function of k_x and k_y . As we know the plane wave coefficients after the propagation we can obtain the real space image by taking the inverse Fourier transform

$$E(x, y; z) = \int \tilde{E}(k_x, k_y; z) \exp(ik_x x + ik_y y) dk_x dk_y. \quad (2.16)$$

Equation (2.14) is the fundamental equation that we use throughout this thesis, along with eqs. (2.15) and (2.16). We shall refer to the $k_z(k_x, k_y)$ component of the wavevector as the propagation constant,² as it describes propagation of the plane wave component (given by k_x, k_y) along the propagation axis (z axis).

2.4. Wave propagation in anisotropic media

2.4.1. Dispersion relation in anisotropic media

So far we have assumed an isotropic medium, described by (relative) dielectric permittivity ε and magnetic permeability μ . Now we extend these results for anisotropic media and see that the angular spectrum representation works equally well here. Indeed, in eqs. (2.15) to (2.16) we only assumed that we can express the fields in terms of plane waves and we can get the propagation constant k_z from the dispersion relation [eq. (2.13)]. These assumptions always hold in a homogeneous medium, so we just need to derive the dispersion relation for an anisotropic medium.

²This is a somewhat unfortunate name, as in the angular spectrum representation k_z is quite clearly not a constant: it depends on k_x and k_y . However, the term is already widely used in similar contexts, for example when discussing propagation of guided modes in waveguides.

2.5. Summary

We are interested in uniaxial anisotropic dielectric media, so while relative permittivity is now given by a dielectric tensor $\hat{\varepsilon} = \text{diag}(\varepsilon_e, \varepsilon_o, \varepsilon_o)$ we still assume isotropic magnetic permeability.³ Equation (2.5) now reads [20]

$$\mathbf{D} = \varepsilon_0 \hat{\varepsilon} \mathbf{E}. \quad (2.17)$$

Assuming plane wave [eq. (2.12)] can write the wave equation [eq. (2.7)] as

$$\mathbf{k} \times (\mathbf{k} \times \mathbf{E}) + k_0^2 \hat{\varepsilon} \mu \mathbf{E} = 0. \quad (2.18)$$

Seeking nontrivial solutions to the equation above we get

$$(k_x^2 + k_y^2 + k_z^2 - k_0^2 \varepsilon_o) ((-k_0^2 \varepsilon_e + k_y^2 + k_z^2) \varepsilon_o + k_x^2 \varepsilon_e) k_0^2 = 0. \quad (2.19)$$

From the first term we can identify the isotropic dispersion relation for the ordinary wave,

$$k_x^2 + k_y^2 + k_z^2 = \mu k_0^2 \varepsilon_o, \quad (2.20)$$

while the second term gives the anisotropic dispersion relation, which we can write in the usual form as

$$\frac{k_x^2 + k_y^2}{\varepsilon_e} + \frac{k_z^2}{\varepsilon_o} = \mu k_0^2. \quad (2.21)$$

Given rotational symmetry in x - y plane we assume $k_y = 0$, without loss of generality, to the yield following expression for the propagation constant:

$$k_z = \pm \sqrt{\mu \varepsilon_o k_0^2 - k_x^2 \varepsilon_o / \varepsilon_e}. \quad (2.22)$$

2.5. Summary

In this chapter we started from Maxwell's equations and derived equations describing plane wave propagation both in isotropic [eq. (2.13)] and anisotropic media [eq. (2.21)]. We also introduced angular spectrum representation, which allows us to decompose arbitrary fields in term of plane wave components and then calculate propagation of the fields.

³For a procedure to derive a dispersion relation under general conditions (i.e. no assumptions on form of permittivity and permeability tensors) we refer to ref. 44.

3. Hyperbolic metamaterials

3.1. Introduction

If we were limited by natural materials, then the discussion would be limited to cases where ordinary and extraordinary permittivities (in case of an uniaxial medium) are relatively close. However, by using metamaterials we can have media, where the two permittivities are of opposite signs. Roughly speaking this kind of medium would be “metallic” in some directions (characterized by negative permittivity) and “dielectric” in others (exhibiting positive permittivity). Only media with positive permittivity allows propagation of optical waves. Therefore we have medium where waves can propagate in some directions, but not in others.

In this chapter we will explore the properties of hyperbolic metamaterials (HMMs) along with ways to realize such structures experimentally. It turns out that although they exhibit relatively exotic properties, the implementations of such media are well within the realm of real experiments. The focus of this chapter is on optical hyperbolic metamaterials, so in laying out the theoretical background I describe the HMMs in terms of optical properties (dielectric permittivity). However, at the end of the chapter I will describe the acoustic HMMs as well and compare to the optical case.

The dispersion relation [eq. (2.21)] gives the set of allowed plane waves that are able to propagate in the medium. In isotropic case the equation describes a sphere in k -space, reflecting the fact that the wave propagation is isotropic. That is, the length of the wavevector (wavenumber) does not depend on the propagation direction. However, not only are hyperbolic metamaterials anisotropic, the two components of the permittivity tensor have opposing signs. In this case the dispersion relation eq. (2.21) describes a hyperboloid (thus the name hyperbolic metamaterials), illustrated in fig. 3.1.

One particularly noteworthy property of such media is the unbounded shape of the isofrequency contour. This means that for a given frequency the wavenumber of a plane wave mode is unbounded, i.e. there exists waves with very short effective

3. Hyperbolic metamaterials

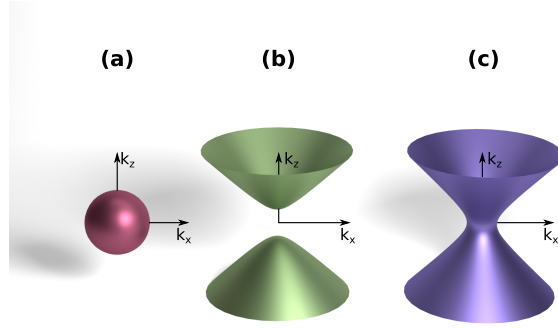


Figure 3.1.: Isofrequency contours for an isotropic medium (a), type-I HMM (b) and type-II HMM (c). Type-I HMM is obtained when the extraordinary permittivity tensor component is negative (i.e. $\varepsilon_e < 0$), while for type-II hyperbolic dispersion the ordinary component must be negative (i.e. $\varepsilon_o < 0$).

wavelengths.¹ We can also see from the expression for the propagation constant k_z [eq. (2.22)] to see that in case of hyperbolic media the propagation constant k_z will stay real for all k_x , given that term under the square root will always be positive.

There are two configurations to obtain hyperbolic dispersion: we can either have $\varepsilon_e < 0 < \varepsilon_o$ or $\varepsilon_o < 0 < \varepsilon_e$. These are classified as type-I [fig. 3.1(b)] or type-II HMMs [fig. 3.1(c)], respectively [14, 45]. From the expression for the propagation constant [eq. (2.22)] we note that the asymptotic behavior for $k_x \rightarrow \infty$ of both cases results in²

$$k_z \propto k_x \sqrt{|\varepsilon_o| / |\varepsilon_e|}, \quad (3.1)$$

indicating that for so-called high- k waves the behavior is the same: the propagation constant k_z stays real for arbitrarily large k_x , meaning that high- k are propagating waves (not evanescent as in traditional media).

However, for low- k waves the two types of HMMs show drastically different behaviour. For $k_x = 0$ we have

$$k_z = \sqrt{\varepsilon_o} k_0, \quad (3.2)$$

from which we see that for type-II HMMs the expression under the root will be

¹Of course, this is true only in theory. In practice there indeed is a bound on the effective wavelength, stemming from finite size of unit cells of metamaterials. This will be shortly discussed in section 3.3.3.

²The dispersion relation is rotationally symmetric, so for this discussion we can freely set $k_y = 0$ and only consider k_x and k_z .

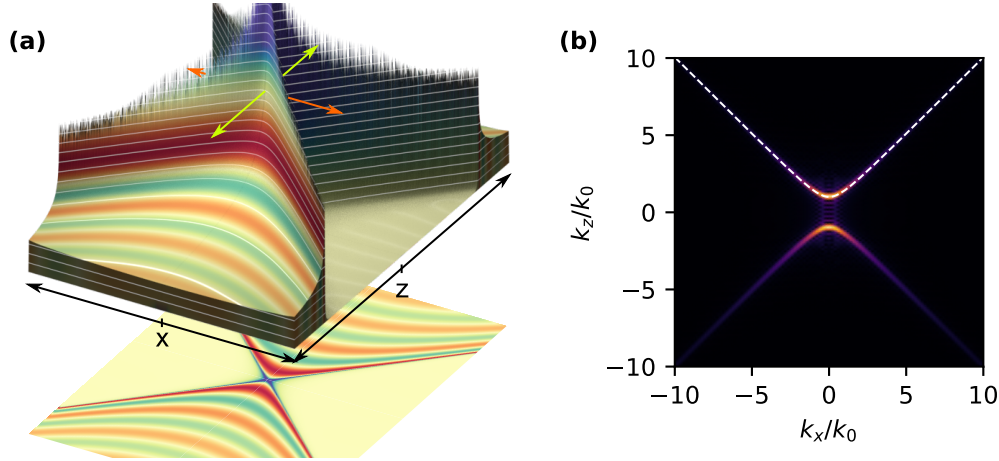


Figure 3.2.: (a) Magnetic fields from a point source in a homogeneous hyperbolic medium (with parameters in the text). Due to numerical considerations a loss factor $\gamma = 10^{-5}$ was used, which accounts for the small decay of the fields. (b) Fourier transform of the fields, indicating hyperbolic structure. As attenuation of waves scales with wavevector \mathbf{k} , there is noticeable attenuation of high- \mathbf{k} waves despite the low loss factor used. White dashed line shows propagation constant per the dispersion relation, given by eq. (2.22).

negative, leading to imaginary propagation constant. This means that in a type-II HMM these low- \mathbf{k} waves will be evanescent waves (not propagating). We will in chapter 5 use this property to discuss a possible dark-field subwavelength imaging device (dark-field hyperlens).

3.2. Wave propagation in HMMs

3.2.1. Homogeneous HMM

Having covered the mathematical groundwork of HMMs it is helpful to see these properties in action. In this section we will explore some basic configurations and show numerical simulation results of simple model problems. This allows to develop some insight, which will be useful in later sections, where we explore more practical systems. By observing the key properties of HMMs in idealized system it will be easier to reason about results seen from more complicated systems.

First we look at a fields originating from a point source in a homogeneous type-I

3. Hyperbolic metamaterials

hyperbolic medium

$$\varepsilon_o = 1 + \gamma i, \quad (3.3)$$

$$\varepsilon_e = -1 + \gamma i. \quad (3.4)$$

We have included the loss term γ , but for most of the discussion we assume loss-less case ($\gamma = 0$). However, for numerical simulations we include small losses to improve numerical behavior of the simulation. Figure 3.2(a) shows the field pattern of a point source in a HMM, which is quite different from usual wave behavior in isotropic media: we see that energy is mostly contained in for narrow beams propagating away from the source.

To understand the reasons for such propagation we can think of waves in a hyperbolic medium as propagating waves in one direction and non-propagating waves in the other(s):³ when waves propagate towards z -direction they only feel the ordinary component of permittivity tensor (ε_o). However, a wave propagating in the x -direction only interacts with the ε_e component of the permittivity tensor. In the case of waves with wavevector in z -direction the waves feel the positive component of the permittivity tensor, thus being propagating waves. On similar ground the waves in x -direction are evanescent. Now, when looking at wave propagating in direction that lies between the two axes it feels an “effective” permittivity composed of both the positive and negative component of the permittivity tensor. Thus, depending on the angle the effective permittivity can be either positive or negative — corresponding to either propagating or evanescent nature of the fields. In fig. 3.2(a) we notice four “characteristic lines” originating from the point source. These lines correspond to propagation direction where the effective permittivity for the wave changes sign.

Mathematically the propagation is governed by the dispersion relation [eq. (2.21)]. Earlier we discussed the dispersion relation of a hyperbolic medium (fig. 3.1). To see which plane wave components are present in fig. 3.2(a) we can use Fourier transform to arrive at k -space plot of the fields [fig. 3.2(b)]. As expected, the figure matches with theoretical results using the dispersion relation, as only components allowed by the dispersion relation can exist in the system. The k -space plot also in-

³This is a rough description, with some details neglected for now. For example, in anisotropic media direction of propagation and wavevector generally do not coincide, so here we talk about direction of propagation very loosely. Furthermore, using the term propagation direction for evanescent waves is somewhat questionable as well. Nevertheless, this way of thinking about the hyperbolic dispersion can still be useful forming basic understanding of the wave behavior. We also return to this simple model when introducing hyperbolic surface waves in chapter 7.

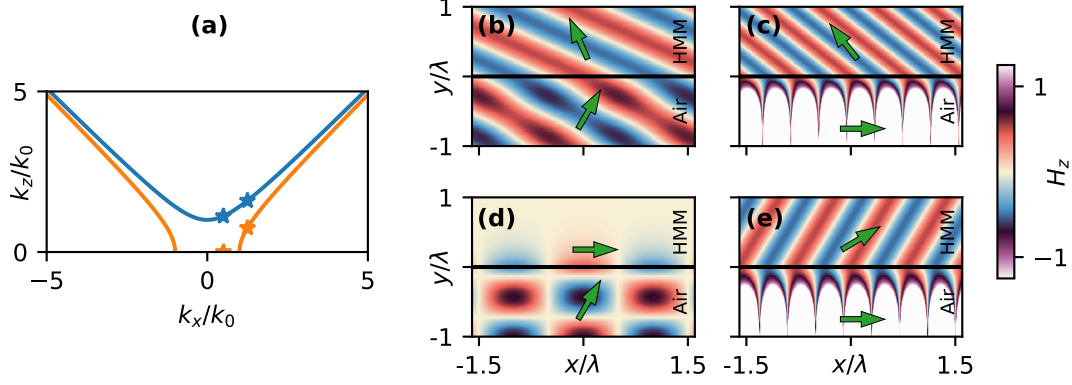


Figure 3.3.: (a) Isofrequency contours for a type-I and type-II HMM discussed in the text. Markers indicate selected points for field plots. (b-e) Reflection and transmission of plane wave from air into a type-I HMM (b,c) or a type-II HMM (d,e). Both low-k ($k_x = 0.5k_0$; b,d) and high-k ($k_x = 1.25k_0$; c,e) cases are shown. Green arrows indicate direction of Poynting vector for the incoming plane wave in air and the refracted wave in the HMM.

indicates the reason why energy is mostly contained in the four "characteristic lines". Propagation direction of the constituent modes is given by normal of the the isofrequency contour [15, 46]. Now, looking at modes present [fig. 3.2(b)] we note that there exists a large amount of modes on the flat part of the dispersion relation. All these waves travel along the characteristic line, leading to concentration of energy there.

3.2.2. HMM-dielectric interface

We now continue with exploring how an interface between a HMM and a dielectric behaves. Before looking at fields from a point source we shall first consider a simple case of a plane wave. We consider (and compare) a type-I HMM ($\epsilon_o = 1$, $\epsilon_e = -1$) and a type-II HMM ($\epsilon_o = -1$, $\epsilon_e = 1$). By plotting the dispersion relation [fig. 3.3(a)] we see that while the type-I medium allows propagation of waves with all k_x , in the type-II HMM waves with k_x below cut-off (so-called low-k waves) are nonpropagating. This is further demonstrated by the field pattern of an incoming plane wave [fig. 3.3(b,d)]. For a low-k wave ($k_x = 0.5$) we see that in the type-II HMM the wave is reflected from the interface, as the propagation is disallowed in the low-k regime. For the type-I HMM the wave propagates freely in the hyperbolic medium. In fig. 3.3(c,e) we see that for high-k waves both kinds of hyperbolic

3. Hyperbolic metamaterials

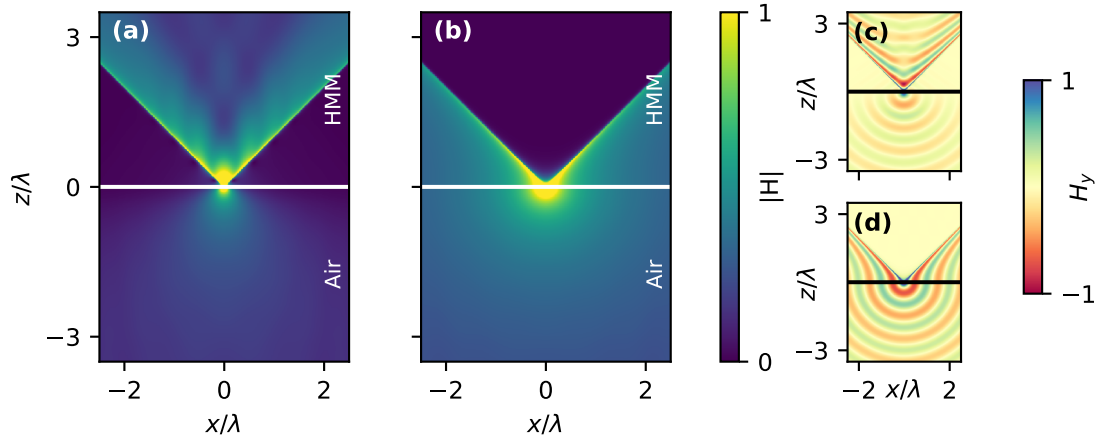


Figure 3.4.: Intensity of fields due to a point source on an interface between air and a type-I HMM (a) or type-II HMM (b). Corresponding field plots are shown in (c,d).

media allow propagation of the wave. However, here we note due to the high k_x the incoming wave is evanescent in the dielectric medium (air).

Another difference between the two HMM kinds is energy propagation direction of the waves. As highlighted in fig. 3.3 the waves in type-I HMM exhibit negative refraction.

We now consider a point source on the interface between a HMM and air. In fig. 3.4 we see the behavior of both type-I [fig. 3.4(a)] and type-II [fig. 3.4(b)] HMMs. We see that the general behavior for this case matches the results of a point source in a homogeneous medium (fig. 3.2), as could be expected.

More interesting results emerge when we place the point source in air some distance away from the interface. Then two processes occur while waves propagate from the point source towards the interface: (1) evanescent waves decay with going further from the source, with waves with higher k decaying faster and (2) propagating waves will acquire phase during the propagation. First we shall look at type-II medium: in fig. 3.5 we show point source at three different distances. By moving the source a small distance $d = \lambda/20$ [fig. 3.5(b)] the field pattern stays more or less similar, although we can notice reduction of high- k beam intensity. This is due to attenuation of (evanescent) high- k waves in the air, even after this short distance. By moving the source even further $d = \lambda/2$ [fig. 3.5(c)] the evanescent decay of high- k waves means that only a small part of evanescent fields is still present at the interface. Note that the cut-off of HMM ($k_c = k_0$) is also cut-off of evanescent waves (for which $k_x > k_0$). Therefore we see almost no propagating fields in the HMM.

Now we will consider similar case, but for type-I HMMs. In fig. 3.6 we show fields

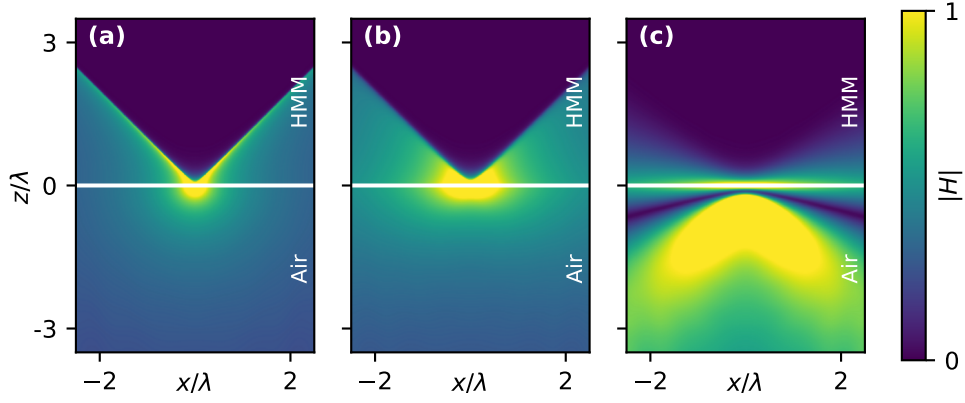


Figure 3.5.: Field intensity due to a point source (in air) at $z = 0$ (a), $z = -\lambda/20$ (b) and $z = -\lambda/2$ (c), near a type-II HMM.

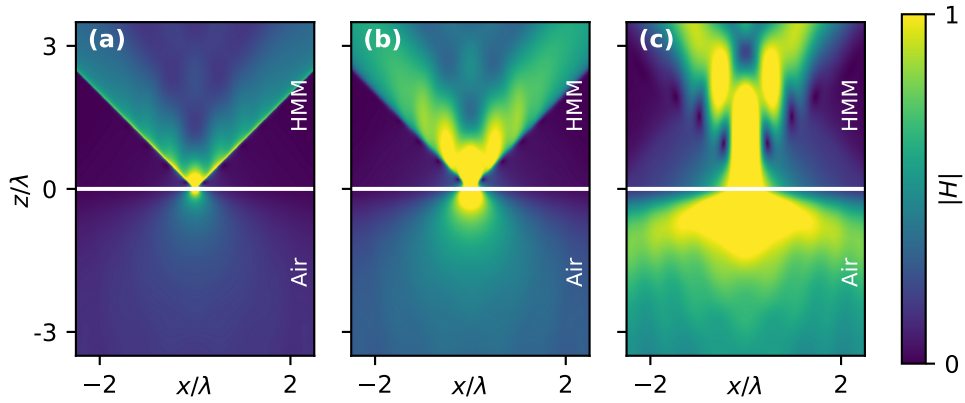


Figure 3.6.: Field intensity due to a point source (in air) at $z = 0$ (a), $z = -\lambda/20$ (b) and $z = -\lambda/2$ (c), near a type-I HMM.

3. Hyperbolic metamaterials

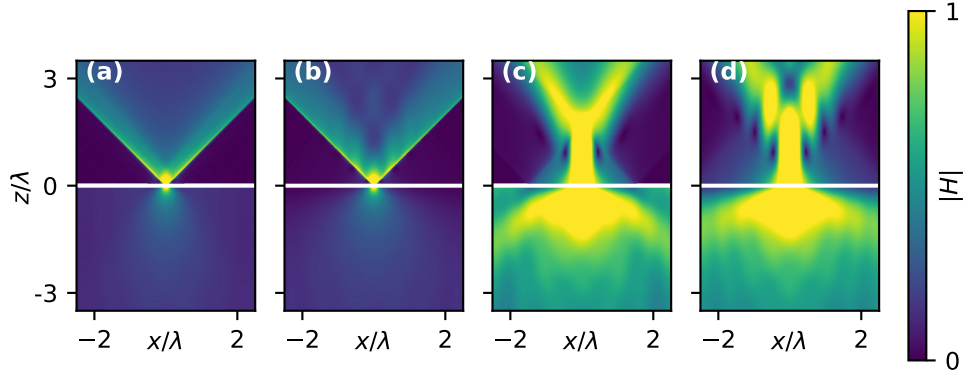


Figure 3.7.: Field intensity due to a point source on the interface (a,b) or $\lambda/2$ away from the interface (c,d) between air and type-I HMM. In (a,c) a PEC pinhole is used to limit the amount of waves refracting into the HMM.

from point source at different distances from the HMM interface. In contrast with type-II HMM there is no cutoff for low- k waves so we see propagating fields even when the source is further away from the HMM. However, as was the case for type-I HMM we note that as the source is moved further from the interface the intensity of the high- k peak drops: while it is clearly visible in fig. 3.6(a), it disappears for larger separations. This again is due to evanescent decay of the high- k modes that would form the high- k beams.

Also we point out that here one can also see the negative refraction of type-I HMM (already discussed in fig. 3.3). This is mostly evident in fig. 3.6(c) where the fields from the point source undergo a focusing effect in HMM.

Negative refraction & interference pattern in type-I HMM In simulations of type-I HMM [fig. 3.6] an interference pattern appears, which does not appear in type-II HMM [fig. 3.5]. This interference is caused by negative refraction of type-I HMM. The part of the field that propagates along the interface (oblique incidence) negatively refracts into the HMM and then shows up as this interference pattern. To clarify the role of negative refraction and interference we show additional simulations in fig. 3.7, where we place a perfect electric conductor (PEC) pinhole on the interface. This way we can prevent these oblique waves from refracting into the HMM.

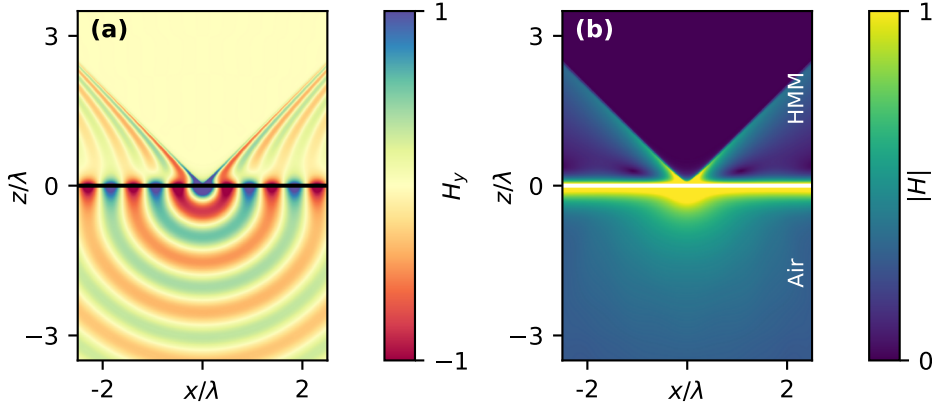


Figure 3.8.: Field (a) and intensity (b) plots of a point source in interface between air and a type-II HMM. Compared to fig. 3.4(b) permittivity of HMM is altered ($\varepsilon_e = 3$) to allow for surface mode to exist.

Surface mode between a type-II HMM and a dielectric It should be noted that in some cases HMM-dielectric interface can support surface waves. A surface wave is characterized by evanescent decay on both sides of the interface [5, 47]. This immediately rules out type-I HMM,⁴ however a type-II HMM can support a surface wave. We shall not go into details at this point (we will cover surface waves in depth in chapter 7), but we note that in an isotropic dielectric medium the evanescent waves occur when $k_x > \sqrt{\varepsilon}k_0$. For type-II HMM the evanescent mode exists in low- k cutoff regime, given by $k_x < \sqrt{\varepsilon_e}k_0$ [as we will show in eq. (5.1)]. From here it follows that a surface mode can exist on the interface if $\varepsilon < \varepsilon_e$ is fulfilled.

For example, in fig. 3.4(b) we see no surface mode, as permittivity of the dielectric ($\varepsilon = 1$) equals extraordinary component of permittivity tensor of the HMM ($\varepsilon_e = 1$). However by increasing ε_e (or decreasing permittivity of the dielectric) we reach conditions for evanescent modes in both media. In fig. 3.8 these conditions are fulfilled, enabling the surface mode. We see that there is localization of energy on the interface, indicating existence of a surface mode. We also see interference between the surface modes and propagating modes in the HMM.

Structure of waves propagating in a HMM In fig. 3.9 we illustrate the structure of wave propagation in the hyperbolic medium. Recalling the isofrequency contour we note that waves just above cut-off k_c will propagate along the interface and with

⁴As k_z is real for all k_x , the waves in type-I HMM are always propagating. Thus the condition for surface mode can not be satisfied.

3. Hyperbolic metamaterials

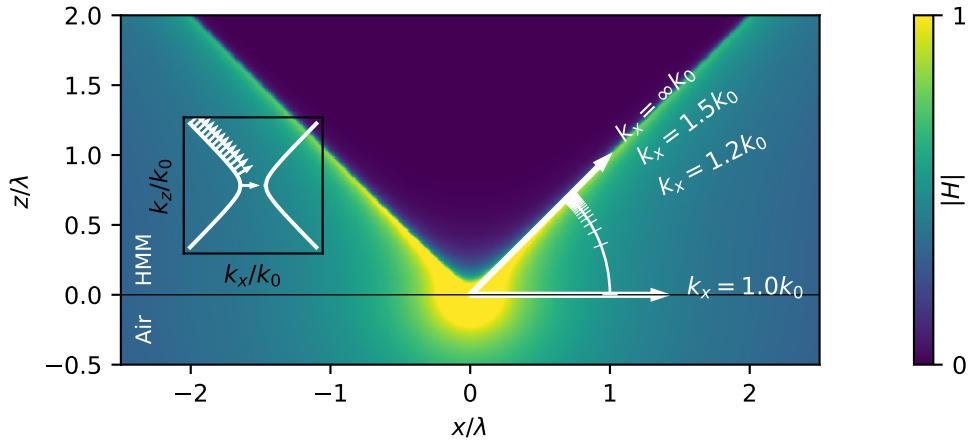


Figure 3.9.: Composition of fields from a point source on a HMM-dielectric interface. Propagation direction of plane wave components is indicated on the figure, showing that most of the components propagate along the two narrow beams. Inset show isofrequency contour for the HMM, where propagation directions are also shown with small arrows.

increasing k_x the propagation angle also increases. As the dispersion flattens out the wave with larger k_x values all propagate in the same direction, forming the narrow beam visible in the figures.

3.2.3. Canalization ratio & propagation direction

So far we have been looking at a simplified case of $\varepsilon_{o,e} = \pm 1$. Let us now explore the effect that different permittivities can have. From eq. (3.1) (giving asymptotic dispersion relation for large k_x)

$$k_z \propto k_x \sqrt{-\varepsilon_o/\varepsilon_e} \quad (3.1)$$

we note that an important role is played by the ratio $\varepsilon_o/\varepsilon_e$. Here we define the “canalization ratio”⁵

$$\xi^2 = -\varepsilon_e/\varepsilon_o, \quad (3.5)$$

which (as we will show) is the key parameter describing wave propagation in (type-I) hyperbolic media. In fig. 3.10(a) we show isofrequency contours of HMMs with varying canalization ratio. We see that increasing canalization ratio makes the dispersion relation “flatter”. Recalling the relationship between dispersion relation and

⁵We will come back to the term “canalization” in section 4.3.2, where the origin of the term becomes clear.

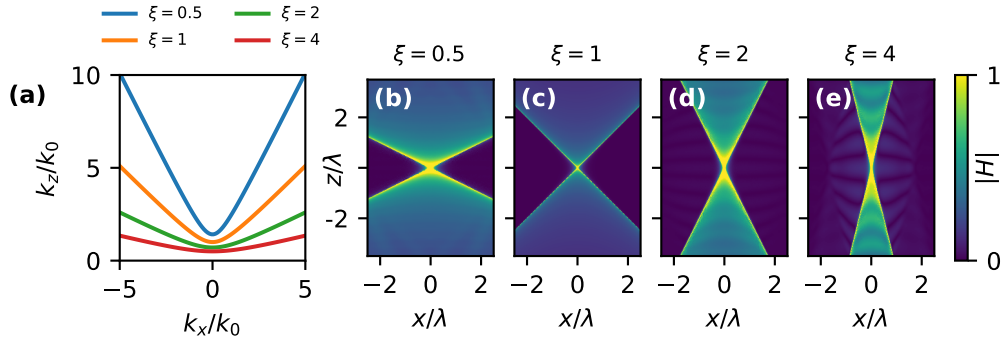


Figure 3.10.: (a) Isofrequency contours with type-I HMM with varying canalization ratio. Permittivities for the HMMs are given by $\varepsilon_o = \xi^{-1}$, $\varepsilon_e = -\xi$ (b-e) Simulations showing fields from a point source in a HMM with $\xi = 0.5$ (b), $\xi = 1$ (c), $\xi = 2$ (d) and $\xi = 4$ (e).

energy propagation direction we note that the propagation angle of the beams decreases with increasing canalization ratio [fig. 3.10(b-e)], meaning that fields propagate in a narrower cone.

3.2.4. Losses and hyperbolic media

The discussion so far was focused on lossless materials (i.e. real ε). However, for any practical experiment we need to consider the role of losses as well. Firstly, we note that equations we have relied on still hold, even in case where ε are complex — during the derivations we did not assume lossless media at any point. However, the nature of the propagation will be altered. Unlike purely real and imaginary propagation constants for high-k and low-k waves (respectively) the propagation constant is now a complex number. For low-k waves it is predominantly imaginary as the low-k waves are still evanescent in nature. However, high-k waves have now a imaginary component as well, due to material losses. In lossless HMM (or very small losses) the system can support wave with very high k [as seen in fig. 3.2(b), for example]. As we see from the propagation constant [eq. (2.22)] the losses scale with k_x so waves with higher k are more strongly affected by the losses.

As the losses primarily affect the high-k waves that are crucial in forming the narrow propagating beam, we expect that increasing losses will result in a deterioration (e.g. broadening) of the beam. Also the attenuation brought on by losses will mean that thicker HMM slabs become less practical, since the energy is dissipated into ohmic losses as propagating fields decay away. We illustrate these processes

3. Hyperbolic metamaterials

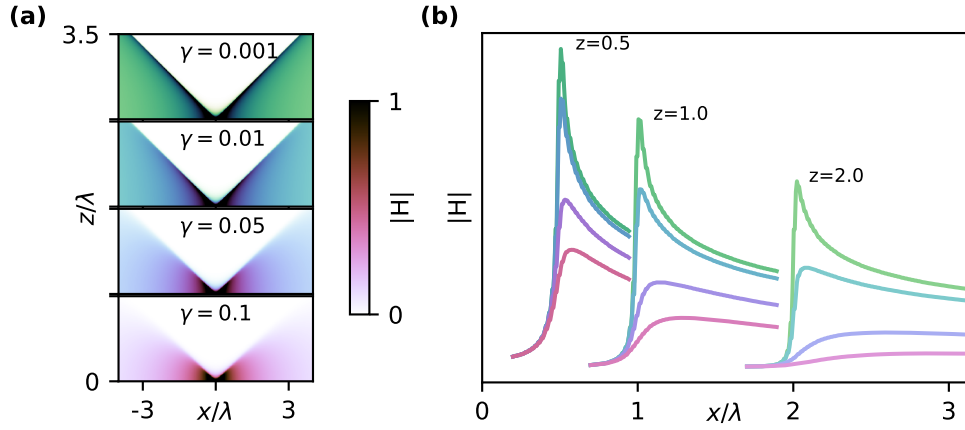


Figure 3.11.: Propagating fields due to a point source in a HMM with varying losses (a). Field slices at three different distances are shown in (b). Different loss factors are indicated by colors.

in fig. 3.11. Looking at propagation from a point source in a homogeneous HMM we see in fig. 3.11(a) that the “characteristic lines” of the hyperbolic medium get weaker with increasing losses. Also we note that the total intensity drops and as explained above, limits the maximum useful thickness of HMM.

Looking at the propagated fields after different propagation distances [fig. 3.11(b)] we see that in case of short propagation distance ($z \sim 0.5\lambda$) we have a well-formed narrow beam even with relatively high losses. However, as we go further the beam is strongly attenuated and broadened, reducing its usefulness. As we see, even for quite low losses the attenuation of high- k waves is strong enough to affect the propagating waves after some distance.

3.3. Multilayer structures as HMMs

3.3.1. Effective medium approximation

Although the properties of hyperbolic metamaterials are indeed somewhat exotic, it turns out that they can be realized in practice, with a suprisingly simple approach. Namely multilayer structures (or equally well, trench structures) can be effectively characterized as hyperbolic media, given that the structure period is well below wavelength.

Lets consider a periodic multilayer structure composed of ε_1 and ε_2 , with respective thicknesses d_1, d_2 . When looking at a single period of the structure and assum-

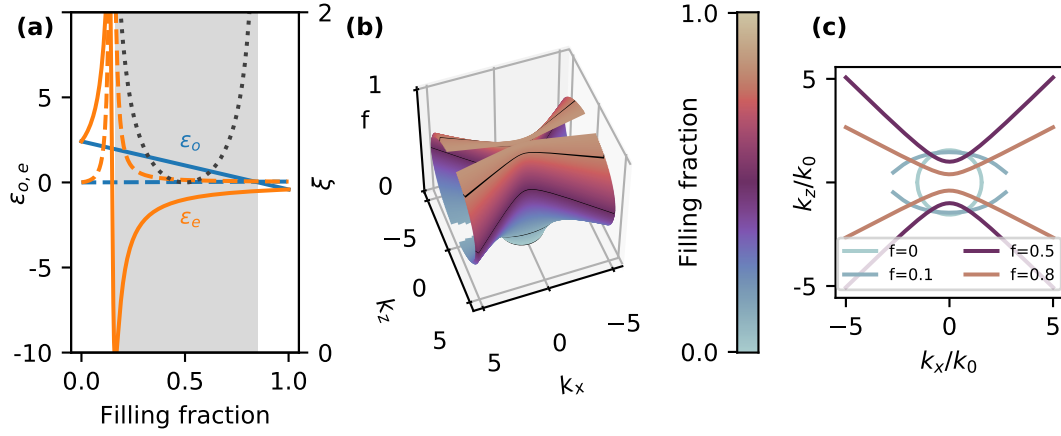


Figure 3.12.: (a) Effective medium parameters as function of filling fraction f of the metal (ϵ_2). Dashed lines indicate imaginary parts and the dotted line indicates canalization ratio ξ . (b) Isofrequency contours of the resulting effective medium as function of filling fraction f . For selected filling fractions (indicated by black lines) we show isofrequency contours also in (c).

ing that $d_1 + d_2 \ll \lambda$, we can use the electromagnetic interface conditions to reason about the average fields in the structure. Given our assumption of constant fields within the layers we can write the electric fields in first and second layer as

$$\mathbf{E}^{(i)} = E_x^{(i)} \hat{\mathbf{x}} + E_y^{(i)} \hat{\mathbf{y}} + E_z^{(i)} \hat{\mathbf{z}}. \quad (3.6)$$

From the electromagnetic interface conditions we have

$$E_x^{(1)} = E_x^{(2)}, \quad (3.7)$$

$$E_y^{(1)} = E_y^{(2)}, \quad (3.8)$$

$$\epsilon_1 E_z^{(1)} = \epsilon_2 E_z^{(2)}. \quad (3.9)$$

Now we look at the effective permittivity tensor, given by

$$\langle \mathbf{D} \rangle = \epsilon_0 \hat{\epsilon} \langle \mathbf{E} \rangle, \quad (3.10)$$

where $\langle x \rangle = (d_1 x_1 + d_2 x_2) / (d_1 + d_2)$ is used to indicate spatial average over the multilayer structure. From eq. (3.10) we can write

$$\epsilon_{ij} = \langle D_i \rangle / \epsilon_0 \langle E_j \rangle. \quad (3.11)$$

3. Hyperbolic metamaterials

Applying the interface conditions we reach a result that in effective medium approximation [48] this multilayer is represented by uniaxial anisotropic permittivity tensor $\hat{\varepsilon} = \text{diag}(\varepsilon_o, \varepsilon_o, \varepsilon_e)$, with components given by

$$\varepsilon_o = f\varepsilon_1 + (1 - f)\varepsilon_2, \quad (3.12)$$

$$\varepsilon_e^{-1} = f/\varepsilon_1 + (1 - f)/\varepsilon_2, \quad (3.13)$$

where $f = d_1/(d_1 + d_2)$ is the volume filling fraction of the first medium (ε_1).

As an example let us consider multilayer structure, with material parameters

$$\varepsilon_1 = -0.41 + 0.05i,$$

$$\varepsilon_2 = 2.41,$$

for a metallic and a dielectric medium, respectively. The parameters above are chosen such that at filling fraction $f = 0.5$ the effective medium approximation yields familiar $\varepsilon_o = 1$, $\varepsilon_e = -1$. Of course this choice is completely arbitrary — later in this section we will discuss implications of limiting choices to realistic parameter ranges, but before that we aim to form a basic intuition about the effects of different parameters.

Plotting the effective permittivities from effective medium theory [eqs. (3.12) and (3.13)] in fig. 3.12(a) we notice that the two permittivity components can be of opposite sign (under suitable conditions), fulfilling the requirements for a HMM. As expected, losses in the metal mean that the effective medium approximation will also result in a lossy medium. We see that for our chosen parameters (with relatively low losses) the imaginary parts of effective medium parameters are relatively low, signifying that in general the losses will not necessarily destroy the hyperbolic behavior. Here the only regime where losses have an adverse effect is near $f \approx 0.15$, where (due to near-pole condition of $\varepsilon_e^{-1} \approx 0$) both real and imaginary part of ε_e reach high values. Of course, when dealing with metal with more high losses, the hyperbolic behavior can be more strongly affected.

The effective permittivity parameters themselves are not so straightforward to reason about. Instead, in fig. 3.12(b) we plot the isofrequency contours for varying filling fraction. At $f = 0$ we have the isotropic dielectric medium, which at first becomes a conventional (positive) anisotropic medium and from $f \approx 0.15$ onwards we see the hyperbolic dispersion. At the other end ($f = 1.0$) we have purely metallic

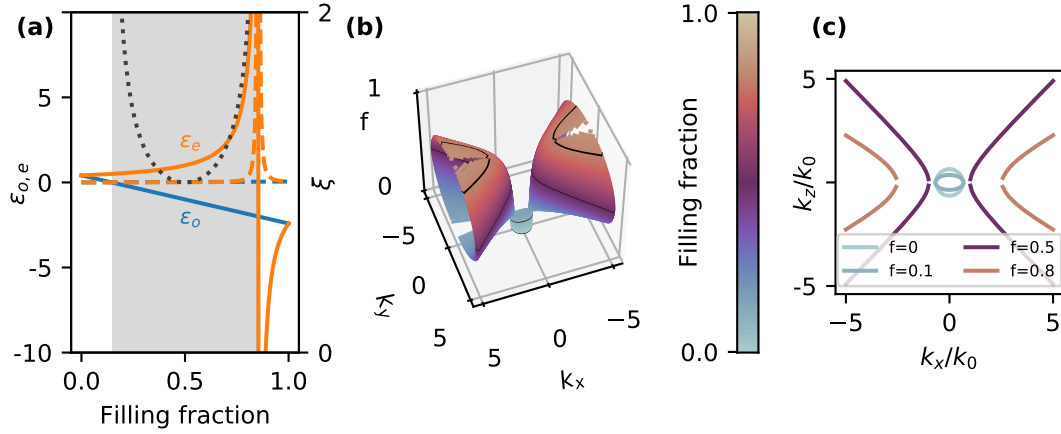


Figure 3.13.: (a) Effective medium parameters as function of filling fraction f of the metal. Dashed lines indicate imaginary parts and the dotted line indicates canalization ratio ξ . (b) Isofrequency contours of the resulting effective medium as function of filling fraction f . For selected filling fractions (indicated by black lines) we show isofrequency contours also in (c)

behavior, so there is no corresponding isofrequency contour as the medium does not support propagating waves in that configuration.

We see that tuning the filling fraction gives some control over the propagation properties in the HMM. In section 3.2.3 we discussed the importance of the canalization ratio $\xi^2 = \epsilon_e/\epsilon_o$, particularly for a type-I HMM, determining the "flatness" of the dispersion relation. From fig. 3.12(a) we see that the ratio is minimal when $f = 0.5$. This can also be seen from the shape of the isofrequency contours [fig. 3.12(b)], which are widest for the same filling fraction. By changing relative thicknesses of constituent layers we can thus tune the propagation direction in the HMM, without need to vary the constituent materials of the multilayer.

To clearly show changes in the dispersion relations we have plotted the isofrequency contours for chosen filling fraction in fig. 3.12(c). The figure outlines the transition from dielectric into hyperbolic medium and shows the varying shape of hyperbolic dispersion.

Crucially we see that given the material parameters we can only achieve type-I HMM. It is easy to demonstrate that for given material parameters only type-I or type-II HMM could be achieved. More precisely, to be able to obtain type-I HMM $\epsilon_1 > -\epsilon_2$ is required, and conversely $\epsilon_1 < -\epsilon_2$ will allow for type-II HMM.

To show the effect of filling fraction on type-II HMMs we similarly choose material parameters so that at $f = 1/2$ we reach effective medium with $\epsilon_o = -1$, $\epsilon_e = 1$:

3. Hyperbolic metamaterials

$$\begin{aligned}\varepsilon_1 &= -2.41 + 0.05i, \\ \varepsilon_2 &= 0.41.\end{aligned}$$

Of course, the materials here are chosen purely on mathematical grounds, with somewhat unrealistic dielectric medium with permittivity of less than unity.

In fig. 3.13(a) we again plot the effective medium parameters for the structure. The results are remarkably similar, although in the hyperbolic regime signs of ε_o , ε_e have been flipped compared to the previous case: now we have $\varepsilon_o < 0 < \varepsilon_e$, signifying type-II HMM. The change in dispersion relation is better visualized in fig. 3.13(b), where we once again show the dispersion relation for various filling fractions.

As in case of type-I HMM the canalization ratio is minimal for $f = 0.5$ and tuning filling fraction allows one to increase the canalization ratio. However, here unlike type-I HMM we have another important parameter to consider: the cut-off wavevector k_c , separating propagating high-k and evanescent low-k waves. As we see already from fig. 3.13(b,c) this parameter is also linked to the filling fraction. The cut-off k_c is given⁶

$$k_c^2 = \varepsilon_e.$$

In general we are interested in keeping the cut-off as low as possible since it allows capturing large amount of fields in the HMM. Secondly we note that high-k waves are by their nature much more sensitive to the material losses and as such will attenuate faster. With too high k_c so that only waves with high k are propagating in the system we end up being very sensitive to ohmic losses, which are especially relevant when we are planning to design structures with realistic material parameters.

3.3.2. Realistic material parameters

Now we turn to realistically achievable material properties. Here we shall consider two classic plasmonic metals: gold and silver in optical frequencies. In fig. 3.14(a) we classify the effective medium parameters obtained using silver and dielectric multilayer as a function of filling fraction and wavelength. To illustrate role of the dielectric we consider three different dielectrics, with $n = 1.5$, $n = 2.0$ and $n = 2.5$. We see that for a large part of the visible spectrum we can obtain type-II HMM, while

⁶This will be shown in chapter 5 in with eq. (5.1).

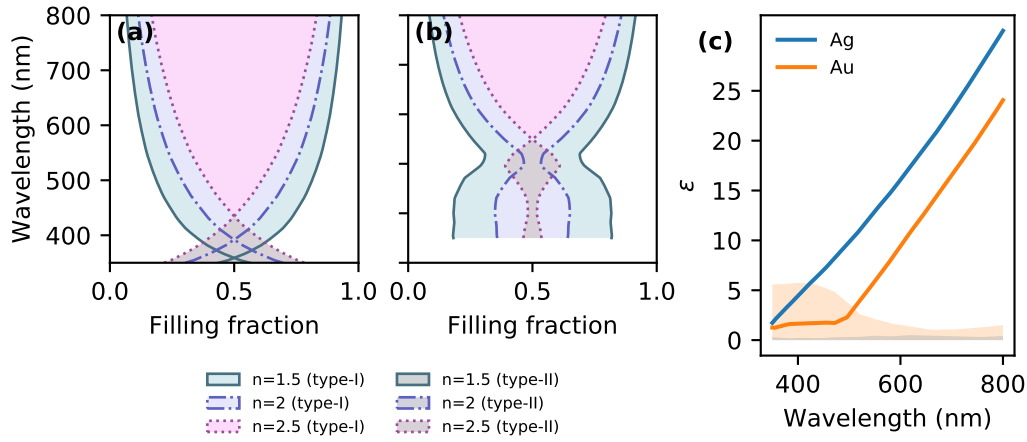


Figure 3.14.: Conditions for obtaining hyperbolic effective medium parameters for Ag (a) and Au (b). Shaded regions indicate areas where wavelength and filling fraction result in hyperbolic dispersion. Three different dielectrics are considered, as indicated in the figure. (c) Real part of permittivity for Au and Ag in optical range.

type-I hyperbolic dispersion is limited to short wavelengths. To achieve type-I HMM with multilayer structures small dielectric permittivity is required. From fig. 3.14(c) we see that for gold and silver this means using short wavelengths.

In fig. 3.14(b) we show a range of effective HMM parameters available for gold structures. However, strong losses due to the interband transitions in gold make it unsuitable for short wavelengths. This means that the regime where epsilon of the metal is small is somewhat impractical, as the losses strongly affect the effective medium approximation. This means that we can consider gold mostly for achieving type-II HMMs, where we can operate away from the very lossy regime.

In fig. 3.15 we further explore HMM properties available with metal-dielectric multilayers. Like we already saw in fig. 3.14(a), a high-index dielectric is required in order to push type-I regime into visible spectrum. Conversely a low-index dielectric is preferable in realizing type-II HMM, as it facilitates reaching lower canalization ratio ξ and lower low-k cut-off k_c .⁷

3.3.3. Limitations of the effective medium approach

It is important to stress that the long wavelength approximation has to hold for effective medium approach to work. In case of hyperbolic media this is even more important, as the high-k waves exhibit small effective wavelengths. Although in prin-

⁷We will cover reasons for aiming for low ξ and k_c in more detail in chapter 5.

3. Hyperbolic metamaterials

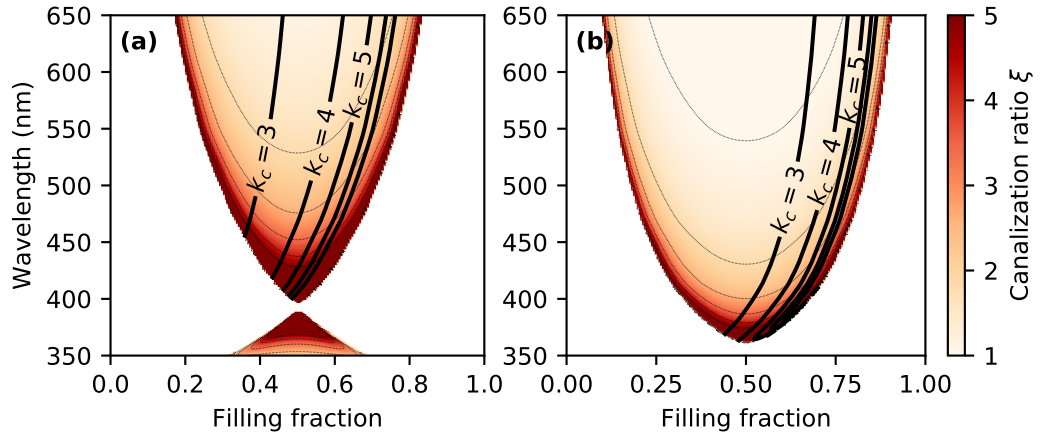


Figure 3.15.: Plots of canalization ratio ξ (indicated with color and gray lines) and low-k cutoff k_c (indicated with black lines) for silver-dielectric multilayer, with dielectric $n = 2$ (a) and $n = 1.45$ (b).

While a hyperbolic medium would support waves with arbitrarily small wavelengths, this does not hold for the effective medium theory. As the effective wavelength approaches periodicity of the structure the averaging procedure that underpins the effective medium theory is no longer valid. Therefore in reality the dispersion relation is not completely hyperbolic, as the high-k waves are not unbounded and the isofrequency surface is actually a closed surface [48].

It is also noteworthy that it is not only the high-k waves that one needs to be careful of. For example, as evanescent waves decay quickly, they interact the structure closer to the interface more strongly. This means that in case of a multilayer structure the first layer has a stronger effect than subsequent layers, in some cases invalidating the effective medium approach [49].

3.4. HMMs with magnetic properties

Usually the discussion regarding HMMs neglects magnetic properties (i.e. the relative permeability μ is taken to be unity). In previous pages we followed that practice. Given the difficulty of achieving magnetic properties in the optical regime this approach is usually justified. However, we now will include magnetic properties in the discussion to allow for more flexibility in our theoretical analysis. Though here we are motivated by theory, it should be noted that there have been reports of practical HMMs structures exhibiting magnetic properties in some form.

3.5. Hyperbolic metamaterials in acoustics

In deriving the dispersion equation

$$k_x^2/\varepsilon_e + k_y^2/\varepsilon_e + k_z^2/\varepsilon_o = \mu k_0^2, \quad (2.21)$$

in the last chapter we already allowed for the possibility of magnetic properties ($\mu \neq 1$). So far we have just assumed $\mu = 1$ and ignored implications of magnetic properties on the dispersion relation.

Lets now consider two hyperbolic media, first with $\mu^{(1)} = 1$ and a second one where $\mu^{(2)} = -1$. Supposing that we fix parameters of the two media with

$$\begin{aligned} \varepsilon_o^{(2)} &= -\varepsilon_o^{(1)}, \\ \varepsilon_e^{(2)} &= -\varepsilon_e^{(1)}, \end{aligned}$$

then the expressions for the propagation constant k_z seem equivalent for these two media:

$$\begin{aligned} k_z^2 &= \varepsilon_o^{(2)} \mu^{(2)} k_0^2 - k_x^2 \varepsilon_o^{(2)} / \varepsilon_e^{(2)} \\ &= \varepsilon_o^{(1)} \mu^{(1)} k_0^2 - k_x^2 \varepsilon_o^{(1)} / \varepsilon_e^{(1)}. \end{aligned} \quad (3.14)$$

However, we do need to carefully consider the signs for these expressions. For our purposes we are looking to deal with waves propagating towards positive z direction. For that we can take the corresponding component of the Poynting vector

$$S_z = \frac{|H_y|^2}{2\omega} \operatorname{Re} \left(\frac{k_z}{\varepsilon_o \varepsilon_x} \right) \quad (3.15)$$

and choose the sign of k_z such that $S_z > 0$. From here we see that the propagation constants for the two media have opposing signs, indicating reversed phase propagation direction with respect to each other. We will consider implications of this in chapter 6.

3.5. Hyperbolic metamaterials in acoustics

Acoustic wave equation Earlier we showed that from Maxwell's equations we can easily get to the (electromagnetic) wave equation eq. (2.7). Here we will follow ref. 50 in showing how to reach wave equation for acoustic waves. Instead of electric and magnetic fields the important physical quantities here are particle velocity \tilde{v} , pressure \tilde{p} and medium density $\tilde{\rho}$. We separate these into disturbance caused by the

3. Hyperbolic metamaterials

wave (v, p, ρ) and the rest values (v_0, p_0, ρ_0) :

$$\tilde{v} = v_0 + v, \quad (3.16)$$

$$\tilde{p} = p_0 + p, \quad (3.17)$$

$$\tilde{\rho} = \rho_0 + \rho. \quad (3.18)$$

These quantities obey Euler and continuity equations

$$\dot{\tilde{v}} + \tilde{v} \cdot \nabla \tilde{v} = -\tilde{\rho}^{-1} \nabla \tilde{p}, \quad (3.19)$$

$$\dot{\tilde{\rho}} + \nabla (\tilde{\rho} \tilde{v}) = 0. \quad (3.20)$$

We then obtain set of linear equations by inserting eqs. (3.16) to (3.18) into eqs. (3.19) and (3.20) and keeping only the first-order terms. As in chapter 2 we consider case of a homogeneous medium. Furthermore we assume that the medium itself does not move ($v_0 = 0$), i.e. only source of particle velocity is disturbance v due to the acoustic wave. With that we get

$$\ddot{p} - c^2 \nabla^2 p = 0, \quad (3.21)$$

where speed of sound c is given via density ρ and bulk modulus κ as [51]

$$c^2 = \frac{\kappa}{\rho}.$$

To consider time-harmonic waves we insert $p(t) = p \exp(-i\omega t)$ into eq. (3.21), giving (isotropic) wave equation for acoustic waves

$$\nabla^2 p + \omega^2 / c^2 p = 0. \quad (3.22)$$

Hyperbolic metamaterials As eq. (3.22) is derived for isotropic case, it is not sufficient to discuss acoustic HMMs. By assuming anisotropic response of the acoustic medium it is possible to derive the anisotropic dispersion relation for acoustic waves [38, 52]

$$\frac{k_x^2}{\rho_x} + \frac{k_y^2}{\rho_y} = \kappa^{-1} \omega^2, \quad (3.23)$$

which is the acoustic version of the dispersion relation we derived earlier [eq. (2.21)]. Here the effective mass density (ρ_x and ρ_y) is the analogue to dielectric permittivity and the effective bulk modulus κ mirrors permeability.

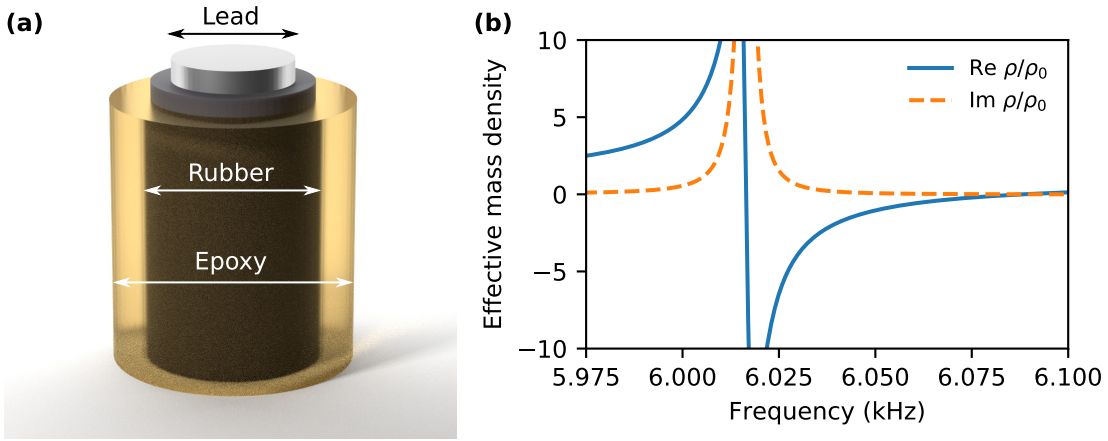


Figure 3.16.: (a) Resonator used to implement negative dynamic mass density. Radii of the lead, rubber and epoxy layers are 1.5 mm, 2.0 mm and 3.0 mm, respectively. (b) Calculated effective relative mass density of periodic arrangement of resonators placed in regular grid with 1 cm spacing.

The challenge in acoustics is that there are no natural materials where either mass density or bulk modulus is negative [37, 38]. While the static mass density must indeed always be positive, with resonant structures it is possible to achieve effective negative dynamic mass density for particular frequencies [53]. Chiang et al. [38] proposed an acoustic hyperbolic metamaterial, consisting of small cylindrical resonators [fig. 3.16(a)], arranged periodically (similar in idea to metal-dielectric multilayers in optics). Near the resonance frequency the vibrations of the cylindrical structures are out of phase with incident wave, leading to negative mass density response [fig. 3.16(b)]. A regular arrangement of such resonators produces an acoustic metamaterial, with an negative effective mass density. By having different grid spacing in x and y directions it is possible to tune the anisotropic effective mass density [38].

We will shortly return to this topic at the end of chapter 5, where we will present simulations of acoustic hyperlens.

3.6. Summary

In this chapter we introduced hyperbolic metamaterials and discussed how wave propagation in hyperbolic media differs from conventional media, where waves from point source radiate away in relatively uniform way. In HMMs the propagation is significantly different: waves propagate in narrow lines, corresponding to the di-

3. Hyperbolic metamaterials

rection were waves in HMM change in nature from propagating to non-propagating waves.

We also discussed interface between an dielectric and hyperbolic media. We showed that type-I HMMs exhibit negative refraction. We also discussed that type-II HMM interface can support a propagating surface wave.

We examined wave propagation in HMMs, introduced the canalization ratio ξ and showed how this relates to wave propagation properties of the HMM.

A practical design of HMMs (periodic metal-dielectric multilayer) was also discussed: we showed how hyperbolic dispersion could be achieved with both gold and silver multilayers and how choice of wavelength affects the resulting HMM dispersion.

4. Diffraction limit and subwavelength imaging

4.1. Diffraction limit

The angular spectrum representation introduced in section 2.3 gives a convenient theoretical framework for understanding the diffraction limit. We start by analyzing the propagation of fields from a point source. For simplicity we neglect the details of the vectorial nature of the electromagnetic fields for a moment. The point source is represented by a Dirac delta function¹

$$E(x) = \delta(x) . \quad (4.1)$$

According to our convention we are imaging in x - y plane, with light propagating in the z -direction. Following eq. (2.15) we take Fourier transform of our point source, reaching a result that the image contains all spatial frequencies $\tilde{E}(k_x) = 1$. Looking at the dispersion relation of isotropic medium

$$k_x^2 + k_z^2 = \varepsilon k_0^2 , \quad (4.2)$$

we notice that only waves with $k_x^2 \leq \varepsilon k_0^2$ have a real propagation constant k_z . For the rest of the waves the propagation constant is imaginary, indicating that these components decay exponentially away from the source. In the far field we have only propagating components left

$$\tilde{E}'(k_x) = \begin{cases} 1 & k_x^2 < \varepsilon k_0^2 \\ 0 & \text{otherwise} \end{cases} . \quad (4.3)$$

Taking the inverse Fourier transform [eq. (2.16)] gives an expression for fields in real space. However, with evanescent waves cut out during the propagation the image has effectively been through a low-pass filter. The resulting real-space image

¹Here we for simplicity assume fields to be constant in y direction.

4. Diffraction limit and subwavelength imaging

now as a form of

$$E'(x) = \frac{2 \sin(\sqrt{\varepsilon} k_0 x)}{x}, \quad (4.4)$$

which unlike the original point source has a finite width, related to the refractive index of the medium.

4.2. Devices for subwavelength imaging

4.2.1. Introduction

There are several routes to avoid the diffraction limit, as indicated by the popularity of several subwavelength imaging techniques. However, no method can escape the underlying diffraction limit, but there are ways around it. The simplest approach is to reduce the wavelength, thus improving the resolution. High-NA immersion microscopes also offer improvement in resolution, by increasing the refractive index and thus pushing the resolution a little bit further. More advanced techniques however rely on external factors to the diffraction limit. The scanning near-field optical microscope (SNOM) achieves high resolution by working in close proximity to the imaged object. In this way the exponential decay of high-k waves is can be overcome. The small tip of SNOM is used to convert the evanescent waves into propagating waves (either scattering in the free space or coupled into the fiber via the tip).

However, it is not necessary to work in the near field to achieve superresolution. Stimulated emission depletion microscopy (STED) [25, 26] microscopy works in the far field, but this time the diffraction limit is circumvented by having extra information about the imaged object. In STED microscopy a tightly focused laser beam is used to excite the emitters. Also an additional donut-shaped beam is used to suppress emitters in close vicinity of the focus. Due to this suppression we know that all the emitters imaged are located in a narrow region, below traditional diffraction limit. The high resolution here is achieved using selectively exciting the emitters, which due to depletion mechanics allow to achieve tighter focusing than traditional diffraction limit.

4.2.2. Superlens

Advances in metamaterials theory have opened up another avenue in subwavelength imaging. By substituting the traditional isotropic medium with a metama-

terial medium, we can avoid the the dispersion limit altogether.² Perhaps the first well-known idea came from Pendry, when he proposed the superlens [27]. He proposed to use a slab of negative-index metamaterial as a device to reconstruct the evanescent fields of the initial subwavelength source. I will not discuss the superlens idea in much detail, because the underlying details are quite different with HMM-based approach. However, some of the key points merit a mention.

Firstly it is important to stress that the high- k waves stay evanescent in the negative-index medium. Indeed by looking at the dispersion relation and the resulting isofrequency contour we note that it resembles the dispersion relation of a regular isotropic positive-index medium, albeit with reversed phase propagation direction. However, due to the boundary conditions of the interfaces of negative-index medium, the evanescent waves are restored in that medium. This means that the fields after the negative-index slab contain all the information they had before the slab (assuming, perhaps a bit too optimistically, there are no losses in the metamaterial). Although the superlens design does not offer any magnification and as such is not a suitable for subwavelength imaging by itself, it has been an interesting and motivating example of how metamaterials force a new look on underlying physics in optics.

4.3. Hyperlens

4.3.1. Introduction

The hyperlens is an application of HMMs to the subwavelength imaging problem [16, 18, 28, 29]. As we discussed in chapter 3 there are no evanescent waves in type-I HMM, all waves being allowed to propagate — thus no filtering of high- k waves and no diffraction limit in the medium. This means that a HMM slab can be used to function as a superlens, i.e. perfectly carrying the fields without attenuating the high- k waves (containing information about subwavelength details).

The hyperlens design however goes further: by use of cylindrical (or spherical) geometry the fields propagating through the HMM can be magnified, effectively transforming the high- k waves into low- k waves. This means that after propagating through the system the fields can be imaged using conventional far-field optics as now the image is above the diffraction limit of the far-field system.

As the first approximation³ we can write the dispersion relation of a cylindrical

²At least in the theory. In practice there are of course a range of issues to consider, ranging from losses to unit cell size of metamaterial limiting the effective medium approximation

³We will discuss the cylindrical case more rigorously in this thesis, but it should be noted that this

4. Diffraction limit and subwavelength imaging

HMM as

$$k_\theta^2/\varepsilon_r + k_r^2/\varepsilon_\theta = k_0^2, \quad (4.5)$$

where the components of the wavevector and permittivity tensor are in cylindrical coordinates instead of Cartesian coordinates. An important consequence of a cylindrical system is that the quantity $k_\theta r$ is conserved. It follows that the wavevectors are compressed as the fields propagate in the cylindrical system

$$k_\theta(r) = k_\theta(r_0) \frac{r_0}{r}, \quad (4.6)$$

corresponding to magnification of the image in the real space. This delivers the key feature of the hyperlens: magnification of the image from below diffraction limit so that the fields can be imaged using far-field optics.

4.3.2. Canalization regime

An important design goal of the hyperlens is to make sure that the fields from the inner to interface propagate to the outer interface with minimal distortions. In the lossless case this means that the phase acquired through propagation in the hyperlens should be same for all the plane wave components. This is achieved in the so called canalization regime. The name originates from an early proposal of a hyperlens based on a metamaterial consisting of a wire medium [54], where the modes propagating along individual wires carried the pixels of image through the hyperlens. Effectively the image is “canalized” from the inner to the outer interface. This effect is not limited to wire media, as similar behavior of (near) perfect image transmission is achievable in several of proposed hyperlens designs [28, 29, 55].

We shall now consider mathematical details of this canalization regime. For easier analysis we examine a planar HMM slab, avoiding additional complications arising from cylindrical geometry. In the end of the chapter we will justify the results in the context of cylindrical geometry.

Mathematically the idea of a canalization regime is to “flatten out” the dispersion relation. In this case the propagation constant is slowly varying for different transverse wavevectors, to the limit of being constant. With k_z becoming independent of k_x, k_y we can pull out the propagation term from eqs. (2.14) and (2.16) and we see

approximation holds very well, especially for type-I HMM.

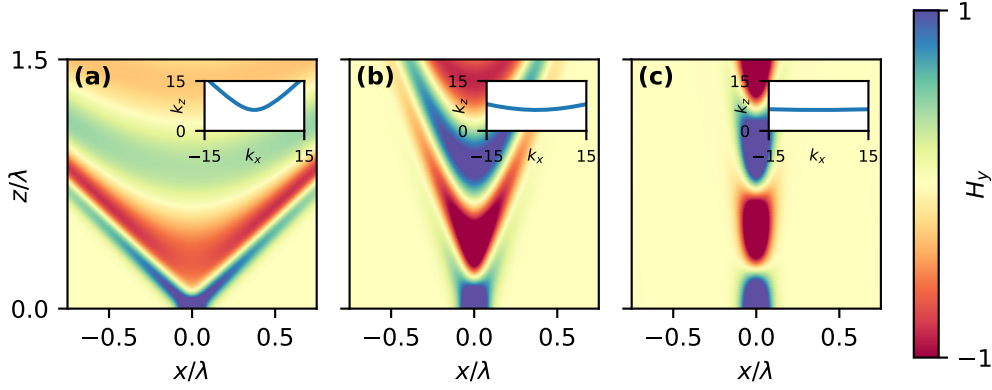


Figure 4.1.: Field propagation from Gaussian source in type-I HMM with various canalization ratios: $\xi = 1$ (a), $\xi = 3$ (b), $\xi = 9$ (c). Inset show isofrequency contour of the corresponding HMMs.

that the propagation equation reduces to

$$E(x, y, z) = \exp(ik_z z) \int \tilde{E}(k_x, k_y; z=0) \exp(ik_x x + ik_y y) dx dy \quad (4.7)$$

$$= \exp(ik_z z) \mathbf{E}_0(x, y, z=0). \quad (4.8)$$

We see that the fields only acquire a constant phase term but are otherwise unaffected. Looking at the expression for propagation constant in HMM [eq. (2.22)] we see that there are two ways to make k_z independent of k_x, k_y : either let $\varepsilon_o \rightarrow 0$ (in which case $k_z \rightarrow 0$) or let $\varepsilon_e \rightarrow \infty$, in which case $k_z \rightarrow \sqrt{\varepsilon_o} k_0$.

For reference, we shall review some of the proposed hyperlens designs to highlight the role of the canalization regime. We recall the canalization ratio from section 3.2.3

$$\xi^2 = -\frac{\varepsilon_e}{\varepsilon_o}, \quad (3.5)$$

which describes the degree of canalization: as ξ approaches infinity the system is more and more canalized. In fig. 4.1 we show that for practical purposes relatively small values of the canalization factor already yield sufficient flattening of the dispersion relation. As a practical point we note that the canalization factors for hyperlenses demonstrated in the literature are around 5–10 [18, 29–31].

4.4. Magnification in cylindrical hyperlens

4.4.1. Wave expansion in cylindrical system

Although appropriating the dispersion relation of a flat Cartesian system with eq. (4.5) is appealing and a quite good approximation, we shall also cover a rigorous approach to cylindrical hyperbolic media. For a proper analysis we shall leave the original equations (meant for Cartesian coordinates) behind and derive the dispersion equation straight for the cylindrical case, starting from the electromagnetic wave equation

$$\nabla \times (\hat{\varepsilon}^{-1} \nabla \times \mathbf{H}) = k_0^2 \mu \mathbf{H} . \quad (4.9)$$

Given cylindrical geometry we assume (TM) fields $\mathbf{H}(r, \theta) = F(r) \exp(im\theta) \hat{z}$, which after being inserted into eq. (4.9) yields a solution

$$H_z(r, \theta) = \exp(im\theta) \left[a H_\nu^{(1)}(k_r r) + b H_\nu^{(2)}(k_r r) \right] , \quad (4.10)$$

where $\nu = m \sqrt{\varepsilon_\theta / \varepsilon_r}$ and $k_r = k_0 \sqrt{\varepsilon_\theta}$. For a more straightforward comparison with plane waves we move from the angular momentum mode number m to the tangential wave number k_θ . We recall that a wave number represents the number of wavelengths per unit length, while the angular mode number m gives number of wavelengths per full rotation (2π). From here we see that $m = k_\theta r$. As m is fixed for a given wave component we get from $k_\theta r = k'_\theta r_0$ that

$$k_\theta = k'_\theta \frac{r_0}{r} , \quad (4.11)$$

which shows that as waves propagate through the cylindrical systems the wave vectors are compressed (corresponding to magnification of the image in real space).

4.4.2. Phase propagation in cylindrical system

A major convenience of plane waves is that the phase propagation can be straightforwardly expressed by

$$E_2 = E_1 \exp[ik_z(x_2 - x_1)] ,$$

where the phase acquired during propagation is just

$$\text{Re}(k_z)(x_2 - x_1) . \quad (4.12)$$

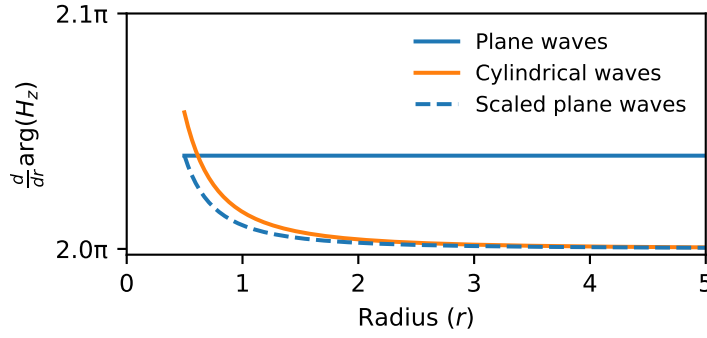


Figure 4.2.: Comparison of the of phase acquired during propagating assuming plane waves (blue line), cylindrical waves using Hankel functions(orange line) and scaled plane wave approach (dashed blue line). Figure reproduced from ref. 42

On the other hand, in cylindrical bases we need to extract the phase propagation from Hankel functions, i.e. we are interested in $\frac{d}{dr} \arg H_\nu^{(1,2)}(k_r r)$. However, there is no analytical expression available.

Instead we seek to approximate the problem with modified plane waves, hoping to capture the relevant effects due to cylindrical geometry while still allowing to reach analytical expressions for phase propagation. We start by writing eq. (4.12) in more general form, allowing k_z to vary with propagation. This gives an expression for the acquired phase as

$$\int \text{Re } k_r(r) dr. \quad (4.13)$$

From eq. (4.5) we get the propagation constant where using eq. (4.11) gives

$$k_r^2 = k_0^2 \varepsilon_\theta - k_\theta^2 \frac{r_0^2}{r^2} \frac{\varepsilon_\theta}{\varepsilon_r} \quad (4.14)$$

This equation can now be numerically integrated, allowing us to calculate phase propagation in a cylindrical system (i.e. accounting for magnification). In fig. 4.2 we show that although approximate, this approach gives a practical approximation to actual phase propagation when calculated using Hankel functions.

4.5. Summary

In this chapter we introduced mathematical formulation of diffraction limit in terms of low-pass filtering of plane wave components. We then shortly discussed different approaches on bypassing the limit. Most importantly, we introduced basic idea of the

4. Diffraction limit and subwavelength imaging

hyperlens concept and introduced canalization regime, which is crucial for hyperlens operation.

Finally we covered mathematical details of wave propagation in cylindrical geometry, showing that due to the cylindrical geometry waves are magnified as they propagate through the cylindrical geometry. We also discussed phase propagation in cylindrical geometry, which will become important in chapter [6](#).

Part II.

Results

Here we present the main results achieved during the PhD project. The chapters here are based on two published papers, with one more manuscript in preparation.

5. Dark-field hyperlens

This chapter is mostly based on ref. 34 (J1), with contributions from ref. 56 (C1).

5.1. Introduction

One problem with the approaches for the hyperlens has been lack of intensity contrast, i.e. capacity to image weak scatterers. For practical purposes the objects for superresolution imaging would be biological samples (with sizes ranging from a few hundreds of nanometers), which due to their dielectric properties and small sizes are relatively weakly scattering. But the experiments with hyperlenses so far have used bright (high-contrast) sources, such as slits in an opaque metal film. Both the incident and scattered fields are carried in the usual hyperlens design and thus the image reaching far field has very low contrast, as the scattered fields are weaker than the incident radiation.

To avoid problems with low contrast, my PhD project has been focused on developing the theory of the dark-field hyperlens concept. This idea was proposed by Benisty and Houdail in 2012.[33] However, that work requires two separate hyperlenses: one to convert the incoming plane wave to specially shaped illumination to the scatterer and the second hyperlens to collect scattered light from the sample. The two hyperlenses are designed in such way that the illuminating light itself does not couple into the imaging hyperlens.

We have proposed and studied a design based on a single hyperlens, where we exploit the type-II HMM to filter out incident radiation thus allowing only scattered waves to propagate through the system. Recalling from chapter 3, the type-II HMM can behave in two ways: the high- k waves propagate unimpeded, as is typical for an hyperbolic medium. However, here the low- k waves are evanescent and thus do not propagate through the medium. This behaviour (low- k filtering) can be used to filter out an incoming plane wave (having naturally small transverse wavevector,

5. Dark-field hyperlens

due to originating from the far field) from the scattered fields (where the near fields have significant contribution in high-k components).

In this chapter we present our earlier results (refs. 34 and 56). In these publications we studied a multilayer based implementation of the dark-field hyperlens concept. We first show that type-II HMM is indeed suitable for filtering incident radiation while also capturing scattered high-k waves. Crucially we note that the key building block for a (bright-field) hyperlens — canalization regime — is not available for dark-field designs. In this chapter we will discuss implications of this limitation and explore possibilities for finding a good compromise between imaging contrast and imaging quality.

Although there have been different proposed implementations and experimental realizations of hyperlenses, the most promising ones are based on metal-dielectric multilayers.[16, 18, 31] Therefore in the start of our project we specifically studied implementing a dark-field hyperlens using thin multilayer structures. We limited our studies to designs achievable with realistic material parameters for the visible spectrum. In this constrained approach we still show that a reasonable trade-off between the conflicting requirements can be made. Although the final design is still challenging in terms of fabrication and experiment, it is based on realistically obtainable properties.

We first discuss a planar HMM slab and study scattering via type-II HMM in this flat geometry. This allows first to study filtering and propagation properties of type-II medium without the complications of cylindrical geometry. Later in the chapter we extend the results to a proper cylindrical hyperlens geometry and demonstrate (1) filtering of background fields and (2) subwavelength resolution of the hyperlens design.

5.2. Scattering via type-II HMM slab

5.2.1. Type-II HMM for filtering background fields

To see how type-II HMM leads to high-contrast imaging, we first look at the propagation constant for a HMM (from section 2.4)

$$k_z = \pm \sqrt{\epsilon_o k_0^2 - k_x^2 \epsilon_o / \epsilon_e}, \quad (2.22)$$

from where we see that there is a cross-over point

$$k_c = \sqrt{\varepsilon_e k_0^2}, \quad (5.1)$$

which separates the low-k and high-k behaviour of a type-II HMM. Below k_c the propagation constant k_z is imaginary, indicating evanescent nature of the waves. For these attenuated low-k waves we can write the propagation constant as

$$k_z = \pm i \xi^{-1} \sqrt{\varepsilon_e k_0^2 - k_x^2}, \quad (5.2)$$

where we use canalization ratio $\xi^2 = -\varepsilon_e/\varepsilon_o$ [eq. (3.5)].

As we know for bright-field hyperlens, the crucial part of operation is the canalization regime, which allows the fields to propagate through the hyperlens with little change. However, eq. (5.2) shows that we cannot maximize filtering of low-k waves and strength of canalization at the same time. Increasing canalization ratio by decreasing ε_o or increasing ε_e unavoidably reduces $\text{Im } k_z$ (and thus the evanescent decay of low-waves). Furthermore, increasing ε_e also moves the transition point k_c further, so that more and more waves would fall into attenuated low-k regime, reducing the amount of scattered fields that are able to propagate through the hyperlens.

5.2.2. Scattering via type-I HMM slab

Before looking at a type-II HMM slab, we briefly turn to a characteristic type-I HMM consisting of a dielectric $\varepsilon_d = 3.22$ and a metal $\varepsilon_m = -2.5 + 0.5i$. These parameters are comparable to those used in literature both in experimental and also theoretical discussions of bright-field hyperlenses [18, 29–31]. Effective parameters for this system can be retrieved using eqs. (3.12) and (3.13):

$$\begin{aligned} \varepsilon_o &= 0.36 + 0.24i \\ \varepsilon_e &= -13.3 + 13.4i, \end{aligned}$$

We note that the canalization ratio is $\xi \approx 6$ and thus we can expect a strongly canalizing behavior from such HMM slab (recalling results about canalization in section 3.2.3).

We shall now see how scattered near fields propagate through a type-I HMM slab. So we simulate a small metallic scatterer (details are specified in fig. 5.1) close to a HMM slab. An incoming plane wave illuminates the HMM slab and the

5. Dark-field hyperlens

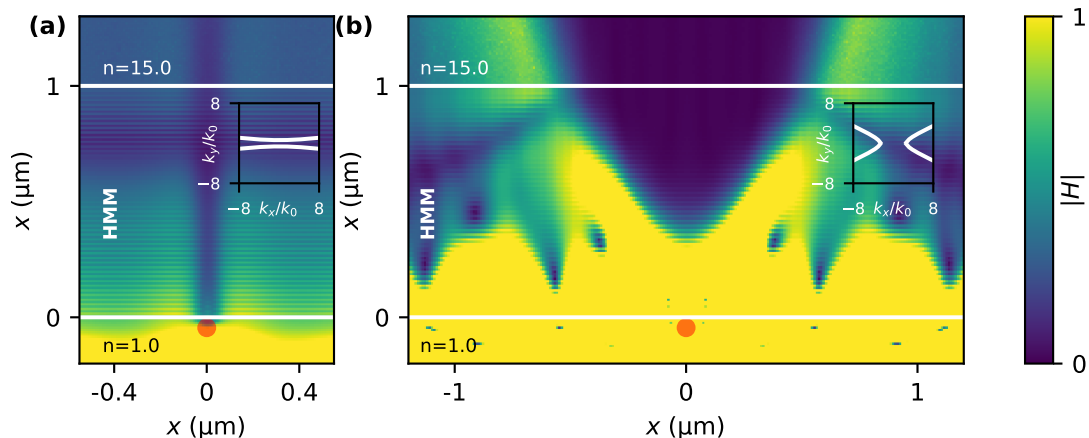


Figure 5.1.: Scattering from a metallic scatterer (diameter 70 nm, $n = 0.01 + 1.5i$) due to incoming plane wave ($\lambda = 715\text{nm}$) through a type-I HMM (a) or a type-II HMM (b). Both structures are multilayer stacks containing 50 periods of 10 nm metal and 10 nm dielectric layers. An artificial high-index medium is placed after the HMM to allow out-coupling of high-k waves from the HMM. Insets show isofrequency contours for the HMMs.

scatterer, with the HMM slab then capturing and propagating the scattered fields. Figure 5.1(a) shows simulation results of such a structure. Given the canalizing nature of the system, we see the expected behavior of scattered fields traveling in a straight narrow beam through the multilayer structure (see also fig. 3.10 and related discussion in section 3.2.3).

However, we can also notice the inherent drawback of type-I based (bright-field) hyperlens: both the incoming plane wave and scattered fields propagate through the system and the incident radiation overwhelms the scattered signal. Because this low contrast of the scattered fields, imaging of these objects is difficult. Here we have considered a metallic scatterer, exhibiting a relatively large scattering cross section. Had we instead used a dielectric scatterer the object would have been mostly invisible in the output.

5.2.3. Scattering via type-II HMM slab

We now show that with a type-II HMM slab we can use the hyperbolic dispersion to filter out incident radiation. We seek to achieve type-II hyperbolic dispersion using a silver-dielectric multilayer structure (recall discussions in section 3.3.2). For simplicity here we assume 50% volume filling fraction for the silver (i.e. the dielectric and metal layer have equal thickness). Here we assume dielectric with $n = 1.45$ and

5.2. Scattering via type-II HMM slab

wavelength of 440 nm, which gives $\varepsilon_m = -5.11 + 0.61i$.^[57] With this we end up with effective parameters¹

$$\varepsilon_o = -1.50 + 0.31i \quad (5.3)$$

$$\varepsilon_e = 7.03 + 0.57i. \quad (5.4)$$

We immediately note the lower canalization ratio $\xi \approx 2.2$ of this design. This means that the waves entering the HMM slab will no longer travel in single narrow beam, but instead two beams will now be formed. This is the key compromise of a dark-field design: we sacrifice canalization ratio to gain in enhanced contrast of output fields. We will motivate this choice of material parameters in the next section, where we will consider type-II HMM in cylindrical geometry.

In fig. 5.1(b) we see the operation of this type-II HMM slab. As discussed, we see the two output beams, due to reduced canalization [e.g. relative to fig. 5.1(a)]. At the same time we see that the illuminating plane wave does not propagate through the slab. With only scattered fields present in the output we avoid issues with visibility of weak scatterers. Here we used a metallic scatterer [as we did in fig. 5.1(a)], but thanks to the dark-field properties of the system we could equally well have used a dielectric scatterer (with much lower scattering cross section).

The fields in fig. 5.1(b) exhibit relatively complex behavior. In order to better understand them, we can turn back to figs. 3.4 and 3.8 and corresponding discussion on wave propagation in hyperbolic media (section 3.2). From that discussion we recall that in a type-II hyperbolic medium we can have three different kind of fields interacting:

1. the incident plane wave, decaying exponentially in the HMM;
2. the two propagating beams excited from high-k scattered waves; and
3. a surface wave propagating along the air-HMM interface.

Existence of these fields complicates the field picture near the input interface. However, during the propagating both the incident plane wave and the surface mode decay, so in the output we are only left with the beam formed by high-k waves.

Here we have used realistic material parameters, which means we are accounting for the losses in the metal. Recalling our earlier discussion on the effect of losses (section 3.2.4) we note that we are using a relatively thin HMM slab (on the order

¹We will explain the choice of material parameters in more detail after we introduce cylindrical geometry and the design constraints arising there.

5. Dark-field hyperlens

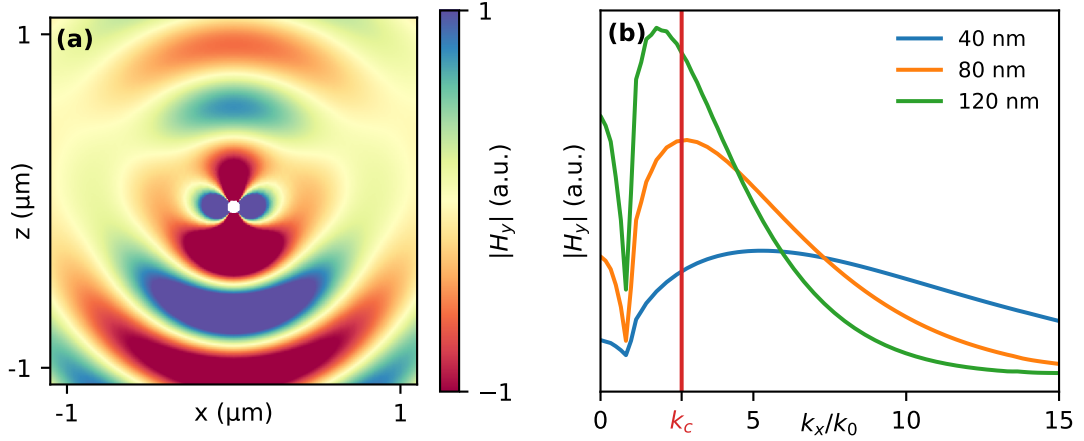


Figure 5.2.: Scattered fields from a perfectly conducting cylinder with diameter 80 nm (a), with k -space compositions of near fields for three different cylinder diameters (b). Low- k cut-off $k_c = 2.65k_0$ for the type-II HMM used in fig. 5.1 is also indicated.

of the wavelength of light). This is necessary to avoid broadening and attenuation of the beams, which would destroy the subwavelength imaging properties of the structure. Here we see that the subwavelength imaging is still feasible, as the two beams themselves are subwavelength in size.

We see that the type-II HMM system performs relatively well. We shall shortly consider why it does perform — or more precisely, in which cases it will not perform. With our choice of material parameters the cut-off point for low- k waves k_c is relatively high, meaning there exists a range of plane wave components that will not propagate through the slab². This means we need to consider the structure of the scattered fields to see when they are able to propagate through the HMM. In particular we see that in case of fig. 5.1(b) it is not detrimental to the imaging process: we have clearly formed fields in the output. We illustrate this in fig. 5.2 by showing k -space spectra for scattered fields as a function of scatterer size. We see that in the case of small particles the scattered fields contain plenty of high- k components. However, as the particle size increases the spectrum is shifted towards low- k regime. Of course, there is some filtering of the plane wave components and we will discuss that in more detail later (section 6.2.3).

²This holds in the strict sense only for very thick HMM slabs. In practice we often assume slabs with thickness in the order of a few free space wavelengths. In such cases the evanescent tails of the low- k waves are not completely attenuated, depending on the dispersion properties of the HMM.

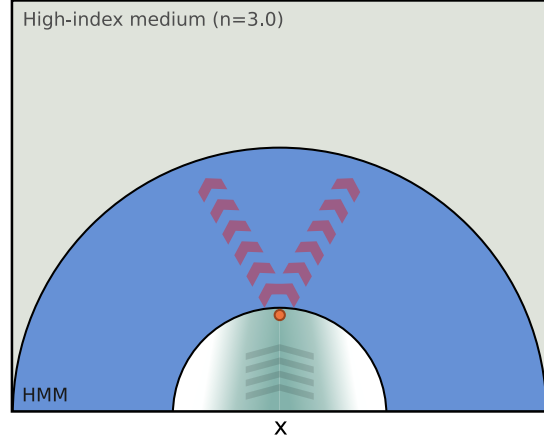


Figure 5.3.: Simulation geometry for the dark-field hyperlens: a scatterer near the inner interface of the hyperlens is illuminated by an incoming Gaussian beam, producing two scattered beams in the hyperlens.

5.3. Cylindrical geometry: dark-field hyperlens

We have now covered the basic ingredients for high-contrast subwavelength imaging (dark-field hyperlens): (1) filtering of incident radiation and (2) propagating scattered fields and reconstructing the fields in the output. Now we will discuss the final component: magnification of a subwavelength image to above the diffraction limit (to be imaged with conventional far-field optics). To achieve that we need cylindrical HMM geometry. Having already covered the principles behind magnification with cylindrical HMMs (section 4.3), we will focus here on complexities brought on by working with type-II HMM in a cylindrical geometry.

The general setup of the system we are considering is shown in fig. 5.3: a small cylindrical scatterer (with a diameter of 70 nm) is placed close to the inner interface of the hyperlens (10 nm from the surface). Again, like we did for the slab geometry, we use a metallic scatterer ($\epsilon = -2.25 + 0.03i$) for a larger scattering cross section. A Gaussian beam is incident upon the cylinder, from which waves will scatter into the hyperlens and propagate to the outer interface. Due to dark-field properties of the type-II HMM, only scattered high-k waves propagate through the HMM, while the incident radiation is reflected back. Note that the low-k cutoff $k_c = 2.65k_0$ of the HMM [given by eqs. (5.3) and (5.4)] is relatively high so the dielectric medium outside must have a high refractive index, to allow waves from the hyperlens to be coupled out.³

³Outcoupling of the waves is limited both by (1) low-k cut-off in the HMM (as waves below cut-off

5. Dark-field hyperlens

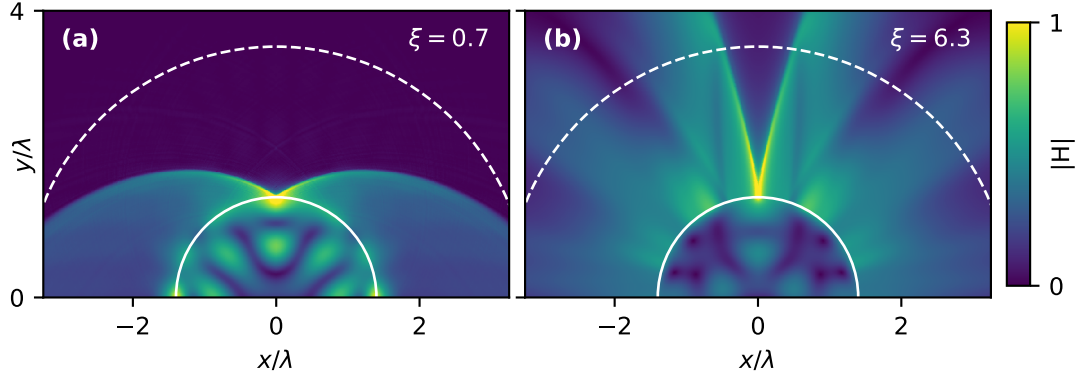


Figure 5.4.: Fields propagating from a point source on the inner interface of a semi-infinite hyperlens, using type-II HMM. Canalization ratio of the HMM is 0.6 (a) or 6.3 (b). Inner radius of the hyperlens is 1.4λ (white solid line). White dashed line indicates a radius of 3.5λ , corresponding to an outer interface of a hyperlens with $2.5\times$ magnification. Here the hyperlens is semi-infinite to avoid reflections from the outer interface.

The primary concern with the type-II hyperlens is (lack of) canalization. As already discussed, in conventional (type-I based) hyperlens the canalization regime ensures that fields propagate through the hyperlens in a narrow beam, facilitating straightforward imaging process. In the previous section we alluded to the fact that for type-II HMM we have to work away from the canalization regime in order to preserve filtering of low- k waves. Instead of trying to work as close to the canalization regime as possible we aim to go further away from the canalization regime. With this we increase separation between the two propagating beams, so that we direct the two beams from the object into two spatially separated regions, avoiding problems with overlapping beams.

In fig. 5.4 we explore the effects of a varying canalization factor in cylindrical geometry. We see that for a very small canalization ratio [fig. 5.4(a)] two beams propagate with a large propagation angle and thus the waves will not escape the hyperlens structure (or at least will not propagate towards the far-field optics). Even for the canalization factor $\xi = 6.3$ used here the waves originating from the point source spread enough to rule out straightforward imaging process. At the same time canalization is already strong enough so that filtering of low- k waves is too weak for proper dark-field operation.

are evanescent within the HMM and (2) refractive index of the outside medium, as waves with $k_x > nk_0$ are evanescent outside the HMM.

5.3. Cylindrical geometry: dark-field hyperlens

Simulations of our proposed design are shown in fig. 5.5(a), where we study scattered fields from a weak dielectric scatterer. The two beams form two image points corresponding to the same source, but due to spatial separation we only need to consider one of the images.

We use the same parameters for the HMM as in previous section [eqs. (5.3) and (5.4)]. As already mentioned, here we (for simplicity) assume equal thickness for dielectric and metal (Ag) layers in the HMM structure. To reach a suitable HMM we have to choose a dielectric medium⁴ and a wavelength (from which follows the permittivity of the Au layer). On one hand we seek to achieve relatively low canalization, so that the two beams are spatially separated and low-k filtering is strong enough to filter out the incident radiation. At the same time the canalization cannot be too low, otherwise the two beams will not reach the far field optics [as shown in fig. 5.4(a)]. Previously we discussed designing multilayer HMM structures (in section 3.3.2). There we showed (fig. 3.15) that the canalization ratio of such structures is generally rather low. So to achieve a good hyperlens operation we reached a design with dielectric $n = 1.45$ and silver at a wavelength of around 440 nm (giving $\varepsilon_m = -5.11 + 0.61i$), giving us the HMM with effective parameters as given earlier by eqs. (5.3) and (5.4).

In order to better understand and visualize the behavior of the design we also performed simulations with a simplified, more idealistic system. Instead of considering the proper multilayer structure, we use an effective medium structure, where we can easily adjust the relevant propagation parameters ($\varepsilon_o, \varepsilon_e$).⁵ We also reduced the losses by a factor of 20, so that the propagating beam of high-k waves would be clearly visible. Furthermore, we used a point source instead of an incoming wave and a scatterer in order to simplify the field structure. Simulation of this “idealized” system is shown in fig. 5.5(b), where the narrow beams of high-k waves propagating through the hyperlens are more clearly visible. We also see that part of the high-k waves reflect from the outer interface: this is total internal reflection due to relatively low refractive index of the outer medium.⁶ In fig. 5.5(c) we show a semi-infinite hyperlens so comparing fig. 5.5(b,c) allows us to further illustrate the

⁴Here we are satisfied by just choosing refractive index and not actually choosing a material.

⁵For a multilayer structure we enter material parameters and the filling fraction to the simulation. These parameters make sense from a fabrication/experiment point of view, but as the behaviour of the hyperlens depends of the effective parameters we are more interested in directly adjusting those.

⁶Of course, the refractive index used here ($n = 3$) low for the optical regime. However, as the HMM structure carries high-k waves, there are plenty of wave components that have too high k to enter the dielectric medium. This is particularly visible in the lossless case, where the high-k waves are not as attenuated.

5. Dark-field hyperlens

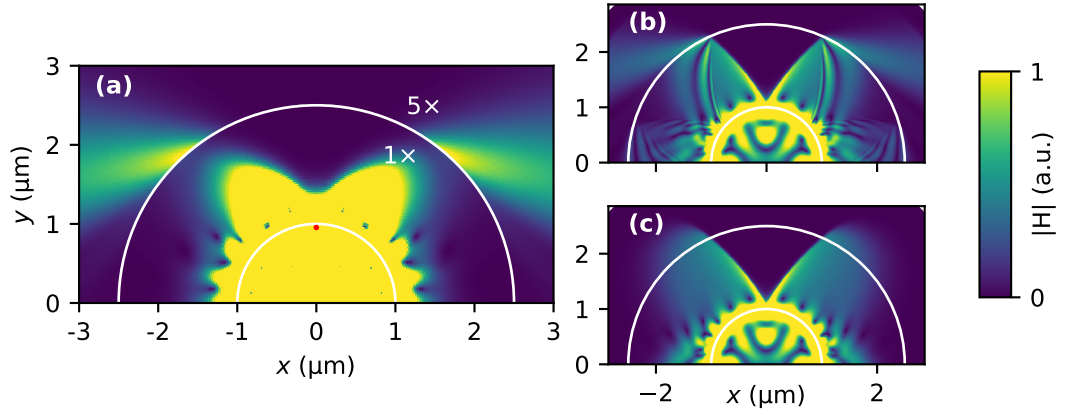


Figure 5.5.: (a) Scattering from a metallic particle, imaged through a dark-field hyperlens. The hyperlens consists of 50 periods of metal-dielectric multilayer (with thickness 10+10 nm). (b,c) Fields due to a single point source placed on a inner interface of a hyperlens, with anisotropic permittivity tensor as per effective medium approximation of the multilayer used for (a). Losses have been decreased by 20 \times to highlight high-k structure of the hyperbolic propagation in the medium. In (b) the total hyperlens thickness is same as in the multilayer structure of (a), whereas in (c) the hyperlens is semi-infinite, avoiding reflection from the outer interface.

effect of the reflected beam in the hyperbolic medium.

Having reached this cylindrical design we now examine subwavelength imaging properties of the hyperlens. We start from a range of simulations with two scatterers with varying distance between them. Figure 5.6(a-c) show a range of simulations of two small scatterers with varying distance between them. As seen from the figure it is possible to distinguish the two particles with a separation below the diffraction limit (~ 360 nm). A more thorough analysis is shown in fig. 5.6(d) where we plot outgoing fields for a range of particle separations (from 100 to 600 nm). We see two peaks (corresponding to the two scatterers), separated by a large distance (due to magnification in the hyperlens). However, as we have already noted, the losses cause significant broadening of the propagating beam. This leads to interference between waves from the two objects (for small separations). In this case the resolution of the device is limited by the broadening, not magnification of the hyperlens.

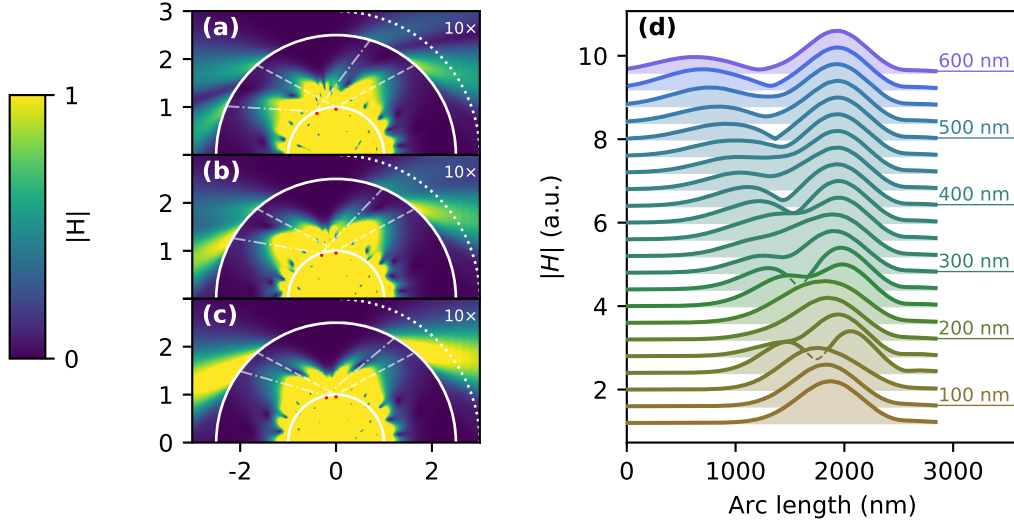


Figure 5.6.: Fields scattered from a pair of scatterers (with same parameters as fig. 5.5) separated by 400 nm (a), 300 nm (b) and 200 nm (c). Fields outside the hyperlens have been scaled $10\times$ so that fields both inside hyperlens and outside the hyperlens are visible, despite attenuation in the hyperlens. The red circles indicate scatterers and the dashed white lines indicate the beams corresponding the scatterers. (d) Output fields of the hyperlens, measured along arc 500 nm away from the outer interface (shown in field plots with dotted line).

5.4. Hybrid design: avoiding low-k cutoff

5.4.1. Challenges due to low-k cutoff

An important practical obstacle for a dark-field hyperlens is the out-coupling: low-k cutoff places a lower limit on the range of waves that can be coupled out. At the same, time refractive index of the outside medium places an upper bound for out-coupling. To achieve a working design we had to use a high-index medium ($n = 3$) outside of the hyperlens, so that the nk_0 of the dielectric was higher than the low-k cutoff ($k_c \approx 2.7k_0$) in the HMM. However, using such a high refractive index is not easy to achieve in practice, so we seek to improve the design to avoid this out-coupling challenge.

Type-II hyperbolic dispersion also limits the magnification available: as the waves propagate through the hyperlens the image is magnified, which in k-space corresponds to scaling down of the transverse wavevector. In case of a canalized type-I based hyperlens this is not an issue as the propagation properties of the waves change very little.⁷ However, in case of a type-II HMM along the magnification

⁷This actually improves canalization, as the waves are moved towards the center of the dispersion

5. Dark-field hyperlens

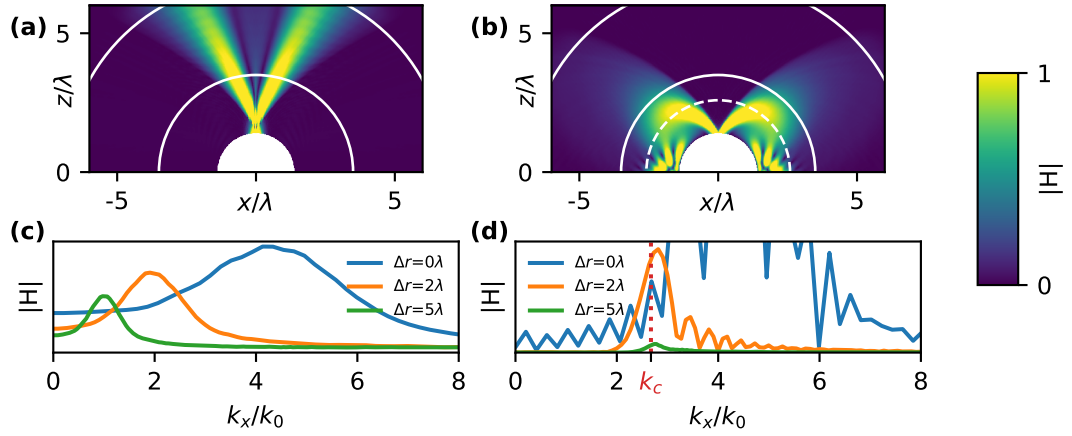


Figure 5.7.: High-k Gaussian beam (see text for details) propagating through a type-I (a) and type-II (b) hyperlens. k-space spectra of the initial fields and fields after propagating to $r - r_0 \approx 2\lambda$ and $r - r_0 \approx 5\lambda$ are shown in (c,d). Type-II HMM is based on the previous section, but losses are reduced $30\times$ to highlight high-k behavior. Type-I is obtained by flipping signs of permittivity tensor components. In (d) low-k cutoff k_c is also shown, with red dotted line.

waves slowly transform from propagating high-k regime to non-propagating low-k regime, thus placing an upper limit on magnification. To further study this issue we compare propagation of scattered fields in bright- and dark-field hyperlens. We excite a beam of waves containing a limited k-space spectrum of waves (centered around $5k_0$), so we can see the transformation of waves in the k-space. First, in fig. 5.7(a) we see that in type-I cylindrical hyperlens the propagating waves are expanded according to the cylindrical geometry. In fig. 5.7(c) we show k-space compositions of propagating waves after different propagation distances. As the waves propagate and are magnified, the k-space spectrum is correspondingly compressed. For a type-I HMM this is not an issue, as low-k components themselves are also allowed to propagate in the medium, so not much changes in terms of propagation. Even though we reduced the losses in the system, we still see some attenuation of the waves. In a type-I HMM this is purely due to the material losses.

In contrast we see that in type-II medium the waves start to be reflected back after propagating for distance $1.4r_0$ [fig. 5.7(b), dashed line indicates $1.4r_0$]. The reflection is due to waves transitioning into the low-k regime, where these components are not able to propagate further and are thus reflected. However, some of the components of the propagating beam are still above the low-k cut-off so these

relation, so the magnification actually helps to reduce phase mismatch between different plane wave components.

5.4. Hybrid design: avoiding low-k cutoff

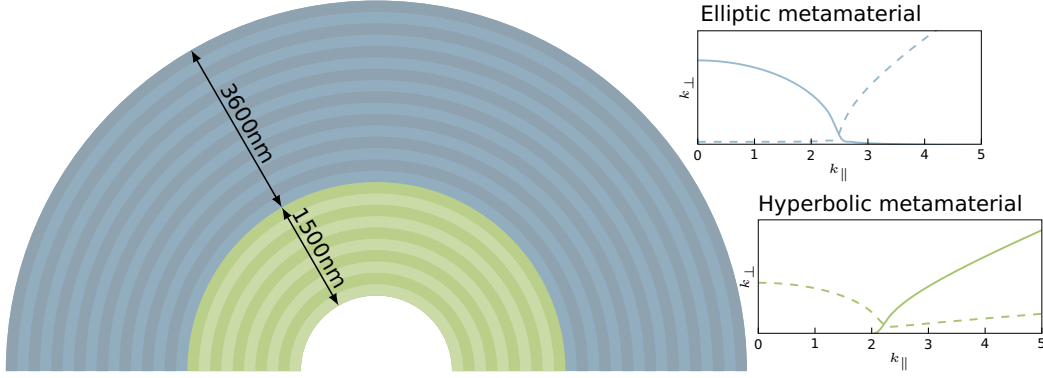


Figure 5.8.: Hybrid design comprising of inner type-II HMM core (shown in green) and a outer region with elliptic dispersion (blue). Insets show dispersion relations of the two media. Reproduced from ref. 56.

components propagate further (where they also will be reflected at some point). This behavior is explored by looking again at the evolution of the k-space spectrum [fig. 5.7(d)]. At first all components of the propagating waves are above cut-off, so propagation behaves similarly to the type-I case. However, as the propagation (and magnification) continues, more and more of the k-space spectrum enters into cut-off and is reflected. This dramatic cut-off at $k_c \approx 2.7k_0$ is clearly visible in the k-space plots of larger propagation distances in fig. 5.7(d). Strong attenuation seen in the k-space plots here is mainly due to evanescent decay of low-k waves, with material losses playing a minor role.

5.4.2. Hybrid design for avoiding low-k cutoff

We proposed [56] a hybrid design combining regions with hyperbolic and elliptic dispersions (fig. 5.8). This way the inner HMM core of the hybrid structure provides dark-field superresolution imaging: capturing (and magnifying) the scattered high-k waves and filtering the incident low-k illumination. The outer structure is designed to have elliptic dispersion, where the waves will propagate (and magnify) further. We can expect magnification properties in the second layer as well, as the elliptic dispersion is flat enough for waves with small k , so that the similar arguments hold as with hyperbolic medium.

For the type-II HMM we use the same material parameters as before, but we have slightly tuned layer thicknesses: thickness of the metal layer is 12 nm, while the dielectric layers are 18 nm thick (giving metal volume filling fraction 40%). As we still have 50 periods, this increases thickness of the HMM part to 1500 nm, compared

5. Dark-field hyperlens

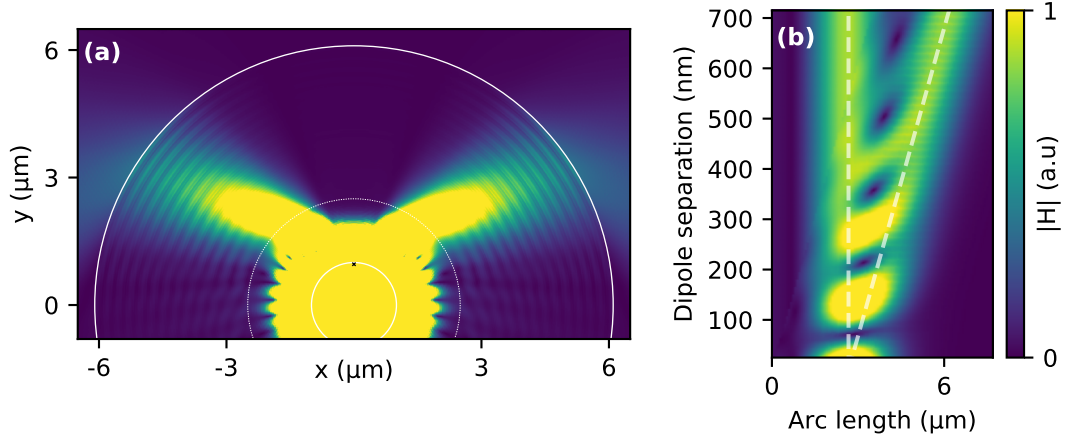


Figure 5.9.: (a) Fields from a point source on the inner interface of the hyperlens. The dashed line indicates change from hyperbolic to elliptic dispersion. (b) Fields along outer interface of the hyperlens as function of point source separation.

to the previous design. With this we reduce low- k cut-off from $k_c = 2.65k_0$ to $2.20k_0$, allowing more of scattered fields to propagate in the hyperlens.

Ideally the second layer would be a type-I HMM, allowing propagation of all waves. However, for the metal we are using this is difficult to achieve, as it would require dielectric layers with refractive index over 2.6.⁸ Instead, we aim for the second layer to have elliptic dispersion, which allows the magnified waves to propagate, but reflecting rest of the high- k waves. Assuming that the HMM layer has magnified the image enough, this will not be an issue. Compared to the dielectric in the HMM part we use a high index dielectric ($n_{d2} = 2.0$) and a significantly reduced filling metal fraction (20%), achieved by changing the thickness of dielectric layers to 48 nm (while keeping the metal layers at 12 nm). The second part of the hybrid hyperlens consists of total 60 periods, giving a total thickness of 3600 nm.

5.4.3. Results

In fig. 5.9(a) we show the operation of this hybrid design. From the figure we see a similar results as we showed before [fig. 5.5], however here we have avoided the need for very high-index outer medium, making the experimental design more feasible. To study superresolution properties of this design we calculated output fields from two point sources with varying separation, shown in fig. 5.9(b). As expected, the behavior of the hyperlens is similar to the previously shown design

⁸This follows from eq. (3.12), where we can solve for $\varepsilon_o = 0$ as function of ε_d , with $f = 0.5$.

(fig. 5.5): from 300 nm and above we can (more-or-less) reliably distinguish the two sources, whereas below 200nm the sources appear as one (due to the broadening).

We emphasize that the main improvement of this hybrid design is more reasonable requirements for the outside medium: in this case we assumed a dielectric medium with $n = 2$, which is a more realistic choice than $n = 3$ required for a design based on a pure type-II HMM structure. Another improvement of this design is reduced losses: as insets in fig. 5.8 shows, the imaginary part of k_z is reduced in the elliptic layer, leading to smaller attenuation of propagating waves.

5.5. Summary

In this chapter we proposed a dark-field hyperlens design based on a type-II HMM structure. First we showed how low-k cut-off of a type-II HMM can be used to filter incident radiation, while still capturing fields scattered from a subwavelength object.

We discussed design considerations of cylindrical dark-field hyperlens, with the important point of lack of canalization regime for type-II HMM based design.

Having covered the basic design considerations we showed simulations of our initial design[34], based on realistic metal-dielectric multilayer design. We showed that despite the strong losses in metal layers, the subwavelength imaging process still works, although with reduced performance when compared to an “ideal” system with very low losses.

Finally, we raised the issue of magnification and corresponding compression of k-space spectrum. To combat the resulting challenges with out-coupling we discussed our proposition for improved hybrid hyperlens design [56].

Acoustic dark-field hyperlens

We have by now covered the necessary theory of hyperlenses, so we can now briefly discuss the acoustic version of the design. Previously, in section 3.5, we outlined the theory of acoustic HMMs and showed that it mirrors the optical case. We use a resonant acoustic HMM, which we already introduced in section 3.5. By changing the operation frequency of the structures we can move from type-I to type-II HMM, realizing acoustic dark-field hyperlens.

Figure 5.10(a) shows calculated dynamic mass density, following the procedure of ref. 53. In fig. 5.10(b) we reproduce results from Chiang et al. [38], showing bright-field operation of the acoustic hyperlens operating at 6065 Hz. By changing

5. Dark-field hyperlens

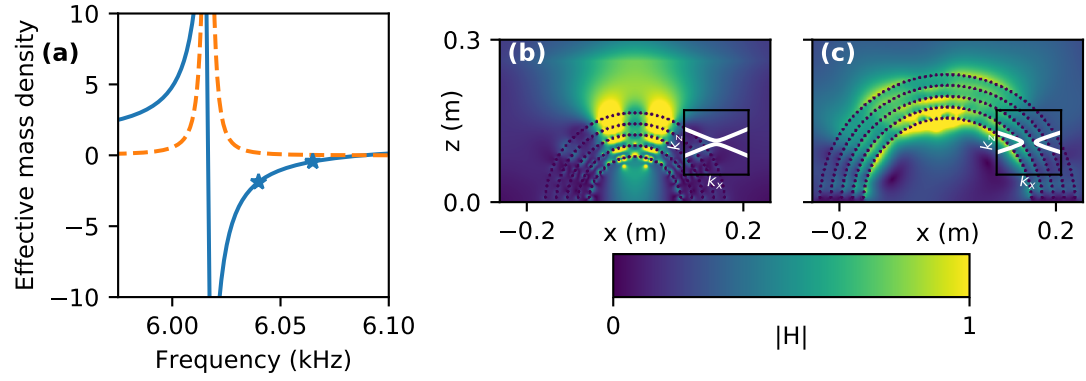


Figure 5.10.: (a) Calculated effective mass density of the cylindrical resonators, markers indicate frequencies for bright- and dark-field hyperlens. (b,c) Hyperlens structure consisting of such resonators, operating as a bright-field hyperlens at 6065 Hz (b) and as a dark-field hyperlens at 6040 Hz (c). Insets show hyperbolic dispersions of effective medium approximation.

the operating frequency to 6040 Hz the same structure now behaves as dark-field hyperlens [fig. 5.10(c)], where we can see a lack of canalization (two output points appearing from a single source) and a surface mode appearing on the inner interface (as we also observed in our optical dark-field hyperlens).

6. Magnetic dark-field hyperlens

This chapter is based on
ref. 42 (J2).

6.1. Motivation: “pseudocanalization” via phase compensation

We now move away from practical multilayer designs of the previous chapter. We recall that in section 3.4 we pointed out that with negative permeability we can reach a kind of “complementary” medium — where the dispersion relation is identical compared to the μ -positive case, but the sign of the propagation constant k_z is flipped. As the propagation constant describes phase accumulation during propagation this “complementary” medium exhibits reversed phase propagation, when compared to respective nonmagnetic HMM. This leads to a question of what happens if we combine a “normal” and a “complementary” HMMs in a way that phase propagation is canceled in the output.

Implications of canceling the phase propagation become clearer when looked from the perspective of the canalization regime (section 4.3.2), where we by suitably choosing the permittivity tensor components (i.e. maximizing the canalization ratio ξ) the propagation constant k_z is suppressed and thus the waves propagate without acquiring any phase. However, as a downside we have less degrees of freedom to engineer hyperbolic dispersion, as we need to impose a large canalization ratio ξ for the canalization regime. In contrast, the idea of neutralizing the phase propagation using μ -negative media enables us to achieve a similar effect as canalization regime, without constraints on the HMM parameters. This leaves us are free to choose parameters for the first HMM region, as long as we choose suitable parameters for the second region, reaching a “complementary” dispersion.

This idea of phase compensation is illustrated in fig. 6.1. In fig. 6.1(a) we show a HMM operating in canalization regime: the initial fields propagate with very little change.¹ The idea presented in this chapter is to use two complementary media, as

¹Canalization ratios that are usually achieved are not too high, so there is some phase acquired

6. Magnetic dark-field hyperlens

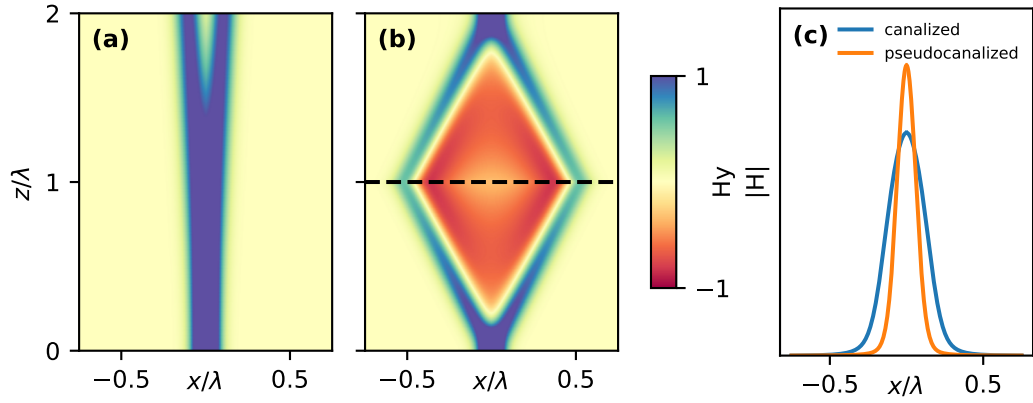


Figure 6.1.: A narrow Gaussian beam propagating through a canalizing (a) and pseudo-canalizing (b) system. Fields after the propagations are shown in (c). Canalization is achieved by reducing phase propagation term (with canalization ratio $\xi = 20$) whereas pseudocanalization relies on combination of two complementary media, so that in the end phase propagation is cancelled.

shown in fig. 6.1(b): although in the two layers of the system phase propagation is not suppressed, the phase propagation is reversed in the second medium, after propagating through both layers initial fields are reconstructed. Final fields are compared in fig. 6.1(c), showing that in the output the original narrow Gaussian shape is mostly preseved.²

In this chapter we explore achieving canalization using reversal of phase propagation (“pseudocanalization”). This is in general achieved using μ -negative HMMs, but we also shortly discuss limited pseudocanalization achievable using nonmagnetic HMMs. We start from planar slab geometry and cover important consideration in case of type-I and type-II HMMs. After we extend the discussion to cylindrical geometry and show how this pseudocanalization offers an improved design for dark-field hyperlens.

throughout propagation. This accounts for small broadening and phase advancement seen in the figure.

²Given a canalization ratio $\xi = 20$ the Gaussian beam is slightly broadened in the canalizing system.

6.2. Phase compensation in planar structures

6.2.1. Introduction

For the first layer we assume a simple hyperbolic medium with

$$\varepsilon_o^{(1)} = \mp 1 + \gamma i, \quad (6.1)$$

$$\varepsilon_e^{(1)} = \pm 1 + \gamma i, \quad (6.2)$$

$$\mu^{(1)} = 1, \quad (6.3)$$

where depending on the signs we have either type-I ($\varepsilon_e < 0 < \varepsilon_o$) or type-II hyperbolic medium ($\varepsilon_o < 0 < \varepsilon_e$). We allow for a lossy medium, represented by loss term γ .

For analysis we adopt a relatively simple approach: we prescribe the fields at $z = 0$ and look into propagation in the positive z direction. As per eq. (2.14) (see section 2.4 on wave propagation), the plane wave components of the fields after distance d in a homogeneous medium are given by

$$\mathbf{E}(k_x, d) = \mathbf{E}(k_x, 0) \exp[ik_z(k_x) d]. \quad (6.4)$$

The effect of the propagation constant k_z can be split into real (k'_z) and imaginary (k''_z) parts: the real part results in a phase factor $\exp(ik'_z d)$ for the propagated field, while the imaginary part gives an attenuation factor $\exp(-k''_z d)$.

The pseudocanalizing system consists of two layers, with thicknesses d_1 and d_2 and optical parameters $\varepsilon_o^{(1)}, \varepsilon_e^{(1)}, \mu^{(1)}$ and $\varepsilon_o^{(2)}, \varepsilon_e^{(2)}, \mu^{(2)}$. For a rigorous analysis we would need to consider reflections from the interfaces at $z = d_1$ and $z = d_1 + d_2$ and also reflections due to imposed fields at $z = 0$. However, in the basic analysis we neglect these effects. For the interface between the two HMMs we have perfect impedance matching in the lossless case.³ As any practical applications are limited to the low-loss regime, we will assume impedance matching also for lossy calculations. Neglecting reflections from $z = d_1 + d_2$ is arguably not physically correct, but nevertheless we assume this for simplicity.⁴ With these assumptions there is subse-

³It is easy to see that impedances for oblique incidence $\gamma = k_z/\varepsilon_x k_0$ are always matched in the lossless case.

⁴In effect, we are assuming that the second layer is semi-infinite, or at very least the medium after the second layer is impedance matched. In practice we are interested in systems where the pseudocanalizing system is in a conventional dielectric (e.g. air). In such case there is strong impedance mismatching for high-k waves, as these wave will be totally internally reflected. However, introducing these reflections would only complicate the theory and would not give any extra insight into the physics of pseudocanalization.

6. Magnetic dark-field hyperlens

quently no need to consider reflections from the $z = 0$ boundary either. Later we validate these assumptions with full-wave simulations.

Given these simplifications we can straightforwardly apply the propagation equation [eq. (6.4)] to get an expression for propagated fields (in k-space)

$$\mathbf{E}(k_x, z) = \begin{cases} \mathbf{E}(k_x, 0) \exp\left(ik_z^{(1)}z\right) & z \leq d_1, \\ \mathbf{E}(k_x, 0) \exp\left(ik_z^{(1)}d_1\right) \exp\left[ik_z^{(2)}(z - d_1)\right] & z > d_1, \end{cases} \quad (6.5)$$

where $k_z^{(1)}$ and $k_z^{(2)}$ are propagation constants for the first and second layer, given by eq. (2.22) using respective permittivities and permeabilities. This equation allows us to easily calculate propagation of (plane wave components of) fields through our two-layer system. For real-space fields we need to Fourier transform the resulting fields $\mathbf{E}(k_x, x)$.

Looking at fields after propagation through our two-part system, we get from eq. (6.5) and (looking at fields at $z = d_1 + d_2$) the expression for propagated fields

$$\mathbf{E}(k_x, d_1 + d_2) = \mathbf{E}(k_x, 0) \exp\left[i\left(d_1 k_z^{(1)} + d_2 k_z^{(2)}\right)\right]. \quad (6.6)$$

Pseudocanalizing behavior is reached when we reduce the exponential term to unity (thus reproducing the initial fields), which gives the condition for pseudocanalization

$$d_1 k_z^{(1)} + d_2 k_z^{(2)} = 0. \quad (6.7)$$

To reach conditions for material parameters between two slabs we assume for now that both media are lossless and furthermore that the relative permeability of the first medium is unity ($\mu^{(1)} = 1$). For the second layer we assume negative permeability, so $\mu^{(2)} < 0$. We shall look at the two limiting cases: $k_x = 0$ and $k_x = \infty$. Writing out eq. (6.7) for these two cases we get two equations

$$d_1 \operatorname{sgn}\left(\varepsilon_y^{(1)}\right) \sqrt{\varepsilon_x^{(1)}} = -d_2 \operatorname{sgn}\left(\varepsilon_y^{(2)}\right) \sqrt{\mu^{(2)} \varepsilon_x^{(2)}}, \quad (6.8)$$

$$d_1 \sqrt{-\varepsilon_x^{(1)} \varepsilon_y^{(1)}} k_x / \varepsilon_y^{(1)} = -d_2 \sqrt{-\varepsilon_x^{(2)} \varepsilon_y^{(2)}} k_x / \varepsilon_y^{(2)}. \quad (6.9)$$

Solving these two equations gives the conditions for the material properties of the two slabs:

6.2. Phase compensation in planar structures

$$\mu^{(2)}\varepsilon_x^{(2)} = \varepsilon_x^{(1)}d_1^2/d_2^2, \quad (6.10)$$

$$\mu^{(2)}\varepsilon_y^{(2)} = \varepsilon_y^{(1)}. \quad (6.11)$$

Although we derived these relations based on two limiting cases, it is easy to verify that the condition in eq. (6.7) is fulfilled for all k_x .

In case of lossy media the phase compensation can still be achieved. In this case we would enforce real parts of eq. (6.7).⁵ In principle we do not need to place any constraints on the losses, at least from the phase compensation viewpoint.⁶ However, here we assume $d_1 \text{Im } k_y^{(1)} = d_2 \text{Im } k_y^{(2)}$ as this allows us to reach the following analytical conditions for complex permittivities:

$$\mu^{(2)}\varepsilon_x^{(2)} = \varepsilon_x^{(1)*}d_1^2/d_2^2, \quad (6.12)$$

$$\mu^{(2)}\varepsilon_y^{(2)} = \varepsilon_y^{(1)*}. \quad (6.13)$$

6.2.2. Phase compensation with type-I HMM

We shall now demonstrate the results obtained in the previous section by showing phase compensation in the case of type-I HMM. We assume the first medium given is by eqs. (6.1) to (6.3) (with signs such that $\varepsilon_e < 0 < \varepsilon_o$, i.e. type-I HMM) and then get the parameters for the complementary medium from eqs. (6.12) to (6.13) as:

$$\begin{aligned} \varepsilon_o^{(2)} &= 1 + \gamma i, \\ \varepsilon_e^{(2)} &= -1 + \gamma i, \\ \mu^{(2)} &= -1. \end{aligned}$$

Note that we have assumed equal thickness of the first and second layers ($d_1 = d_2$).

We assume fields with Gaussian profile $\exp(-x^2/\Delta^2)$ on the interface $z = 0$,

⁵Here we recall an earlier discussion on the effects of real (k'_z) and imaginary (k''_z) part of propagation constant k_z . For lossless type-I media we neglected k''_z term and only focused on effects of the real part (the phase term) of the propagation constant. However, in the case of a non-negligible attenuation term parts of propagating waves are attenuated and thus perfect reconstruction is not possible. There is no way to restore those attenuation components without gain (i.e. $k''_z > 0$) and we thus focus our attention on the real part of the k_z .

⁶Of course, in practice attenuation of plane wave components is an important consideration in reconstructing the initial fields.

6. Magnetic dark-field hyperlens

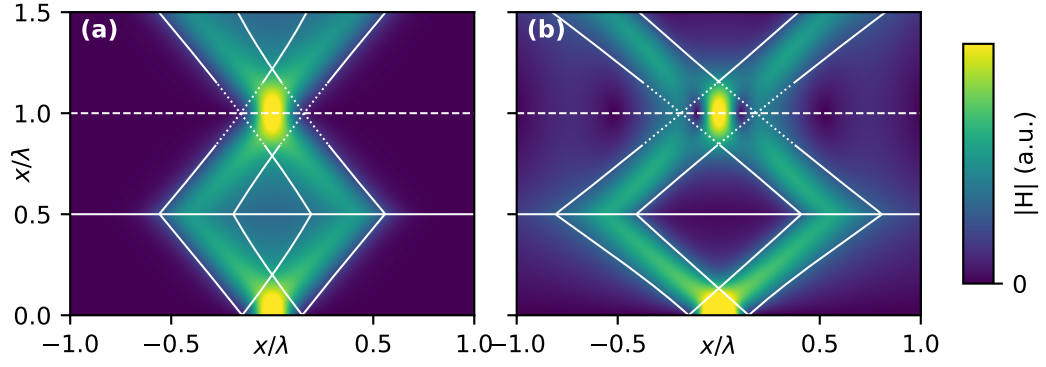


Figure 6.2.: Pseudocanalizing operation based on a type-I HMM (a) and type-II HMM (b). At $z = 0$ a Gaussian profile $H_z = \exp(-x^2/\Delta^2)$ of fields is imposed, with $\Delta = 0.1\lambda$. Losses are taken to be $\gamma = 0.01$.

which after Fourier transform yields expression in k-space

$$H_z(k_x, z=0) = \sqrt{\pi}\Delta \exp\left(-\frac{1}{4}\Delta^2 k_x^2\right). \quad (6.14)$$

Now, using eq. (6.5) we can study wave propagation through the two-layer system. Results of the calculation are shown in fig. 6.2(a), where we see that after fields propagate through both layers the initial fields are restored. In the calculation we have assumed second layer to be semi-infinite.

6.2.3. Phase compensation for type-II HMM

The same procedure can be applied to type-II HMM as well. Using eqs. (6.12) and (6.13) we get parameters for the second layer (this time having type-II HMM as the first layer, i.e. $\varepsilon_o^{(1)} < 0 < \varepsilon_e^{(1)}$):

$$\begin{aligned} \varepsilon_o^{(2)} &= -1 + \gamma i \\ \varepsilon_e^{(2)} &= 1 + \gamma i \\ \mu &= -1. \end{aligned}$$

In fig. 6.2(b) we show propagation through this type-II HMM based pseudocanalizing system. Comparing results against type-I system [fig. 6.2(a)] we see a very

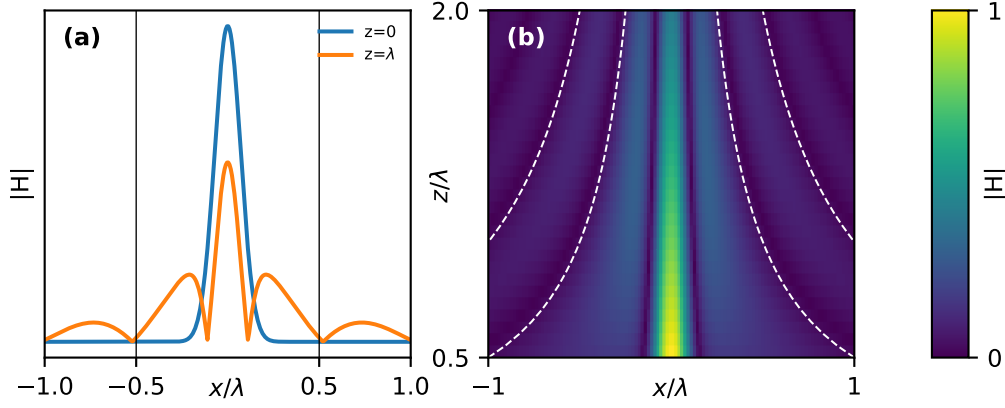


Figure 6.3.: (a) Initial fields (blue) and fields after propagation through pseudocanalizing (orange) type-II HMM system [fig. 6.2(b)]. (b) Fields after propagation through the pseudocanalizing system, with various low-k cutoffs k_c . White dashed lines indicate zeros of $\sin(k_c x)/x$.

similar picture: in the second layer phase propagation is reversed and using that the initial fields are reconstructed at $z = d_1 + d_2$. However, we see that the reconstruction is not perfect as there is interference between the two beams. This is due to low-k filtering, as we shall now explain.

Low-k filtering We show effect of low-k filtering in detail in fig. 6.3(a), where we plot electric field slices from fig. 6.2(b) for $z = 0$ and $z = d_1 + d_2$. We see that in effect the point source is more narrow, but due to filtering of low-k waves sidelobes have now appeared.

There is an important difference between pseudocanalization in type-I and type-II HMMs: while in type-I HMM we could assume that only real part k'_z of the propagation constant k_z has a significant contribution, this is not case for type-II HMM. Wave components below the low-k cutoff k_c are not allowed to propagate in a type-II HMM, and thus the propagation constant k_z is now dominated by the imaginary component k''_z for low-k waves, resulting in attenuation of these components. This means that the propagated fields [given by eq. (6.6)] can not perfectly reconstruct the original fields at $z = 0$, as the low-k components are now missing.

Imaginary part of the propagation constant (k''_z) ends up in eq. (6.6) as an attenuation term $[\exp(-k''_z z)]$, which we can consider as a high-pass filter with cutoff at k_c . Looking then waves from a point source propagating through a pseudocanalizing

6. Magnetic dark-field hyperlens

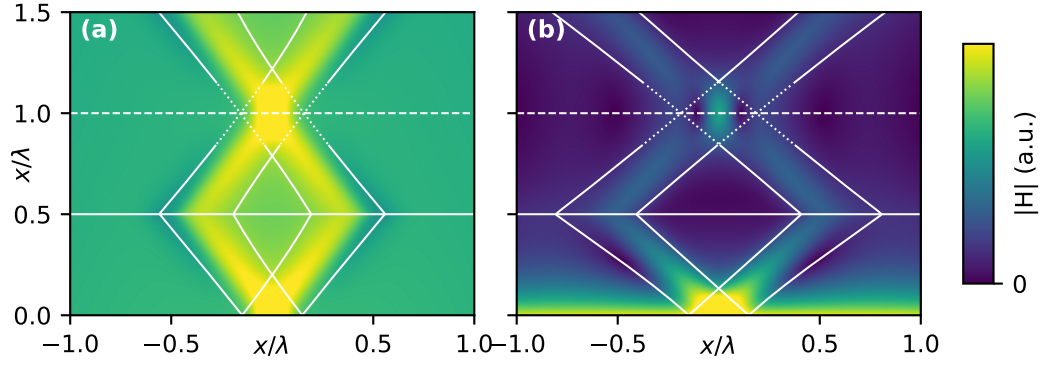


Figure 6.4.: Propagation of incident plane wave and “scattered” fields through a pseudocanalizing system based on a type-I HMM (a) and type-II HMM (b). Parameters for calculation match fig. 6.2, except additional term for normally incident plane wave.

system we reach the following approximation for the propagated fields:

$$\mathbf{E}(x, y) \approx \mathbf{E}_0 \frac{2}{x} \sin(k_c x), \quad (6.15)$$

where we used the Fourier transform of a rectangular function to approximate the propagated image. In fig. 6.3(b) we show fields propagating through a pseudocanalizing system with varying k_c . We see that due to the high-pass filtering the image now has additional zeros at $n\pi/k_c$, with $n = \pm 1, \pm 2, \dots$. In case of low k_c the additional zeros have relatively minor effect on reconstructed fields, but as k_c gets higher the zeros appear closer and thus the sidelobes become more pronounced.

We will return to the issue of the sidelobes with cylindrical geometry, when we will be discussing the resolution of a pseudocanalizing dark-field hyperlens.

Dark-field operation An important upside of pseudocanalization is that we can combine this with the dark-field properties of type-II HMM. As we discussed earlier (section 5.3) the canalization ratio and filtering of low-k waves are inversely related, so increasing canalization makes dark-field operation impossible. As pseudocanalization is independent of dispersion properties we can achieve perfect reconstruction of fields with dark-field operation.

To show that we consider a case similar to a weak scatterer under plane wave

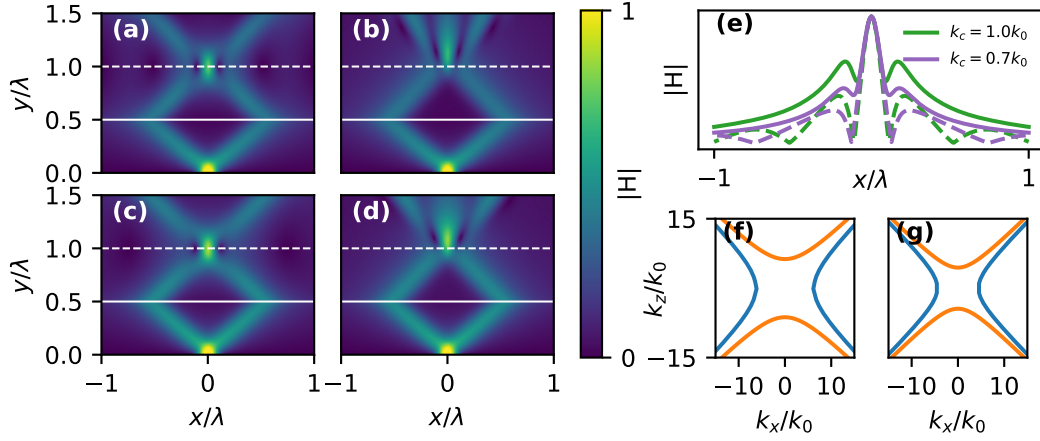


Figure 6.5.: Phase compensation using magnetic (a,c) and non-magnetic pseudocanalization (b,d). Fields at $z = \lambda$ (e) show compensated fields, with dashed lines indicating magnetic and solid line nonmagnetic pseudocanalization. (f,g) show corresponding isofrequency contours for the two layers of non-magnetic system for $k_c = k_0$ (f) and $k_c = 0.7k_0$ (g).

illumination:

$$H_z(k_x, z=0) = \overbrace{H_s \sqrt{\pi} \Delta \exp\left(-\frac{1}{4} \Delta^2 k_x^2\right)}^{\text{"scattered"}} + \overbrace{H_i \delta(k_x)}^{\text{"incident"}}, \quad (6.16)$$

where we now have a narrow Gaussian beam (playing the part of scattered fields) and a normally incident plane wave. As before, we use eq. (6.5) to calculate propagated fields.

We show results for both type-I and type-II system in fig. 6.4, from where we now see an important difference between the two systems. Type-I system [fig. 6.4(a)] carries both scattered and incident fields, whereas fig. 6.4(b) shows that the type-II HMM filters out the incident plane wave. For both cases (and as in fig. 6.2) the phase propagation is cancelled and thus initial fields are restored (apart from the effects of low-k filtering).

6.2.4. Phase compensation without magnetic properties

It is possible to achieve (limited) phase compensation even with non-magnetic HMMs (i.e. $\mu = 1$). To show this we start again from eqs. (6.8) and (6.9)

6. Magnetic dark-field hyperlens

$$d_1 \text{sgn}(\varepsilon_y^{(1)}) \sqrt{\varepsilon_x^{(1)}} = -d_2 \text{sgn}(\varepsilon_y^{(2)}) \sqrt{\mu^{(2)} \varepsilon_x^{(2)}}, \quad (6.8)$$

$$d_1 \sqrt{-\varepsilon_x^{(1)} \varepsilon_y^{(1)}} k_x / \varepsilon_y^{(1)} = -d_2 \sqrt{-\varepsilon_x^{(2)} \varepsilon_y^{(2)}} k_x / \varepsilon_y^{(2)}. \quad (6.9)$$

We notice that eq. (6.9) (corresponding to limit of $k_x = \infty$) does not contain magnetic permeability μ . This implies that in large k_x limit we can achieve phase compensation [eq. (6.7)] without the need for magnetic properties. Of course, this phase compensation is limited to high-k regime, as for waves near the cut-off k_c the phase propagation is not canceled.

Solving eq. (6.9) (i.e. looking at high-k limit) yields conditions for limited (non-magnetic) pseudocanalization:

$$\text{sgn}(\varepsilon_y^{(1)}) = -\text{sgn}(\varepsilon_y^{(2)}), \quad (6.17)$$

$$\varepsilon_x^{(1)} / \varepsilon_y^{(2)} = (\varepsilon_x^{(2)} d_1^2) / (\varepsilon_y^{(2)} d_2^2). \quad (6.18)$$

The equations show that this limited pseudocanalization is achieved by combining type-I and type-II HMM. This means that this approach is affected by low-k filtering and subsequent limitations to reconstructing the initial fields. Of course, lack of phase compensation for waves near k_c makes things worse.

To see how well this limited pseudocanalization works we study again the propagation of a narrow Gaussian beam (as in fig. 6.2). Comparing magnetic [fig. 6.5(a)] and nonmagnetic pseudocanalization [fig. 6.5(b)] schemes we observe partial reconstruction of initial fields in the nonmagnetic system as well. Looking more carefully at the reconstructed fields [fig. 6.5(e); solid lines] we see that with non-magnetic phase compensation the sidelobes are more pronounced and thus this approach is not very promising for hyperlens applications.

As nonmagnetic phase canalization only works with high-k waves we can expect improvement as we decrease the low-k cutoff k_c . We show that in fig. 6.5(c-d) and in more detail by dashed lines in fig. 6.5(e), where a reduction in sidelobes is observed. As we discussed in the previous section, lowering k_c also improves magnetic phase compensation (due to a reduction of sidelobes originating from low-k filtering).

Looking at dispersion relations for nonmagnetic pseudocanalization in fig. 6.5(f,g) illuminates the issue of non-perfect phase compensation. As expected, for large k_x the dispersions overlap (albeit being of opposite sign, as required for phase compen-

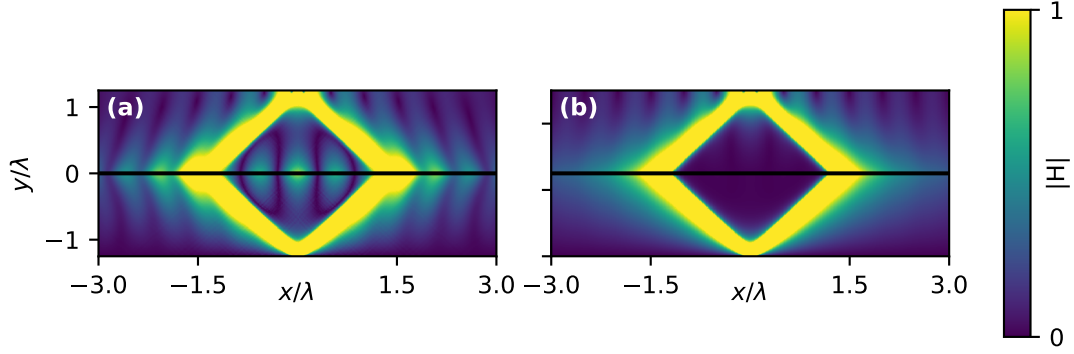


Figure 6.6.: Comparison of full wave simulation (a) and approximate solution via eq. (6.5) (b). In both cases Gaussian input beam is prescribed at $z = -1.25\lambda$, given by $H_z = \exp \left[-x^2 / (\lambda/15)^2 \right]$.

sation). However, in low- k regime (and near k_c) there is significant divergence in the dispersion, as expected. Comparing cases for $k_c = k_0$ [fig. 6.5(f)] and $k_c = 0.7k_0$ [fig. 6.5(g)] it is evident that overlap between the two dispersions is improved.

6.2.5. Verifying semi-numerical approach

We can verify the semi-numerical approach [eq. (6.5)] using full-wave simulations. In fig. 6.6 we compare results from the simulations along with the semi-numerical approach.⁷ Looking at fields at the output ($z = 1.25\lambda$) we note a good correspondence between the two approaches, with visible interference pattern due to low- k filtering (as discussed above). However, the full-wave simulations reveal that the interface between the two media supports a surface mode [see fig. 6.6(a)], that is neglected in our semi-analytical approach. However we note that from the perspective of pseudocanalization this surface mode does not play an important role.

It should be noted that the surface mode can only appear for a type-II HMM based system. The surface mode has to have imaginary k_z in both media, so that it is evanescently tied to the interface. The low- k filtering means that in type-II hyperbolic media waves below the cutoff k_c are evanescent and thus can support surface modes (as we briefly covered in section 3.2.2).

⁷In order to have comparable results we prescribe input fields at $z = -1.25\lambda$ for both approaches. A more physically correct approach would be to use a point source for the FEM simulation, but this would make comparing the two solutions more difficult. As discussed above, enforcing the fields at the boundary can introduce additional reflections to the system, but here this turns out not to be important.

6. Magnetic dark-field hyperlens

6.2.6. Summary

We outlined the idea of using two complementary slabs to cancel out the phase propagation. We showed that this can be used to perfectly reconstruct initial fields (in case of type-I HMM). In the case of type-II HMM reconstruction of fields is limited by the attenuation of low-k waves. Crucially, we outlined the conditions [eqs. (6.12) and (6.13)] necessary for the second slab to provide phase cancellation for fields propagated through the first layer.

6.3. Cylindrical geometry: pseudocanalizing hyperlens

6.3.1. Introduction

In order to apply these results to a hyperlens we need to extend these results from planar to cylindrical geometry. To achieve this we rely on our discussion on wave propagation in cylindrical HMMs (section 4.4).

A hyperlens, due to cylindrical geometry, has a magnification $M = r_2/r_1$, where r_1 is the radius of the inner interface and r_2 is the radius of outer surface of the hyperlens. After the waves propagate from the inner to the outer interface the wave vectors of the wave components are scaled by [following from eq. (4.11)]

$$k_\theta = k'_\theta / M, \quad (6.19)$$

where k'_θ is the initial wave number. When implementing pseudocanalization in cylindrical geometry, the question arises which properties should the second (compensation) layer have. The conditions that held in the planar case [eqs. (6.12) and (6.13)] are no longer valid, as they neglect effects of magnification.

The aim of the pseudocanalization approach is to cancel out phase propagation. In planar geometry this is straightforward, as the phase propagation is given by the real part of the propagation constant k_z . However, in cylindrical geometry this is not as easy. In planar geometry we worked with plane waves, which allow for the calculation of phase accumulated during propagation. In cylindrical geometry we instead need to work with Bessel functions, which offer no analytical expression for phase. In section 4.4 we described an approximate approach using (scaled) plane waves to describe wave propagation in cylindrical geometry. In this approach we assume a plane wave, but allow the propagation constant k_r to vary with propagation, in order to incorporate effects of magnification.

As the magnification in real space corresponds to a scaling of k_θ [as per eq. (4.11)],

6.3. Cylindrical geometry: pseudocanalizing hyperlens

we expect that this effect could be compensated by scaling the dispersion relation of the second medium (scaling in direction of k_θ). This is achieved by scaling ε_r . We now assume that a simple scaling of the second medium is sufficient to compensate for effects of magnification. In others words we seek

$$\varepsilon_r'^{(2)} = \varepsilon_r^{(2)} / \sigma^2, \quad (6.20)$$

such that the final phase is zero for all k_θ [calculated using eq. (4.13)]

$$\text{Re} \int_{r_1}^{r_1+d_1} k_r^{(1)} dr = -\text{Re} \int_{r_1+d_1}^{r_2} k_r^{(2)} dr.$$

Inserting eqs. (4.14) and (6.20) into the above equation and carrying out integration results an equation that can be solved for the scaling factor

$$\sigma = \ln \left[(M+1)^2 / 4 \right] / \ln \left[(M+1)^2 / 4M^2 \right].$$

Furthermore we can assume small magnification ($M \sim 2 \dots 3$) in which case the above expression can be simplified to

$$\sigma = -\sqrt{M}. \quad (6.21)$$

From the results above we see that in order to counteract the effects of magnification, the parameters of the second medium should be scaled relative to the parameters given by eqs. (6.12) and (6.13):

$$\varepsilon_r^{(2)} = \varepsilon_r'^{(2)} / M. \quad (6.22)$$

6.3.2. Type-I hyperlens

We start with exploring type-I HMM, here we can show that pseudocanalization indeed gives the same results as canalization via scaling the permittivity tensor. Crucially, we see that the full-wave numerical results indicate that pseudocanalizing behavior is well achieved, despite the approximations we made to reach conditions for pseudocanalization in a cylindrical system

For the pseudocanalizing type-I HMM we make a relatively straightforward choice

6. Magnetic dark-field hyperlens

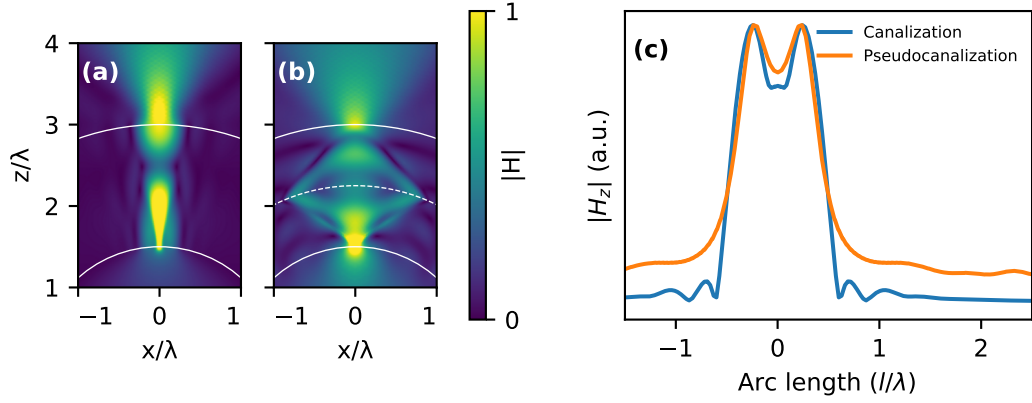


Figure 6.7.: (a,b) Point source on a inner surface of a canalizing bright-field hyperlens (a) and a pseudocanalizing bright-field hyperlens (b). (c) Fields on outer interface of hyperlens due to two closely placed (separated by $\lambda/4$) point sources on the inner interface.

to have material parameters of form

$$\begin{aligned}\varepsilon_o^{(1)} &= 1 + \gamma i, \\ \varepsilon_e^{(1)} &= -1 + \gamma i,\end{aligned}$$

from which we can get the parameters of the compensation layer using eqs. (6.12) and (6.13) [along with correction for magnification, per eq. (6.22)]. For this chapter we fix the losses to $\gamma = 0.05$. On one hand this value is high enough so that the losses already play a role in the results and we thus can reason about behaviour of (a more) realistic case. At the same time the losses are still low enough, not to too much obscure the imaging process. Recalling discussion in section 3.2.4 we note that increased losses result in broadening of the beams in the HMM.

For comparison we compare this pseudocanalizing hyperlens to a (conventional) canalizing hyperlens. In general we look for material parameters in form of

$$\begin{aligned}\varepsilon_o &= \xi^{-1} + \gamma_o i, \\ \varepsilon_e &= -\xi + \gamma_e i.\end{aligned}$$

Here we choose canalization factor $\xi = 5$. The loss parameters γ_o , γ_e were then chosen to result in comparable attenuation to the pseudocanalizing system, giving $\gamma_o = 0.02$, $\gamma_e = 2.20$.

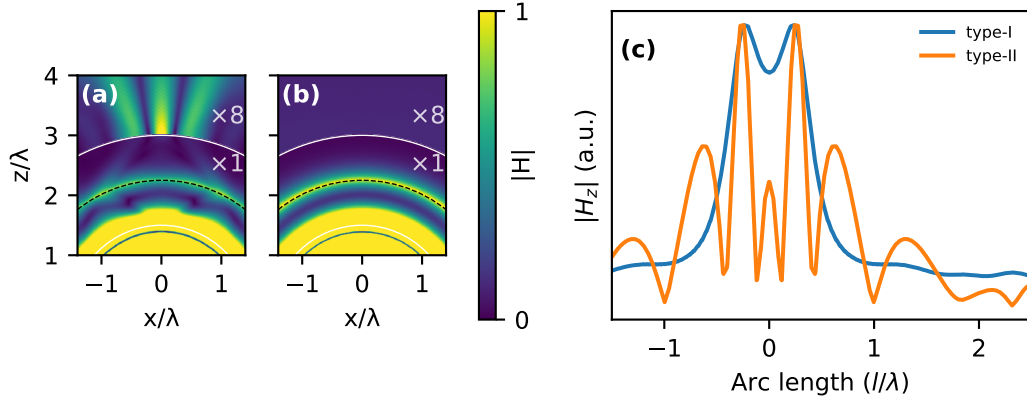


Figure 6.8.: (a) Fields after scattering from a dielectric scatterer and propagating through a pseudocanalizing dark-field hyperlens. (b) Same excitation and hyperlens as in (a), but no scatterer. (c) Imaging of two point sources (separated by $\lambda/4$) by a pseudocanalizing type-I and type-II hyperlens.

In fig. 6.7(a) we show behavior of a pseudocanalizing hyperlens. We see that waves from the point source travel in a relatively narrow beam towards the output interface. We can compare the canalizing hyperlens to the pseudocanalizing system in fig. 6.7(b). Here we see the same behavior as in case of slab geometry: waves initially propagate in diverging beams, but due to reversed phase accumulation in the second layer the original fields are restored in the output. As expected, the both approaches give comparable results. The slight difference in outputted waves is due to non-perfect phase compensation in the canalizing system, along with small differences in attenuation of different k-space components.

By simulating two point sources we can show superresolution capacity of these hyperlenses. In fig. 6.7(c) we show fields on outer interface (coming from the two point sources on inner interface). We see that for sources separated by $\lambda/4$ we can still distinguish the two peaks in the output.

6.3.3. Type-II hyperlens

Having demonstrated using type-I HMM that the pseudocanalization works well in cylindrical geometry, we now consider a type-II HMM based pseudocanalizing hyperlens. As we have already covered, filtering of low-k waves in such system gives rise to additional aspects that we need to consider.

In chapter 5 we discussed issues related to the dark-field hyperlens, with one important one being the problem of outcoupling. To properly outcouple fields from

6. Magnetic dark-field hyperlens

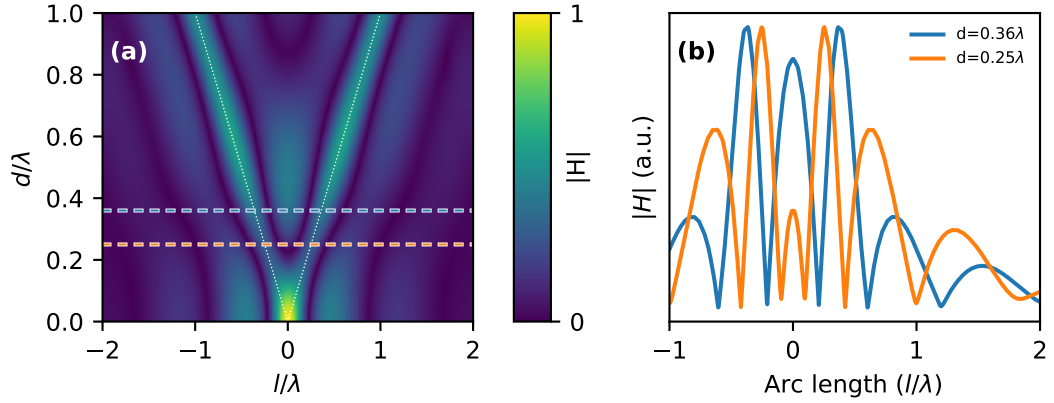


Figure 6.9.: Imaging of two point sources, as a function of source separation d (a). Cuts at separation $d = 0.25\lambda$ and $d = 0.36\lambda$ are shown in (b), highlighting the best and worst-case performance, respectively.

the hyperlens, a high-index medium is needed. We showed how to alleviate this issue with a hybrid design (section 5.4.2), but here we will for simplicity again return to the original design. A high-index medium ($n = 5$) is used outside the hyperlens, so that waves can easily be outcoupled.

We show operation of type-II based hyperlens in fig. 6.8(a). Here, we image a small scatterer ($n_{\text{scat}} = 1.5$, diameter $\lambda/10$) near the inner surface of the hyperlens. To excite the scatterer we have a point source at the origin of the system, providing a background mode with an angular momentum mode $m = 0$ ($k_\theta = 0$). In the output fields we see the characteristic sidelobes, result of the low- k filtering (as discussed in section 6.2.3). For comparison, in fig. 6.8(b) we have the same simulation, but without the scatterer. Here we see that the incident radiation is strongly filtered and thus not present in the output, again showing that dark-field operation is unaffected by pseudocanalization. We note that the surface mode between the two HMM layers is visible in fig. 6.8(a), although it has no influence on the imaging properties of the hyperlens.

We also need to explore the subwavelength imaging properties. In the case of type-I hyperlens interpreting the image is more straightforward, and consequently estimation of hyperlens resolution is also easier. Here, due to the presence of sidelobes, the situation is more complex: the width of the fields from a point source (PSF, point spread function) is now wider, due to the sidelobes — however the sidelobes also mean that the central beam is narrower, possibly helping to distinguish different peaks. In fig. 6.8(c) we compare identical cases of two point sources separated

by $\lambda/4$, imaged through either a bright- or a dark-field pseudocanalizing hyperlens. In this particular case we note that the high-pass filtering of the dark-field hyperlens results in an edge enhancement behavior: the two peaks are particularly well resolved.

However, this edge enhancement does not work universally well for all source separations. In fig. 6.9(a) we show fields on output of the dark-field hyperlens as function of separation between point sources. Indeed we see that for example in case $d = 0.25\lambda$ the two point sources are clearly distinguished. However, due to constructive interference between the sidelobes we see that the contrast between the main peaks and the sidelobes can be quite low. Here the worst case is for $d = 0.36\lambda$, where the contrast between the main peak and the central sidelobe is just 15.6%.⁸

For hyperlenses discussed here (figs. 6.7 and 6.8) we can claim similar superresolution performance, where both hyperlenses shown reached a resolution of around $\lambda/4$. The dark-field hyperlens showed similar performance, albeit with slightly different character. Here, depending on material properties, the sidelobes due to low-k filtering can significantly alter imaging properties of the device.

6.4. Summary

In this chapter we introduced the pseudocanalization idea, where by the use of two complementary slabs the phase propagation is cancelled. In an ideal case this means waves on the input and output interface are identical. To cancel the output phase the second slab has to have reversed phase propagation (compared to the first slab), which can be achieved by using μ -negative HMMs.

We began by exploring pseudocanalization with planar slab structures, showing simulations of the effect in case of both type-I and type-II HMM structures. In particular we showed that in pseudocanalizing system the dark-field operation of the HMM is preserved, unlike in conventional canalizing HMM. We discussed additional complications arising from the low-k cutoff present in type-II hyperbolic media. We also showed that in limited cases pseudocanalization can be achieved with nonmagnetic media as well, albeit only for high-k waves.

We also covered the use of pseudocanalization in cylindrical geometry, where effects of the magnification have to be accounted for. We showed that pseudocanalization offers comparable performance with type-I hyperlens. For type-II hyperlens

⁸This is comparable to performance seen for the type-I pseudocanalizing hyperlens, as we showed in fig. 6.7.

6. *Magnetic dark-field hyperlens*

it offers significant improvement, in effect allowing to combine canalizing behaviour with dark-field imaging.

7. Surface waves

This chapter is based on
in-progress manuscript (J3).

7.1. Motivation

In the previous chapter we introduced the pseudocanalization effect in magnetic hyperlens and discussed how this allows to overcome crucial drawbacks of non-magnetic dark-field hyperlens. Although the pseudocanalization idea is elegant in theory, it lacks real-world applicability: achieving magnetic material properties in optical metamaterials is difficult. Magnetic effects in optics are usually achieved with resonant structures, and so any material losses will have a strong detrimental effect and thus making practical applications unlikely.

Here we turn our attention to another platform for hyperbolic waves: surface waves on anisotropic interfaces. By anisotropic interfaces we mainly mean interface between an anisotropic and isotropic media, but we will also need to consider three-layer systems, where one or more layers are anisotropic. For simplicity of notation we will refer to those systems also as anisotropic interfaces, although technically we are discussing waveguide modes, not a surface wave on an interface.

In this chapter we will start from the single interface between an anisotropic and an isotropic medium and discuss conditions and properties of hyperbolic waves in such media. Later we continue to show how to implement reversed phase propagation using three-layer systems.

7.2. Surface waves on a single interface

7.2.1. Isotropic interface

We start by considering an interface between two semi-infinite layers, described by isotropic permittivities ε_1 and ε_2 . The geometry is shown in fig. 7.1(a): we have metal-dielectric interface at $y = 0$, with metal extending to $y < 0$ while the dielectric

7. Surface waves

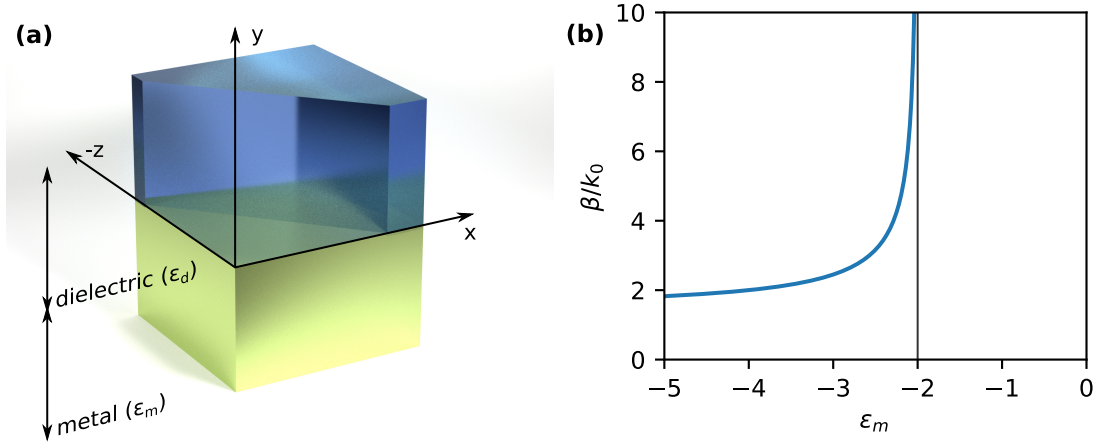


Figure 7.1.: (a) Geometry of the metal-dielectric interface considered in this chapter. (b) Propagation of a surface mode of a metal-dielectric interface, described by ϵ_m and $\epsilon_d = 2$.

layer occupies $y > 0$. We then assume a plane wave solution, propagating towards z -direction (with propagation constant β):

$$\mathbf{E}^{(i)} = E_0^{(i)} \left(-k_z \hat{y} + k_y^{(i)} \hat{z} \right) \exp \left(i\beta z + ik_y^{(i)} y \right), \quad (7.1)$$

where propagation constants in the layers ($k_y^{(i)}$) are calculated from the dispersion relation of an isotropic medium [eq. (2.13)]. Note that we have chosen $\mathbf{E}^{(i)}$ such that

$$\mathbf{H}^{(i)} = -E_0^{(i)} \epsilon_0 \epsilon_i \omega \exp \left(i\beta z + ik_y^{(i)} y \right) \hat{x}, \quad (7.2)$$

as can easily be verified using eq. (2.4). Inserting eq. (7.1) into Maxwell's equations and enforcing interface conditions at $y = 0$ and then solving for propagation constant β yields

$$\beta = \sqrt{\frac{\epsilon_1 \epsilon_2}{\epsilon_1 + \epsilon_2}}. \quad (7.3)$$

From solution we see that surface mode can only exist when condition

$$\epsilon_1 < -\epsilon_2 \quad (7.4)$$

is satisfied. We point out analogy with bulk waves, where we have condition $\epsilon > 0$ for a medium to support propagating waves. In fig. 7.1(b) we plot surface mode propagation constant [eq. (7.3)] as function of ϵ_1 , highlighting the fact that as surface mode approaches the critical limit ($\epsilon_1 = -\epsilon_2$) the propagation constant tends

to infinity.

Phase propagation direction We shall also make a note of phase propagation direction (in regards to energy propagation direction). In a isotropic dielectric the phase and energy propagation directions coincide, as expected. However due to interface conditions between the metal and the dielectric the Poynting vector is flipped in the metal layer.¹ We look at solution where $\beta > 0$ and calculate energy propagation direction of that solution. To consider energy propagation direction for the whole system we need to average energy flux over the metal and dielectric regions. Writing out the z component of the time-averaged Poynting vector $\mathbf{S} = \frac{1}{2} \mathbf{E} \times \mathbf{H}^*$ we get

$$S_z = -\frac{1}{2} E_y H_x^*,$$

where we used $E_x = 0$. From the chosen plane wave solution [eq. (7.1)] we can insert E_y and H_x into the equation above to yield

$$S_z^{(i)} = -\frac{1}{2} \omega \varepsilon_0 \varepsilon^{(i)} k_z \left| E_0^{(i)} \right|^2 \exp \left[-2 \operatorname{Im} \left(k_y^{(i)} \right) y \right]. \quad (7.5)$$

We are interested in ratio of energy propagating backwards (in the metal layer) to energy propagating forward (in the dielectric layer)

$$p = \frac{\int_0^\infty S_y^{(1)} dy}{-\int_0^{-\infty} S_y^{(2)} dy}. \quad (7.6)$$

We insert eq. (7.5) into the above equation and use $\int_0^\infty \exp(-\alpha x) dx = \alpha^{-1}$ to reach

$$p = \frac{\varepsilon_1 \operatorname{Im} k_y^{(2)} \left| E_0^{(1)} \right|^2}{\varepsilon_2 \operatorname{Im} k_y^{(1)} \left| E_0^{(2)} \right|^2}. \quad (7.7)$$

Here we recall interface conditions, which dictate $\varepsilon_1 E_y^{(1)} = \varepsilon_2 E_y^{(2)}$ (from continuity of E_y) and $E_0^{(1)} k_y^{(1)} = E_0^{(2)} k_y^{(2)}$ (from continuity of E_z). This can be used to reach

$$p = \frac{\varepsilon_2^2}{\varepsilon_1^2}. \quad (7.8)$$

¹Here the important term is $\varepsilon_i E_y$, which is conserved across the interface. Due to opposing signs of $\varepsilon_1, \varepsilon_2$ E_y flips sign across the interface. Looking at the component of Poynting vector along the propagation direction (towards z) $P_z = \frac{1}{2} E_y H_x^*$ we see that energy propagation direction in the metal and dielectric layers are opposite.

7. Surface waves

Note that from eq. (7.4) it follows that $p > 1$ and thus energy and phase propagation directions coincide for all surface waves on an *isotropic* interface.

To summarize, we have now shown that an interface between two isotropic media can support propagating surface mode [given that eq. (7.4) is fulfilled], where energy and phase propagation directions coincide.

7.2.2. Anisotropic interface

We now seek to reach description of an anisotropic interface, which would support modes analogous to waves in bulk HMMs. To achieve that we need to design an anisotropic interface such that it support propagating waves in one direction but not the other, thus mimicking behavior of bulk HMMs. For discussion here we assume an interface between an anisotropic medium [with permittivity tensor $\hat{\epsilon} = \text{diag}(\epsilon_e, \epsilon_o, \epsilon_o)$] and an isotropic dielectric, with permittivity ϵ_d .

First we note that in HMMs the two permittivity tensor components are symmetric (as we have considered 2D case), meaning that we can flip ϵ_o , ϵ_e and this flips the dispersion relation (switching k_x , k_y). This is not the case with anisotropic interface, as in here the two components do not appear in a “symmetric” fashion in the equations.

Compared to the isotropic case we need to consider all the modes in the system (while before we were just looking at the TM mode). In an isotropic dielectric layer we consider TM and TE modes, given by

$$\mathbf{H}_{\text{TM}} = E_0^{\text{TM}} (-k_z \hat{\mathbf{x}} + k_x \hat{\mathbf{z}}) \exp(i\mathbf{k}^{(d)} \mathbf{r}), \quad (7.9)$$

$$\mathbf{E}_{\text{TE}} = E_0^{\text{TE}} (-k_z \hat{\mathbf{x}} + k_x \hat{\mathbf{z}}) \exp(i\mathbf{k}^{(d)} \mathbf{r}), \quad (7.10)$$

where corresponding \mathbf{E}_{TM} and \mathbf{H}_{TE} can be reached using Maxwell’s curl equations [eqs. (2.3) and (2.4)]. Wavevector in the dielectric layer is given by

$$\mathbf{k}^{(d)} = k_x \hat{\mathbf{x}} + k_y^{(d)} \hat{\mathbf{y}} + k_z \hat{\mathbf{z}}, \quad (7.11)$$

where k_x , k_z describe propagation of the surface wave (and are conserved across the layers due to the interface conditions), while $k_y^{(d)}$ describes evanescent decay of the surface mode in the dielectric medium.

For the anisotropic layers we take the dispersion relations of the ordinary and the extraordinary wave [eqs. (2.20) and (2.21)], which after solving yield the expres-

7.2. Surface waves on a single interface

sions for isotropic and anisotropic propagation constants $k_z^{(o)}$, $k_z^{(e)}$, respectively:

$$k_z^{(o)} = \sqrt{\mu\varepsilon_o k_0^2 - k_x^2 - k_y^2}, \quad (7.12)$$

$$k_z^{(e)} = \sqrt{\mu\varepsilon_o k_0^2 - (k_x^2 + k_y^2) \varepsilon_o / \varepsilon_e}, \quad (7.13)$$

which we can insert back into the wave equation [eq. (2.18)] to reach expressions for field components for ordinary and extraordinary mode

$$\mathbf{E}_o = E_0^o \left(-k_z \hat{\mathbf{y}} + k_y^{(o)} \hat{\mathbf{z}} \right) \exp \left(i \mathbf{k}^{(o)} \mathbf{r} \right), \quad (7.14)$$

$$\mathbf{E}_e = E_0^e \left[- (k_0^2 \varepsilon_o - k_x^2) \hat{\mathbf{x}} + k_y^{(e)} k_x \hat{\mathbf{y}} + k_z k_x \hat{\mathbf{z}} \right] \exp \left(i \mathbf{k}^{(e)} \mathbf{r} \right). \quad (7.15)$$

Here the wavevectors are

$$\mathbf{k}^{(o)} = k_x \hat{\mathbf{x}} + k_y^{(o)} \hat{\mathbf{y}} + k_z \hat{\mathbf{z}}, \quad (7.16)$$

$$\mathbf{k}^{(e)} = k_x \hat{\mathbf{x}} + k_y^{(e)} \hat{\mathbf{y}} + k_z \hat{\mathbf{z}}, \quad (7.17)$$

with $k_y^{(o,e)}$ given by eqs. (7.12) and (7.13).

Propagation along the z -axis (i.e. perpendicular to the optical axis, x -axis) has a simple solution: as electric field has only y and z components the fields interacts just with ε_o component of the anisotropic permittivity. Thus the conditions for isotropic propagation are recovered, as given by eqs. (7.3) and (7.4).

However, for propagation along x -axis, both ε_o and ε_e terms will be present, due to y and x components of the electric field, respectively. That means we need to derive another propagation constant and corresponding propagation conditions, mirroring eqs. (7.3) and (7.4). To find the propagation constant for extraordinary mode we take $k_z = 0$, write out the equations for enforcing continuity of E_x , D_y and E_z and then solve for k_x (here β_e , to signify it as the propagation constant for the extraordinary mode) to get

$$\beta_e = \sqrt{\frac{\varepsilon_e \varepsilon_d - \varepsilon_d^2}{\varepsilon_e - \varepsilon_d^2 / \varepsilon_o}} \quad (7.18)$$

as the propagation constant. From this we identify

$$\varepsilon_e < \frac{\varepsilon_d^2}{\varepsilon_o} \quad (7.19)$$

as the condition for the interface to support a propagating mode along the z direc-

7. Surface waves

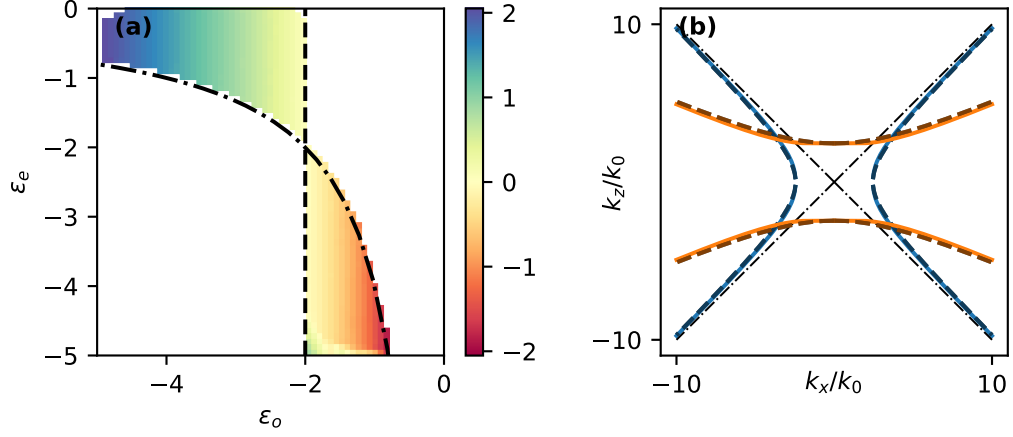


Figure 7.2.: (a) Energy propagation direction of the surface mode of the anisotropic interface given by $\varepsilon_o, \varepsilon_e$ ($\varepsilon_d = 2$ is assumed). The dashed line indicates condition given by eq. (7.4) and dot-dashed line eq. (7.19). As discussed in the text these conditions separate HSWs into type-1 and type-2 mode. (b) Numerically calculated dispersions of type-1 and type-2 HSWs (parameters in the text). Dashed lines indicate dispersions of corresponding HMMs, as per eqs. (7.4) and (7.19).

tion.

Hyperbolic surface waves Now we can introduce the concept of hyperbolic surface waves (HSWs). We first note that hyperbolic dispersion of HMMs arises from the fact that the HMM supports propagating waves in one direction, but not the other. This means that the system exhibits a transistion, where depending on direction in the medium the waves enter from the propagating regime to the nonpropagating regime (see introduction to HMMs in chapter 3). Having derived equations for propagation perpendicular to the optical axis [“ordinary propagation”, eqs. (7.3) and (7.4)] and along the optical axis [“extraordinary propagation”, eqs. (7.18) and (7.19)] we can implement an analogous idea: by choosing the material parameters such that one of the propagation conditions is fulfilled and the other is not, we produce a system that also exhibits this transistion between propagating and nonpropagating regimes. We then classify hyperbolic surface waves (HSWs) into two types, similar to division of HMMs to type-I and type-II. For interfaces where eq. (7.4) is fulfilled [and eq. (7.19) is thus not fulfilled], i.e. we have

$$\varepsilon_o < -\varepsilon_d, \quad (7.20)$$

$$\varepsilon_e > \frac{\varepsilon_d^2}{\varepsilon_o}, \quad (7.21)$$

we designate the surface waves there as type-1 surface waves.² The opposite case, when eq. (7.19) is fulfilled, we classify as type-2 HSWs. In fig. 7.2(a) we plot these conditions to indicate parameters for the two kinds of HSWs. The figure also shows that the two types of HSWs have opposite phase propagation directions. We will return to this question in more details in end of this section on page 99.

There is no explicit form analytical solution for an dispersion of the HSWs, although it is possible to reach a dispersion relation in implicit form [58, 59]. However, here we will be content with solving the dispersion relation numerically.³ We use the same convention as we used for HMM discussions: we shall be looking at propagation in the z direction. So we numerically solve the equations for the surface mode to yield the propagation constant k_z as function of k_x . In fig. 7.2(b) we show dispersion of a type-1 ($\varepsilon_o = -3$, $\varepsilon_e = -1$) and a type-2 HSW ($\varepsilon_o = -1$, $\varepsilon_e = -7$).

Although we abstained from deriving a generic equations for dispersion relation of HSWs, we can reach an asymptotic solution for large k limit. As we let $k_x, k_z \rightarrow \infty$ and enforce the interface conditions, we note that the ordinary mode and TE mode disappear in the high- k limit and thus we easily get an expression for slope of the hyperbolic dispersion $\tau \equiv k_z/k_x$:

$$\tau = \pm \sqrt{-\frac{\varepsilon_d^2 - \varepsilon_o \varepsilon_e}{\varepsilon_d^2 - \varepsilon_o^2}}. \quad (7.22)$$

Effective HMM parameters for an anisotropic interface Given our motivation of exploring HSWs as an alternative for HMMs we shall now establish a relation between an anisotropic interface and parameters for a corresponding HMM.

We start from HMM dispersion and note that instead of using the HMM parameters $\varepsilon'_o, \varepsilon'_e$ we can equivalently describe the HMM using limiting wavenumber⁴ k_c [$k_z(k_x = 0)$ for type-I; $k_z(k_x = 0)$ for type-II HMM] and slope of the hyperboloid [$\tau = \lim_{k_x \rightarrow \infty} k_z(k_x)/k_x$]. Here we use prime to distinguish between parameters of the anisotropic medium of the surface mode ($\varepsilon_o, \varepsilon_e$) from parameters of corresponding HMM ($\varepsilon'_o, \varepsilon'_e$). Considering a type-I HMM we find the expressions for k'_c and τ'

²We use here type-1 and type-2 to make it clear that we are talking about HSW dispersions, reserving type-I and type-II for HMMs.

³The choice of not pursuing the mathematical solution further is also motivated by anticipation of trouble for three-layer system, which we will cover in the coming pages. We will anyway will be forced to resort to numerically solving the HSW dispersion, so we here avoid the additional trouble of obtaining rigorous mathematical solutions for cases where numerical solutions are satisfactory.

⁴By the term “limiting wavenumber” I mean lower bound for k_z in type-I HMM and the cut-off wavenumber in type-II HMMs. When plotting the isofrequency contours the limiting wavenumber k_c corresponds to the length of the shortest wavevector allowed by the dispersion relation.

7. Surface waves

from eq. (2.21):

$$\tau' = \sqrt{-\frac{\varepsilon_o'}{\varepsilon_e'}}. \quad (7.23)$$

$$k_c' = \sqrt{\varepsilon_e'} k_0, \quad (7.24)$$

For type-II HMM expression for limiting wavenumber is instead given by

$$k_c' = \sqrt{\varepsilon_o'} k_0. \quad (7.25)$$

Similarly we can use τ and k_c to describe dispersion of HSWs. We have already derived an expression for τ [eq. (7.22)]. The limiting wavenumber k_c is given either by eq. (7.3) for type-1 or by eq. (7.18) for type-2 HSWs.

Having calculated τ and k_c corresponding to a HSW dispersion we can then use eqs. (7.23) and (7.24) to calculate “effective HMM” parameters

$$\varepsilon_o' = \frac{k_c^2}{k_0^2}, \quad (7.26)$$

$$\varepsilon_e' = -\frac{k_c^2}{k_0^2 \tau^2}. \quad (7.27)$$

For type-2 HSWs we instead have (from eqs. (7.23) and (7.24))

$$\varepsilon_o' = -\frac{k_c^2}{k_0^2} \tau^2, \quad (7.28)$$

$$\varepsilon_e' = \frac{k_c^2}{k_0^2}. \quad (7.29)$$

We use these expressions to calculate corresponding effective HMM dispersions in fig. 7.2(b), indicating a good (but not perfect) correspondence between HSWs and HMMs. We further explore this analogy in fig. 7.3, where using full-wave simulations calculate fields plots of both an anisotropic interface [fig. 7.3(a)] and a corresponding HMM [fig. 7.3(b)].

Numerical simulations of HSWs It should be noted that numerical simulations of HSWs are computationally considerably expensive, as 3D simulations are needed. These simulations are carried out using the finite-element method (using COMSOL Multiphysics), which is particularly sensitive to the mesh size, especially in 3D. Usu-

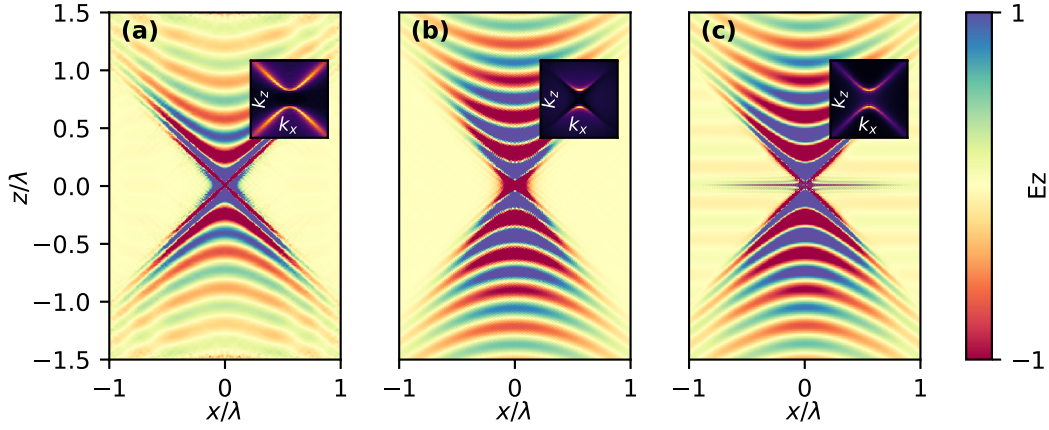


Figure 7.3.: Fields on an anisotropic interface (a), fields in a corresponding HMM (b) and fields on the interface calculated semianalytically (c).

ally the finite-difference time domain (FDTD) method can be used when FEM memory requirements become a significant barrier, however in this case FDTD is not of much help: FEM allows to use higher-order elements, i.e. in simulations shown here cubic basis functions were used. This allows to achieve suitable resolution with larger mesh elements. FDTD mesh corresponds to linear basis functions in FEM terms, requiring finer mesh to properly resolve the field details.

As we can numerically calculate the HSW dispersion, we can also calculate propagating fields. We use the same approach we took in chapter 6, where we calculated the fields using the propagation equation eqs. (6.4) and (6.5). In case of single interface, where we have no reflections in the system, this approach should produce exactly same result as a proper full-wave simulation. Semianalytically calculated fields are shown in fig. 7.3(c), where we see that the fields correspond relatively to full-wave simulations [fig. 7.3(a)].

Phase propagation direction Finally we return to the question of phase propagation direction. For isotropic case we derived eq. (7.8), which followed straightforwardly from the interface conditions. A particular annoyance in case of anisotropic interfaces is that the HSWs are mixtures of modes (TE and TM in the dielectric medium and ordinary and extraordinary modes in the anisotropic medium) — this leads to multiple terms in evaluating Poynting vector, making it difficult to reach a simple expression. To reach an analytic (and instructive) solution we need to take a series of approximations and assumptions. We are somewhat aided by the fact that we primarily care whether $p < 1$ or $p > 1$: i.e. whether majority of the energy

7. Surface waves

propagates in the metal or in the dielectric. As we are interested in large k_x regime, we simplify the dispersion relations [eqs. (2.20) and (2.21)] by dropping k_0 terms. We again start from z component of time-averaged Poynting vector

$$S_z = \frac{1}{2} (E_x H_y^* - E_y H_x^*) .$$

Here we neglect $E_x H_y^*$ term to reach an approximate expression for eq. (7.6).

$$p \approx - \frac{i |E_0^{(2)}|^2 (\tau^2 + 1) \sqrt{\varepsilon_o}}{k_x \varepsilon_d \sqrt{\tau^2 \varepsilon_o + \varepsilon_e} E_0^{(1,e)} E_0^{(1,o)*}} \quad (7.30)$$

To fix the scaling constants $E_0^{(i)}$ we again employ interface conditions. Continuity of E_x fields gives us

$$\frac{E_0^{(2)}}{E_0^{(1,e)}} = \frac{\varepsilon_d}{\sqrt{-\tau^2 - 1}} \quad (7.31)$$

and from continuity of H_x field we get

$$E_0^{(1,o)} \approx \frac{\tau E_0^{(2)}}{k_x} + \mathcal{O}(E_0^{(2,TE)}) , \quad (7.32)$$

here we made approximation by assuming that effect of the TE mode is negligible. Inserting eqs. (7.22), (7.31) and (7.32) into eq. (7.30) yields a simple *approximate* solution for the ratio of energy fluxes

$$p \approx - \frac{\varepsilon_o}{\varepsilon_d} . \quad (7.33)$$

Although we made a series of aggressive approximations the resulting expression is quite useful. Most importantly, in fig. 7.2(a) we numerically show that the expression correctly predicts whether energy propagates mostly in the anisotropic layer ($p < 1$) or the dielectric ($p > 1$), indicating direction of energy propagation.

Equation (7.33) tells us that phase propagation is opposite between type-1 and type-2 HSWs.⁵ This is an important result, especially in light of isotropic surface waves, where phase propagation always coincides with energy propagation.

⁵This can be expected also from analogy with waves in HMMs: as we discussed (chapter 3), the type-I HMMs exhibit negative refraction, indicating reversed phase propagation.

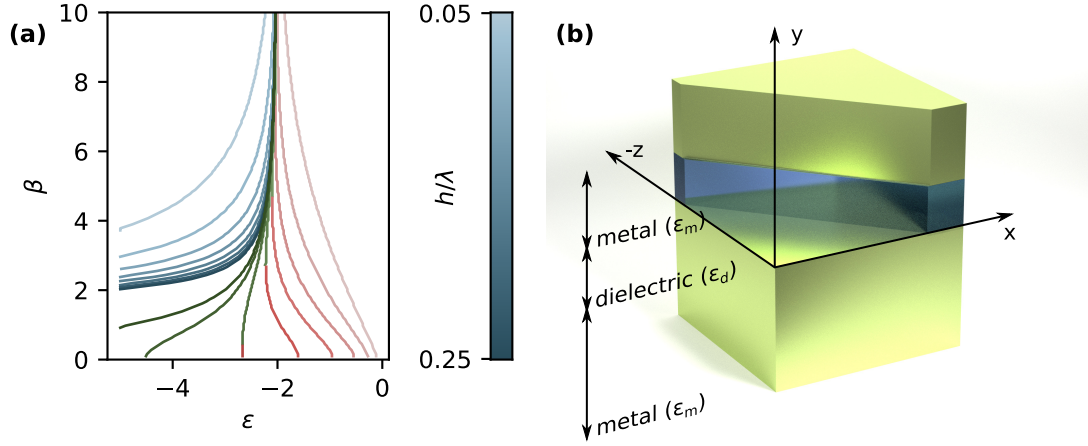


Figure 7.4.: (a) Propagation constant of modes in three-layer system for various spacer layer thicknesses. Blue lines indicate even modes, while green (red) lines indicate odd modes with normal (reversed) phase propagation direction. (b) Problem geometry for isotropic three-layer system. A dielectric layer with thickness h is sandwiched between two metal layers.

7.3. Surface waves in a three-layer system

7.3.1. Introduction

Motivation for use of a three-layer system comes from Shin and Fan [60] where they discussed negative refraction of surface waves using a three-layer system. Our aim of pseudocanalization is in a way similar idea, but applied to anisotropic media.

Again, we will follow a similar approach as in the previous section: we will first analyze the isotropic case, discussing the modes existing in three-layer system. Crucially (from the viewpoint of pseudocanalization) we again will consider the phase propagation direction. Here we will see that even in an isotropic case the system can exhibit negative phase propagation, i.e. case where energy and phase propagate in the opposite directions.

7.3.2. Isotropic system

We first look into symmetric three layer system [fig. 7.4(b)], consisting of two semi-infinite metallic layers ($\epsilon_1 < 0$), separated by a dielectric layer ($\epsilon_2 > 0$) with thickness h . Analysis of this system is somewhat complicated by the fact that there is no analytic explicit formula for modes in this three-layer system [5, 61, 62]. However, at least for this case we can derive an implicit equation for the guided modes.

As this is an isotropic system we can once more limit the analysis to TM modes,

7. Surface waves

as TE modes do not support surface modes [5]. We again assume a plane wave solution [eq. (7.1)] and use the interface conditions to reach dispersion relation (in implicit form)

$$\pm \exp\left(ik_y^{(2)}h\right) = \frac{\varepsilon_1 k_y^{(2)} + \varepsilon_2 k_y^{(1)}}{\varepsilon_2 k_y^{(1)} - \varepsilon_1 k_y^{(2)}}, \quad (7.34)$$

where $k_y^{(1,2)}$ are given by the dispersion relations of corresponding media (assuming propagation constant β)

$$k_y^{(i)} = \sqrt{k_0^2 \varepsilon_i - \beta^2}.$$

The system can support two modes, depending on the sign chosen in eq. (7.34). We shall refer to these modes as odd (−) and even (+) modes, indicating parity of the E_y fields. Note that in case of $h = \infty$ we recover solution for the single interface.

We numerically solve eq. (7.34) and plot the solutions for various spacer thicknesses h in fig. 7.4(a). First we note, that as h is increased both even and odd solutions converge towards solution of the single interface [eq. (7.3)], as expected. Second thing to consider is that the even mode is always above the single interface solution, whereas the odd mode is below. As larger β implies larger k_y , this means that the fields on the two interfaces are more strongly coupled for the odd mode. This means that especially for small h the odd solution is significantly altered by coupling of the fields on the two interfaces.

Phase propagation direction Integrating power flux [eq. (7.5)] in the bottom layer yields a straightforward expression

$$\int_{h/2}^{\infty} P_z^{(1)} dy = \frac{i\beta^3 |E_1|^2}{2k_y^{(1)}}. \quad (7.35)$$

In the dielectric spacer we have now two modes, one propagating towards $+z$, the other towards $-z$. From symmetry of the system we get can fix the the amplitudes of the modes and then we get the following result for the integration

$$\int_0^{h/2} P_z^{(2)} dy = \mp \frac{\beta^3 \left(-i \exp\left(-ik_y^{(2)}h\right) \pm 2hk_y^{(2)} + i \exp\left(ik_y^{(2)}h\right) \right)}{\varepsilon_2 k_y^{(2)}}, \quad (7.36)$$

7.3. Surface waves in a three-layer system

where the signs indicate even and odd modes. Calculating ratio of energy fluxes now yields

$$p = -\frac{i\varepsilon_1 k_y^{(1)}}{2\varepsilon_2 k_y^{(2)}} t, \quad (7.37)$$

where

$$t = \begin{cases} \frac{k_y^{(2)} h - \sin(k_y^{(2)} h)}{\sin^2(k_y h/2)} & (\text{odd}) \\ \frac{k_y^{(2)} h + \sin(k_y^{(2)} h)}{\cos^2(k_y h/2)} & (\text{even}) \end{cases}. \quad (7.38)$$

However, we note that to reach $p < 1$ we need t to be small. As t scales with $k_y^{(2)} h$ we take Taylor expansion to as we only care for the regime with a small argument. With this we have

$$t \approx \begin{cases} \frac{2}{3} k_y^{(2)} h & (\text{odd}) \\ 2 k_y^{(2)} h & (\text{even}) \end{cases},$$

which suggests that only the odd mode can offer negative phase propagation direction. This is validated by numerically calculated results shown in fig. 7.4(a).

7.3.3. Anisotropic system

Our aim now is to implement the pseudocanalization concept with surface waves. For that we need to match dispersion of a three layer system with a two-layer system, while keeping energy propagation directions opposite. In this section we consider the anisotropic three-layer system and compare the surface mode to the one discussed in the two layer case.

We consider a symmetric system consisting of a dielectric layer (ε_d) with thickness h , which is sandwiched between two semi-infinite anisotropic layers [$\hat{\varepsilon} = \text{diag}(\varepsilon_e, \varepsilon_o, \varepsilon_o)$], instead of isotropic metallic layer as in fig. 7.4(b). Following from results for the isotropic case we expect even and odd modes existing in the system. Due to amount of field modes in the layers⁶ we do not expect to reach a useful dispersion relation for the general case of anisotropic three layer system. Therefore we

⁶We use the term “field modes” here to distinguish the individual modes [eqs. (7.9), (7.10), (7.14) and (7.15)] in the layers from the solution for the whole set of equations, giving the hyperbolic mode propagating along the interfaces. Here we have in total six field modes entering the equations: forward- and backwards propagating TE and TM modes in the dielectric, along with the ordinary and extraordinary modes in the anisotropic layers.

7. Surface waves

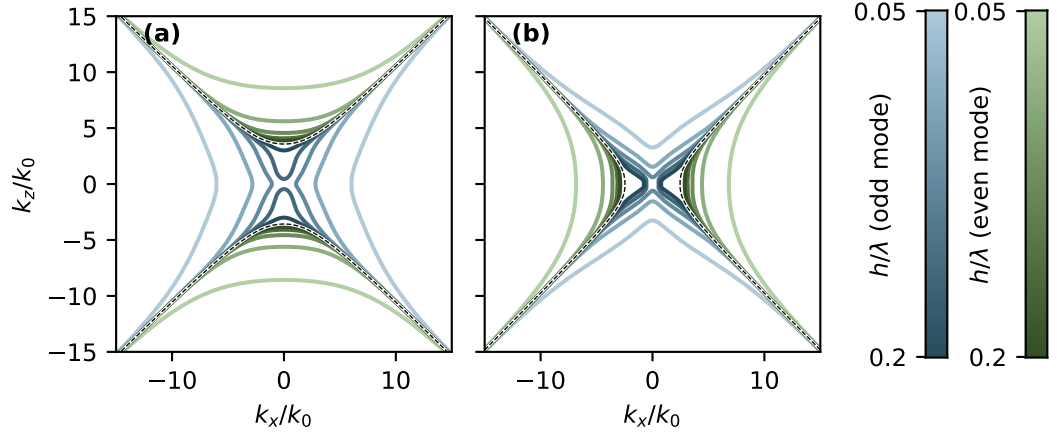


Figure 7.5.: Even (green) and odd modes (blue lines) in symmetric three layer system, for various spacer thicknesses. Both type-1 $\varepsilon_o = -2.37$, $\varepsilon_e = -1$ (a) and type-2 $\varepsilon_o = -1$, $\varepsilon_e = -7$ (b) systems are shown. The black dotted line shows solution from corresponding two-layer system.

will resort to numerical solutions to the equations.

However, there are some useful asymptotic cases that can be noted. Most importantly we note that coupling between the two interfaces scales with $\exp(i k_y^{(2)} h)$. In a limit where we let k_x, k_z to infinity this coupling term goes to zero (as $k_x, k_z \rightarrow \infty$ implies also $k_y^{(2)} \rightarrow \infty$). It follows that the asymptotic behavior is identical to single interface solution, as presented in section 7.2.2. However, in the opposite case of small k_x, k_z we instead are looking at the “strong coupling” limit, dispersion deviates significantly from the one of a single interface. This is especially true for the odd mode, which due its field profile experiences stronger coupling than the even mode.

As we did for HSWs on a single interface, we can in same way classify HSWs in three layer system into type-1 and type-2 HSWs. For a large spacer thickness the three-layer system behaves similarly to a single interface, but for small thicknesses the behavior diverges. We show this in fig. 7.5, where we plot HSW dispersions for a type-1 and a type-2 system for various thicknesses. As discussion of an isotropic case already hinted the even mode is less affected by coupling of fields on the two interfaces. So the even mode behaves similarly the corresponding single interface solution.

However, the odd mode is significantly influenced by coupling, especially with decreasing spacer thickness h . Importantly we note that with the strong coupling we can effectively tune the type-1 HSW look like type-2 mode (and vice versa).

7.3. Surface waves in a three-layer system

Type-2 HSW, for example, exhibits a low-k cutoff for $k_x < 2.5k_0$ [as shown by the dashed black line in fig. 7.5(a)]. We see in fig. 7.5(a) that by decreasing the spacer layer we can tune odd mode of type-1 also exhibit low-k cutoff, in principle behaving close to a type-2 HSW.

Phase propagation direction In section 7.2.2 we derived an expression for the energy flux [eq. (7.33)], assuming the large-k limit. As a three-layer system reduces to a single interface in this limit the results hold here as well, in the large-k limit. However, in context of current discussion more important question is in the strong coupling regime, where coupling between the interfaces strongly alters HSW dispersion. As we noted in before, in this regime the phase propagation can be flipped even in the isotropic case, unlike the single interface. However, reaching simple expressions is increasingly more complicated. In case of an anisotropic system we need to consider 6 fields modes in total, complicating the expressions for the Poynting vectors. Here we will argue about behavior of the modes in relatively general terms, in order to avoid falling into overly complex derivations.

As we showed for isotropic three-layer system, the even mode was identified by larger propagation constant k_z , and thus weaker coupling between the two interfaces. Due to the weaker coupling we assume that the even mode always follows behavior of the single interface solution. This means that on the type-1 interface it will exhibit coinciding energy and phase propagation and on the type-2 interface it phase and energy propagation directions will be antiparallel.

The odd mode on the other hand exhibits stronger coupling between the two interfaces. Indeed, this is the reason why phase propagation can be reversed in the isotropic case. Thus we can expect that the phase propagation direction might not follow from the single interface solution. However, for cases considered here we used numerical calculations to verify that the propagation direction matches the expectation from the single interface solution.

Field profiles In figs. 7.6 and 7.7 we now look at field profiles of the odd and even mode of the type-2 structure [fig. 7.5(b), with spacer thickness $h = 0.1\lambda$]. We show both full-wave FEM simulations and semi-analytical calculations (using numerically calculated propagation constant k_z and eqs. (6.4) and (6.5)). To ensure convergence

7. Surface waves

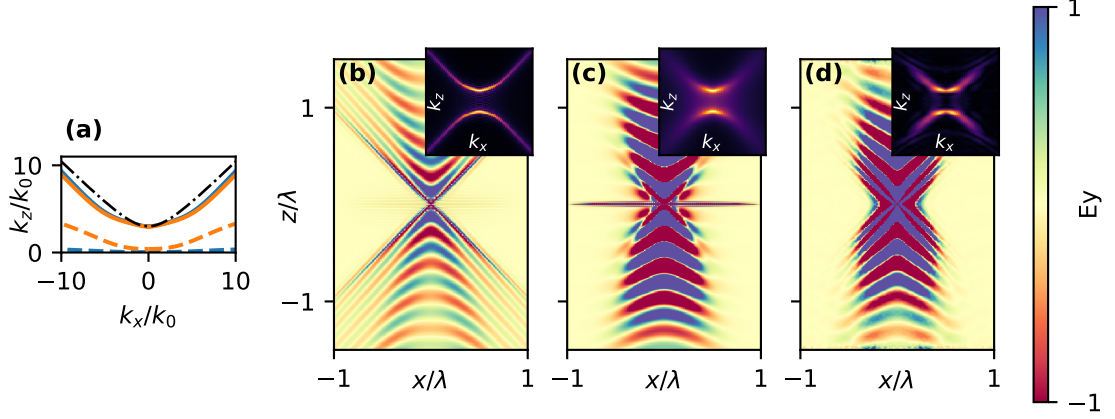


Figure 7.6.: (a) Real and imaginary parts of the propagation constant k_z for the *odd* mode in the three layer system (details in the text) for losses $\gamma = 0.01$ (blue) and $\gamma = 0.1$ (orange). Black line indicates corresponding HMM dispersion. (b,c) Semi-analytically calculated field profiles for losses $\gamma = 0.01$ (b) and $\gamma = 0.1$ (c). (d) Full-wave simulations of the field profile for losses $\gamma = 0.1$. Insets show Fourier transformed fields, showing dispersion of the propagating waves.

in numerical simulations we allow for lossy materials in the calculations:

$$\varepsilon_o = -1.68 + i\gamma. \quad (7.39)$$

$$\varepsilon_e = -3.07 + i\gamma. \quad (7.40)$$

Comparing dispersions for odd and even HSW modes (fig. 7.6(a) and fig. 7.7(a), respectively) shows that the even mode is closer in behavior to solution of the single interface — and thus also a better approximated by an HMM dispersion. In the figure we also plotted dispersion of corresponding HMM, calculated using limiting wavevector k_c (numerically calculated) and τ [eq. (7.22)]. Due to strong coupling the odd mode diverges more from ideal hyperbolic dispersion, which is seen both in the calculated propagation constant [fig. 7.6(a)] and also in the field plots [fig. 7.6(b-d)].

7.3.4. Asymmetric anisotropic system

In the previous section we showed that a symmetric anisotropic three layer system supports two HSW modes. We presented a system that produced a negative phase velocity (in comparison to a “reference” two layer system) for the odd mode. However the system also supports a even mode, which does not produce a desired dispersion for the surface mode. In order to suppress the unwanted even mode we

7.3. Surface waves in a three-layer system

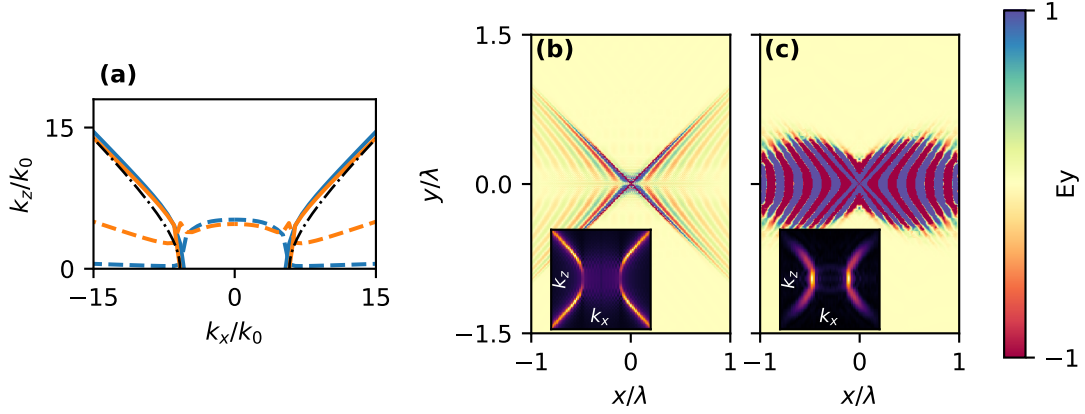


Figure 7.7.: (a) Real and imaginary parts of the propagation constant k_z for the *even* mode in the three layer system (details in the text) for losses $\gamma = 0.01$ (blue) and $\gamma = 0.1$ (orange). The black line shows corresponding HMM dispersion. (b) Semi-analytically calculated field profiles for losses $\gamma = 0.01$. (c) Full-wave simulations of the field profile for losses $\gamma = 0.1$. Insets show Fourier transformed fields, showing dispersion of the propagating waves.

now consider a asymmetric three layer system. The dielectric layer (with thickness $h = 0.1\lambda$) is now sandwiched between the anisotropic medium [given by eqs. (7.39) and (7.40)] and an isotropic metallic medium, given by ϵ_m . In order to avoid any new modes we limit ϵ_m to $-\epsilon_d < \epsilon_m < 0$. This means that interface between ϵ_d - ϵ_m does not support surface mode on its own [recall eq. (7.4)]. As before, in the high-k limit a single interface HSW is restored for the anisotropic interface, as the two interfaces are decoupled. For the low-k regime (i.e. strong coupling between the interfaces) we assume that despite the altered dispersion the phase propagation direction is not changed (in comparison to the symmetric system).

In fig. 7.8(a) we explore effect of ϵ_m on dispersion of the HSW mode. We see that the asymmetric system has significantly altered dispersion in the low-k regime, by flattening out the HSW dispersion in the low-k regime. Looking at propagation of waves [fig. 7.8(b,c)] this manifests as additional beam: we see the usual narrow high-k beams, but also a wider beam propagating straight ahead (corresponding to the flat low-k regime). Of course, this behavior is suboptimal as now this structure can not achieve perfect pseudocanalization for the single anisotropic interface: phase of these low-k waves will not be properly compensated.

7. Surface waves

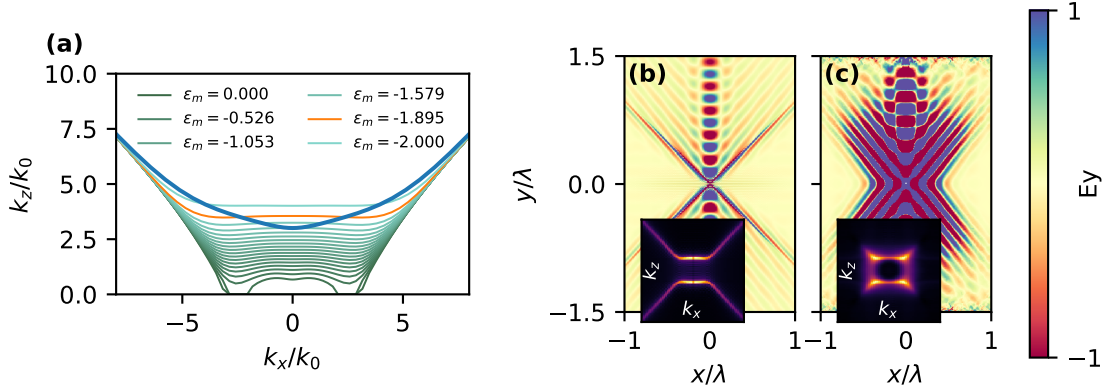


Figure 7.8.: (a) Propagation constant for the symmetric three layer system (blue line) and for asymmetric system, plotted for various different ϵ_m . Orange line indicates $\epsilon_m = -1.89$ chosen for the simulations. (b) Semi-analytically calculated fields for low-loss ($\gamma = 0.01$) system. (c) Simulated fields as per FEM simulations with $\gamma = 0.1$.

7.4. Pseudocanalization with surface waves

We have covered basics of HSWs in two- and three-layer systems and shown that we can engineer the dispersion and phase propagation properties. Now we apply the results to demonstrate pseudocanalization concept with surface waves. As discussed, here we avoid the need for magnetic media, making it (in theory) more viable for an experimental realization. However, we noted that while the dispersion of HSWs on a single interface corresponds relatively well to HMM dispersion, the modes in a three layer system are less closely matched with a single interface HSW dispersion (and subsequently HMM dispersion). Therefore we can not achieve perfect pseudocanalization, as was the case with magnetic HMMs.

As before we combine two media with “complementary” dispersions (see fig. 7.9). One part of the system is an anisotropic interface supporting type-1 HSWs, with $\epsilon_o = -2.48 + 0.1i$ and $\epsilon_e = -0.75 + 0.1i$ [indicated with (2) in fig. 7.9]. The phase-compensating part, with opposite phase propagation, is either realized by symmetric three layer system (fig. 7.6) or asymmetric system (fig. 7.8).

The symmetric system offers better phase compensation, as there the surface waves resemble closely the HSWs on a single anisotropic interface. However, this approach is less practical we artificially suppress the unwanted even mode. As shown in fig. 7.9(a) we excite the waves using two dipoles to ensure that mainly the odd mode is excited.

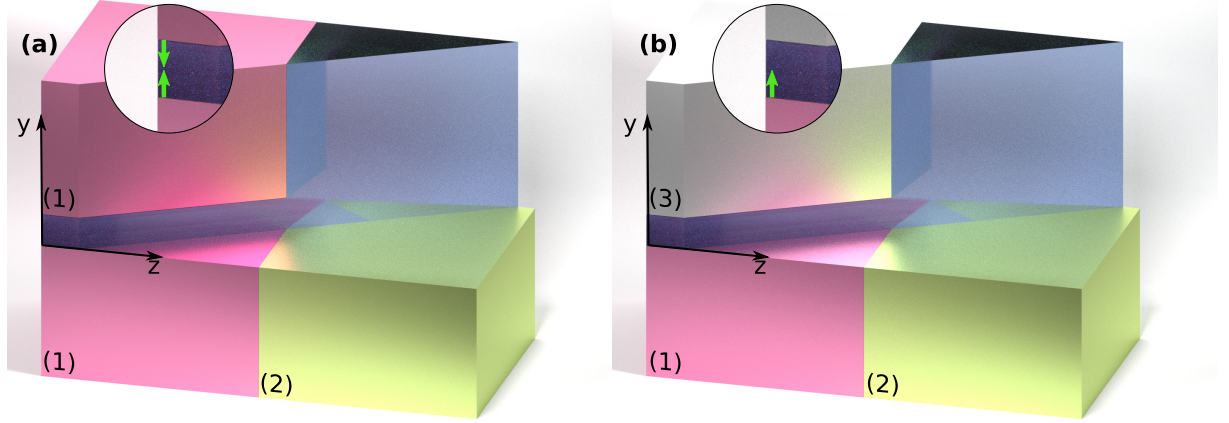


Figure 7.9.: Geometry for the two pseudocanalizing systems, with symmetric (a) and non-symmetric (b) three layer system, with anisotropic media indicated by (1) and (2) and the metal for asymmetric system shown with (c). Insets indicate placement of dipole sources to excite the waves. In (a) the sources are aligned such to only excite the odd mode.

Another approach is to use asymmetric three-layer design, where only the odd-like mode exists. This comes at the cost of distorted HSW dispersion, leading to worse pseudocanalization. However, for this structure we can use a more realistic single point source to excite the waves, without worrying about exciting any unwanted modes.

We show results of full-wave simulations of the structures in fig. 7.10. For comparison we have included semi-analytically calculated fields as well. This approach neglects reflections from the interfaces and here we can no longer make this assumption and thus these calculations are only included for a rough reference. For these proof-of-concept simulations we have not explored the issue of reflections of the surface modes, although from full-wave simulations we see that it is an important aspect. For example, in ref. 60, which discusses negative phase propagation for isotropic surface waves, the authors introduced an optimized system to improve mode overlap to reduce reflections from the three-layer system.

We see that the symmetric system can offer relatively good performance in the low-loss case [fig. 7.10(b)] and in case of higher losses ($\gamma = 0.1$) the performance is expectedly reduced but nevertheless full-wave simulations [fig. 7.10(a)] match relatively well with the simplified calculations [fig. 7.10(c)]. However, for more practical case of asymmetrical design the pseudocanalization performance is degraded even for the simplified calculations [fig. 7.10(e)], while the full-wave sim-

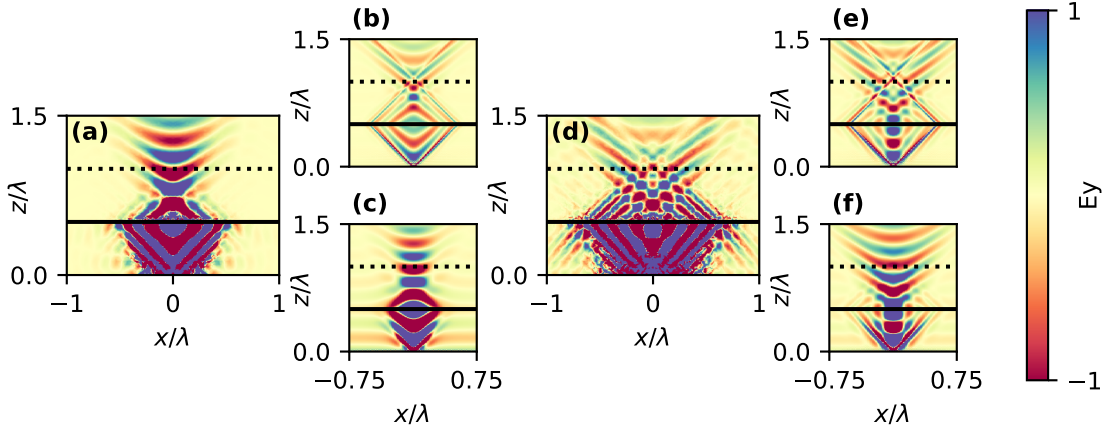


Figure 7.10.: Comparison of surface wave implementations of a pseudocanalizing system. Full-wave simulation results of a symmetric system are shown in (a), with corresponding semi-analytical calculations with reduced losses (b) and full losses (c). Similarly (d) shows FEM results of an asymmetric system, with corresponding semi-analytically calculated fields in (e,f).

ulations [fig. 7.10(d)] show differences with the semi-analytical calculations [fig. 7.10(f)]. This is likely due to reflections from the boundary between the parts of the system, which could be reduced by optimizing overlap between the modes in the two parts.

7.5. Summary

In this chapter we introduced hyperbolic surface waves on both single interfaces and in three-layer systems. Inspired from results with mu-negative HMMs we looked into phase propagation direction these waves. We showed that we can mimic effect of μ -negative media with three-layer system, where coupling between the two interfaces allows to achieve reversed phase propagation without requiring magnetic properties.

Then we showed proof-of-concept simulations showing that the pseudocanalization can be realized with combining two- and three-layer anisotropic systems. By engineering the dispersion properties the two regions can be tuned to have support similar HSWs, but with reversed phase propagation.

However, these results offer only a preliminary look into engineering phase propagation with surface modes. Plenty of questions are still left to be explored.

8. Conclusions

The project started out with the idea of taking the well-known hyperlens concept and substituting the type-I HMM with a type-II. As the type-II HMM reflects low-k waves, the idea had potential as a built-in mechanism for dark-field imaging. Throughout the project we discovered, however, that all the features that were useful (and even necessary) for the bright-field hyperlens turned out to cause difficulties with the type-II based design. The canalization regime, which is crucial in type-I HMM based hyperlens to facilitate straightforward imaging of the object is at odds with dark-field filtering of type-II hyperlens: achieving canalization and dark-field imaging at the same time is not possible. In a similar way the magnification process itself causes the propagating waves in the HMM to turn into evanescent waves during the propagation and reflect back, making it necessary to have very high refractive index outside the hyperlens to allow the waves to couple out of the device.

We studied multilayer based scheme and showed that given some compromises it is in principle possible to design a system, that demonstrates both superresolution and filtering of the incident radiation. We also discussed a hybrid design, combining a type-II HMM with an anisotropic medium with elliptic dispersion, to resolve the issue of outcoupling caused by magnified waves meeting the low-k cutoff. Practically, however, such designs are limited by losses in the metal layers, further hampered by the fact that a part of the incoming fields falls below the low-k cutoff of the hyperlens and is thus reflected even before reaching the device.

As the practical multilayer design was out of reach, we studied the fundamental limits of the dark-field design, ignoring any additional issues due to realistic material parameters or limitations in available fabrication technologies. From this line of research we ended up with the magnetic hyperlens design and the concept of pseudocanalization. Here, instead of tuning the HMM dispersion to achieve a canalization regime (and thus a straightforward correspondence between the input and output fields) we explored using μ -negative HMMs instead. Introducing negative permeability allows one to flip phase propagation of the plane waves in the HMM, while having the same dispersion relation as a corresponding nonmagnetic HMM. By combining corresponding HMMs we can achieve perfect phase cancellation at the

8. Conclusions

output, which provides the same effect as the ideal canalization. However, as this effect is independent of the HMM parameters (as long as two HMMs are matched to each other) this mechanism allows to achieve dark-field imaging and canalization of output fields at the same time, avoiding the key problem with the nonmagnetic design.

The results with magnetic hyperlens motivated us to look into a more practical platform: hyperbolic surface waves. People have already demonstrated that surface waves on anisotropic structures can behave similarly to waves in HMMs. The key idea of magnetic HMMs is to reverse the phase propagation of the propagating waves. Inspired by work of Shin et al. [60], where reversed phase propagation was proposed for isotropic surface waves (in a metal-dielectric-metal structure), we started looking into hyperbolic waves on two and three layer systems. Indeed, we show that such structures support modes with hyperbolic dispersion and by engineering the three layer structure it is possible to obtain reversed phase propagation. We carried out proof-of-concept simulations, showing that pseudocanalization idea with hyperbolic surface waves is feasible. However, more research in this direction is required, such as optimizing the system to minimize reflections and achieving required effective medium parameters.

Acknowledgments

I have thoroughly enjoyed my time as a PhD student at DTU Fotonik. Working here has always been fun and interesting, through all its ups and downs. First and foremost I would like to thank my supervisors Andrei and Morten for all the advice and help during the way.

A big part of making the time enjoyable has been played by colleagues around me, from Metamaterials group and beyond. The importance of the friendly atmosphere can not be understated, but this has not been the only contribution of the people here. I have been surrounded by talented, motivated and clever people and this has been an important factor in my own personal growth.

Special mention goes to Jan, Aurimas and Hitesh for all the interesting discussions during our lunches and other activities. Furthermore I always enjoyed hearing about your work in cleanroom — as it reminded me that doing numerical simulations is not that bad. Another mention goes to Andreas, for your contributions to the DTU HPC cluster, which have left me many annoying memories waiting my compute jobs to start. Fruitful discussions on numerical simulations and your help with my Danish homework is of course worth a mention.

And of course, support of my family and old friends from Estonia must also be mentioned, especially fellow physicists Ardi and Heino for helpful discussions. A special thanks goes to Heino for proof-reading my the thesis. I am also thankful of members of my secret design council (Taavi, Triinu and Ode) for helping to improve artistic quality of my work.

I would also like to thank members of our Friday morning football team and also runners from Wednesday training runs, for providing an healthy excuse to leave the computer screen.

And finally, I acknowledge support from Archimedes Foundation in financing my PhD studies, along with Otto Mønstedts Fond for funding towards my conference attendances.

Bibliography

- [1] A. Sihvola, “Metamaterials in electromagnetics,” *Metamaterials*, vol. 1, no. 1, pp. 2–11, 2007.
- [2] S. A. Cummer, J. Christensen, and A. Alù, “Controlling sound with acoustic metamaterials,” *Nature Reviews Materials*, vol. 1, no. 3, 2016.
- [3] X. Zheng, H. Lee, T. H. Weisgraber, M. Shusteff, J. DeOtte, E. B. Duoss, J. D. Kuntz, M. M. Biener, Q. Ge, J. A. Jackson, S. O. Kucheyev, N. X. Fang, and C. M. Spadaccini, “Ultralight, ultrastiff mechanical metamaterials,” *Science*, vol. 344, no. 6190, pp. 1373–1377, 2014.
- [4] D. R. Smith, “Metamaterials and negative refractive index,” *Science*, vol. 305, no. 5685, pp. 788–792, 2004.
- [5] S. Maier, *Plasmonics : fundamentals and applications*. New York: Springer, 2007.
- [6] S. A. Maier and H. A. Atwater, “Plasmonics: Localization and guiding of electromagnetic energy in metal/dielectric structures,” *Journal of Applied Physics*, vol. 98, no. 1, p. 011101, 2005.
- [7] J. A. Schuller, E. S. Barnard, W. Cai, Y. C. Jun, J. S. White, and M. L. Brongersma, “Plasmonics for extreme light concentration and manipulation,” *Nature Materials*, vol. 9, no. 3, pp. 193–204, 2010.
- [8] D. K. Gramotnev and S. I. Bozhevolnyi, “Plasmonics beyond the diffraction limit,” *Nature Photonics*, vol. 4, no. 2, pp. 83–91, 2010.
- [9] V. G. Veselago, “The electrodynamics of substances with simultaneously negative values of ϵ and μ ,” *Soviet Physics Uspekhi*, vol. 10, no. 4, p. 509, 1968.
- [10] V. M. Shalaev, “Optical negative-index metamaterials,” *Nature Photonics*, vol. 1, no. 1, pp. 41–48, 2007.

Bibliography

- [11] H. Kosaka, T. Kawashima, A. Tomita, M. Notomi, T. Tamamura, T. Sato, and S. Kawakami, "Superprism phenomena in photonic crystals," *Physical Review B*, vol. 58, no. 16, pp. R10096–R10099, 1998.
- [12] R. A. Shelby, "Experimental verification of a negative index of refraction," *Science*, vol. 292, no. 5514, pp. 77–79, 2001.
- [13] A. Poddubny, I. Iorsh, P. Belov, and Y. Kivshar, "Hyperbolic metamaterials," *Nature Photonics*, vol. 7, no. 12, pp. 948–957, 2013.
- [14] P. Shekhar, J. Atkinson, and Z. Jacob, "Hyperbolic metamaterials: fundamentals and applications," *Nano Convergence*, vol. 1, no. 1, p. 14, 2014.
- [15] D. R. Smith and D. Schurig, "Electromagnetic wave propagation in media with indefinite permittivity and permeability tensors," *Physical Review Letters*, vol. 90, no. 7, p. 077405, 2003.
- [16] Z. Jacob, L. V. Alekseyev, and E. Narimanov, "Optical hyperlens: Far-field imaging beyond the diffraction limit," *Optics Express*, vol. 14, no. 18, p. 8247, 2006.
- [17] A. J. Hoffman, L. Alekseyev, S. S. Howard, K. J. Franz, D. Wasserman, V. A. Podolskiy, E. E. Narimanov, D. L. Sivco, and C. Gmachl, "Negative refraction in semiconductor metamaterials," *Nature Materials*, vol. 6, no. 12, pp. 946–950, 2007.
- [18] Z. Liu, H. Lee, Y. Xiong, C. Sun, and X. Zhang, "Far-field optical hyperlens magnifying sub-diffraction-limited objects," *Science*, vol. 315, no. 5819, pp. 1686–1686, 2007.
- [19] J. Yao, Z. Liu, Y. Liu, Y. Wang, C. Sun, G. Bartal, A. M. Stacy, and X. Zhang, "Optical negative refraction in bulk metamaterials of nanowires," *Science*, vol. 321, no. 5891, pp. 930–930, 2008.
- [20] M. Born, *Principles of optics : electromagnetic theory of propagation, interference and diffraction of light*. Cambridge New York: Cambridge University Press, 1999.
- [21] X. Zhang and Z. Liu, "Superlenses to overcome the diffraction limit," *Nature Materials*, vol. 7, no. 6, pp. 435–441, 2008.
- [22] N. I. Zheludev, "What diffraction limit?," *Nature Materials*, vol. 7, no. 6, pp. 420–422, 2008.

- [23] L. Novotny and B. Hecht, *Principles of Nano-Optics*. Cambridge University Press, 2009.
- [24] R. C. Dunn, “Near-field scanning optical microscopy,” *Chemical Reviews*, vol. 99, no. 10, pp. 2891–2928, 1999.
- [25] S. W. Hell and J. Wichmann, “Breaking the diffraction resolution limit by stimulated emission: stimulated-emission-depletion fluorescence microscopy,” *Optics Letters*, vol. 19, no. 11, p. 780, 1994.
- [26] T. A. Klar and S. W. Hell, “Subdiffraction resolution in far-field fluorescence microscopy,” *Optics Letters*, vol. 24, no. 14, p. 954, 1999.
- [27] J. B. Pendry, “Negative refraction makes a perfect lens,” *Physical Review Letters*, vol. 85, no. 18, pp. 3966–3969, 2000.
- [28] Z. Jacob, L. V. Alekseyev, and E. Narimanov, “Semiclassical theory of the hyperlens,” *Journal of the Optical Society of America A*, vol. 24, no. 10, p. A52, 2007.
- [29] H. Lee, Z. Liu, Y. Xiong, C. Sun, and X. Zhang, “Development of optical hyperlens for imaging below the diffraction limit,” *Optics Express*, vol. 15, no. 24, p. 15886, 2007.
- [30] J. Sun, T. Xu, and N. M. Litchinitser, “Experimental demonstration of demagnifying hyperlens,” *Nano Letters*, vol. 16, no. 12, pp. 7905–7909, 2016.
- [31] J. Sun and N. M. Litchinitser, “Toward practical, subwavelength, visible-light photolithography with hyperlens,” *ACS Nano*, vol. 12, no. 1, pp. 542–548, 2018.
- [32] D. Lu and Z. Liu, “Hyperlenses and metalenses for far-field super-resolution imaging,” *Nature Communications*, vol. 3, no. 1, 2012.
- [33] H. Benisty and F. Goudail, “Dark-field hyperlens exploiting a planar fan of tips,” *Journal of the Optical Society of America B*, vol. 29, no. 9, p. 2595, 2012.
- [34] T. Repän, A. V. Lavrinenko, and S. V. Zhukovsky, “Dark-field hyperlens: Super-resolution imaging of weakly scattering objects,” *Optics Express*, vol. 23, no. 19, p. 25350, 2015.
- [35] L. Shen, H. Wang, R. Li, Z. Xu, and H. Chen, “Hyperbolic-polaritons-enabled dark-field lens for sensitive detection,” *Scientific Reports*, vol. 7, no. 1, 2017.

Bibliography

- [36] A. Novitsky, T. Repän, S. V. Zhukovsky, and A. V. Lavrinenko, "Subwavelength hyperlens resolution with perfect contrast function," *Annalen der Physik*, vol. 530, no. 3, p. 1700300, 2018.
- [37] X. Ao and C. T. Chan, "Far-field image magnification for acoustic waves using anisotropic acoustic metamaterials," *Physical Review E*, vol. 77, no. 2, 2008.
- [38] T.-Y. Chiang, L.-Y. Wu, C.-N. Tsai, and L.-W. Chen, "A multilayered acoustic hyperlens with acoustic metamaterials," *Applied Physics A*, vol. 103, no. 2, pp. 355–359, 2011.
- [39] J. Li, L. Fok, X. Yin, G. Bartal, and X. Zhang, "Experimental demonstration of an acoustic magnifying hyperlens," *Nature Materials*, vol. 8, no. 12, pp. 931–934, 2009.
- [40] J. Zhu, J. Christensen, J. Jung, L. Martin-Moreno, X. Yin, L. Fok, X. Zhang, and F. J. Garcia-Vidal, "A holey-structured metamaterial for acoustic deep-subwavelength imaging," *Nature Physics*, vol. 7, no. 1, pp. 52–55, 2010.
- [41] M. Molerón and C. Daraio, "Acoustic metamaterial for subwavelength edge detection," *Nature Communications*, vol. 6, no. 1, 2015.
- [42] T. Repän, A. Novitsky, M. Willatzen, and A. V. Lavrinenko, "Pseudocanalization regime for magnetic dark-field hyperlenses," *Physical Review B*, vol. 96, no. 19, 2017.
- [43] D. Griffiths, *Introduction to electrodynamics*. Cambridge, United Kingdom New York, NY: Cambridge University Press, 2017.
- [44] A. Eroglu, *Wave Propagation and Radiation in Gyrotropic and Anisotropic Media*. Springer US, 2010.
- [45] Y. Guo, W. Newman, C. L. Cortes, and Z. Jacob, "Applications of hyperbolic metamaterial substrates," *Advances in OptoElectronics*, vol. 2012, pp. 1–9, 2012.
- [46] A. Fang, T. Koschny, and C. M. Soukoulis, "Optical anisotropic metamaterials: Negative refraction and focusing," *Physical Review B*, vol. 79, no. 24, 2009.
- [47] J. Polo, *Electromagnetic surface waves : a modern perspective*. Amsterdam Boston: Elsevier, 2013.

- [48] O. Kidwai, S. V. Zhukovsky, and J. E. Sipe, “Effective-medium approach to planar multilayer hyperbolic metamaterials: Strengths and limitations,” *Physical Review A*, vol. 85, no. 5, 2012.
- [49] S. V. Zhukovsky, A. Andryieuski, O. Takayama, E. Shkondin, R. Malureanu, F. Jensen, and A. V. Lavrinenko, “Experimental demonstration of effective medium approximation breakdown in deeply subwavelength all-dielectric multilayers,” *Physical Review Letters*, vol. 115, no. 17, 2015.
- [50] L. M. Brekhovskikh, *Acoustics of layered media I : plane and quasi-plane waves*. Berlin New York: Springer, 1998.
- [51] A. Pierce, “Basic linear acoustics,” in *Springer Handbook of Acoustics*, pp. 25–111, Springer New York, 2007.
- [52] D. Torrent and J. Sánchez-Dehesa, “Anisotropic mass density by two-dimensional acoustic metamaterials,” *New Journal of Physics*, vol. 10, no. 2, p. 023004, 2008.
- [53] J. Mei, Z. Liu, W. Wen, and P. Sheng, “Effective dynamic mass density of composites,” *Physical Review B*, vol. 76, no. 13, 2007.
- [54] P. A. Belov, Y. Hao, and S. Sudhakaran, “Subwavelength microwave imaging using an array of parallel conducting wires as a lens,” *Physical Review B*, vol. 73, no. 3, 2006.
- [55] A. Salandrino and N. Engheta, “Far-field subdiffraction optical microscopy using metamaterial crystals: Theory and simulations,” *Physical Review B*, vol. 74, no. 7, 2006.
- [56] T. Repän, S. Zhukovsky, A. Lavrinenko, and M. Willatzen, “Dark-field hyperlens for high-contrast sub-wavelength imaging,” in *Metamaterials X* (A. D. Boardman, N. P. Johnson, K. F. MacDonald, and E. Özbay, eds.), SPIE, 2016.
- [57] A. D. Rakić, A. B. Djurišić, J. M. Elazar, and M. L. Majewski, “Optical properties of metallic films for vertical-cavity optoelectronic devices,” *Applied Optics*, vol. 37, no. 22, p. 5271, 1998.
- [58] O. Takayama, A. A. Bogdanov, and A. V. Lavrinenko, “Photonic surface waves on metamaterial interfaces,” *Journal of Physics: Condensed Matter*, vol. 29, no. 46, p. 463001, 2017.

Bibliography

- [59] M. Dyakonov *Sov. Phys. JETP*, vol. 67, p. 714, 1988.
- [60] H. Shin and S. Fan, “All-angle negative refraction for surface plasmon waves using a metal-dielectric-metal structure,” *Physical Review Letters*, vol. 96, no. 7, 2006.
- [61] D. Sarid, *Modern introduction to surface plasmons: theory, Mathematica modeling, and applications*. Cambridge New York: Cambridge University Press, 2010.
- [62] C.-L. Chen, *Foundations for guided-wave optics*. Hoboken, N.J: Wiley-Interscience, 2007.